ANALYSIS OF MITRAL REGURGITATION USING ECHOCARDIOGRAPHIC IMAGES

Ph. D. Thesis

by

ARUN BALODI

DEPARTMENT OF ELECTRICAL ENGINEERING
INDIAN INSTITUTE OF TECHNOLOGY ROORKEE
ROORKEE – 247667 (INDIA)
SEPTEMBER, 2017

ANALYSIS OF MITRAL REGURGITATION USING ECHOCARDIOGRAPHIC IMAGES

A THESIS

Submitted in partial fulfilment of the
requirements for the award of the degree

of

DOCTOR OF PHILOSOPHY

in

ELECTRICAL ENGINEERING

by

ARUN BALODI

DEPARTMENT OF ELECTRICAL ENGINEERING
INDIAN INSTITUTE OF TECHNOLOGY ROORKEE
ROORKEE – 247667 (INDIA)
SEPTEMBER, 2017

INDIAN INSTITUTE OF TECHNOLOGY ROORKEE ROORKEE

CANDIDATE'S DECLARATION

I hereby certify that the work which is being presented in the thesis entitled "**ANALYSIS OF MITRAL REGURGITATION USING ECHOCARDIOGRAPHIC IMAGES"** in partial fulfilment of the requirements for the award of the Degree of Doctor of Philosophy and submitted in the Department of Electrical Engineering of the Indian Institute of Technology Roorkee, Roorkee, is an authentic record of my own work carried out during a period from January, 2013 to September, 2017 under the supervision of Dr. M. L. Dewal, Professor and Dr. R. S. Anand, Professor, Department of Electrical Engineering, Indian Institute of Technology Roorkee, Roorkee.

The matter presented in this thesis has not been submitted by me for the award of any other degree of this or any other Institution.

(ARUN BALODI)

This is to certify that the above statement made by the candidate is correct to the best of our knowledge.

(M. L. Dewal)
Supervisor

(R. S. Anand)
Supervisor

Date:

ABSTRACT

The valvular heart disease (VHD) is one of the major cause of morbidity and mortality throughout the world. It affects any of the four valves of the heart (the aortic and mitral valves on the left and the pulmonary and tricuspid valves on the right). The valvular abnormality can be of two types (i) regurgitation and (ii) stenosis. A thorough understanding of the valvular abnormalities are very important to aid in the management of patients with valvular abnormality. Valvular regurgitation is defined as the backward or retrograde flow of blood from the valves into the cardiac chambers when the leaflets do not close completely. This backward flow is referred as "regurgitant flow". In valvular stenosis, the valvular leaflet becomes stiffer which narrows the valve opening and reduces the blood flow through it. Each of the four valves of the heart may exhibit these abnormalities. The presented research work carried out with an aim to enhance the diagnostic potential of conventional B-mode ultrasound imaging modality for the diagnosis and severity analysis of mitral regurgitation (MR). The MR is the most common valvular disorder in modern clinical practice. It is known as the reverse blood flow from the left ventricle (LV) into the left atrium (LA) during the systole process. The ultrasound of the heart is known as echocardiography and is most commonly used in the assessment of cardiac chamber and valvular abnormalities. The aetiologies and the consequences of valvular abnormalities are diagnosed using transthoracic echocardiographic (TTE) images acquired in apical two chamber (A2C), apical four chamber (A4C) and parasternal long axis (PLAX) views. The ultrasound imaging modalities such as conventional B-Mode (brightness mode), M-Mode (motion mode), continuous wave Doppler (CWD), and color Doppler echocardiography are used hand-in-hand to detect the prevalence of regurgitation, a better understanding of the mechanism of regurgitation and quantification of severity along with its repercussions.

A fine-grained textural pattern known as speckle noise is observed in B-mode TTE images which reduce the contrast resolution and masks the texture details. It often makes quantitative measurements and the automatic analysis of ultrasound images difficult. The contemporary research demonstrate the importance and superiority of despeckling techniques. Individual techniques have their merits and demerits. The performance of the despeckling filter is

measured utilizing different performance parameters and visual quality parameters. The automatic estimation of cardiac structures and shape and size become very difficult because of the speckle noise. The speckle noise also affects location of edge features, therefore it is very important to preserve the edges in medical images while doing despeckling. In order to address this issue, as a first objective of this work, a comparative study of despeckling filters of five categories (i) local adaptive, (ii) synthetic aperture radar (SAR), (iii) anisotropic diffusion, (iv) non-local mean, and (v) fuzzy filters have been implemented on test images and TTE images. The despeckling capabilities of these filters have been evaluated in terms of traditional image quality metrics as well as blind image quality metrics. A hybrid homomorphic fuzzy (HHF) filter, combining the advantages of NLM and fuzzy filters, has been proposed here. The denoising performance parameters of the HHF filter are compared with despeckling techniques in the homomorphic and non-homomorphic domain. The HFF filter performed better in terms of edge preservation compared to other fuzzy filters.

The commonly used methods for the quantification of MR still has many limitations, such as the uncertainties in orifice location, multiple jets, and a hemispheric convergence assumption that often results in over or underestimation of flow rate and regurgitation orifice area. These techniques are operator-dependent and often significant training is required to acquire good quality and correct data. It is difficult to analyze manually the acquired data due to the poor quality of echocardiographic images during the diagnosis at various stages. It is quite challenging to derive the necessary information from the acquired data by the technicians. Also, the manual analysis is a subjective methodology; it compromises on the accuracy of diagnosis and severity estimation. It is very difficult to reproduce quantitative measurements, manually. To overcome the issues associated with the severity analysis of MR, machine vision technology has been employed.

Keeping the above facts in view, the second objective of this work has been planned as to develop the texture feature extraction techniques to acquire substantial information from echocardiographic images and to improve the classification accuracy of the computer-aided diagnosis (CAD) system for the severity analysis of MR. In this approach, two steps have been involved. The first step has been to extract the features of the echocardiographic images and in the second step the relevant features among the above extracted features on the basis of certain criteria have been considered as input to the various classifier techniques. An optimized classifier has been selected on the basis of experimentation.

Here, the texture analysis of the MR images has been accomplished through proposed three approaches.

In first approach, eight texture features, (i) first order statistics (FOS), (ii) spatial gray level dependence matrices (SGLDM), (iii) gray level difference statistics (GLDS), (iv) neighborhood gray tone difference matrix (NGTDM), (v)statistical feature matrix (SFM), (vi) Laws textures energy measure (Laws TEM), (vii) fractal dimension texture analysis (FDTA), and (viii) Fourier power spectrum (FPS) have been extracted from the MR image database in three views with four color spaces. The minimum Redundancy Maximum Relevance (mRMR) feature selection techniques have been chosen to eliminate the less relevant features. Finally, two supervised classifiers support vector machine (SVM) with three kernel (linear, polynomial, radial basis function (RBF)) and random forest (RF) has been used along with 10-fold and leave-one-out cross validation technique to reduce biasness. The classification accuracy of the proposed CAD system in red green blue (RGB) color space has been found slightly better than gray-scale color space, however the computational time of the scheme was thrice compared to gray-scale model. Subsequently, the performance of the CAD system has been evaluated in terms of the classification accuracy, severity, and specificity.

In the second approach, the multiresolution based texture feature extraction techniques have been utilized in proposed CAD system. The images are decomposed at several levels of different resolution, where each of the sub-images contain varied and valuable information about the original image. In order to enrich the quality of the texture feature extraction technique the Gaussian pyramid has been used because of less computational requirement. Moreover, to extract the texture features from the decomposed images, variants of the local binary pattern (LBP) such as uniform local binary pattern (LBP^{u2}), rotation invariant local binary pattern (LBP^{ri}), rotation invariant uniform local binary pattern (LBP^{riu2}), center-symmetric local binary pattern (CSLBP), local binary pattern histogram Fourier features (LBP-HF), and completed local binary pattern (CLBP) have been applied. Furthermore, the performance of the extracted features has been evaluated using SVM and random forest (RF) classifier with 10-fold cross validation. The Gaussian pyramid based completed local binary pattern (GP-

CLBP) technique was found to be produced the best classification accuracy amongst the all proposed features.

In the third approach, the discriminatory capability of Daubechies wavelet-based texture modeling has been assessed for the severity analysis of MR. The transform domain techniques have been opted due to their multiresolution capability for analyzing images at different frequencies of several levels of resolutions. The different frequency sub-band images provide substantial information about the various objects of the images compared to the information obtained in spatial domain grayscale images. In the present work, discrete wavelet transform (DWT) technique has been utilized to get transformed domain features as it has the property to emphasize the directional information of the images. The Daubechies wavelet family has been utilized for the image decomposition because of its approximate shift invariance property. This multiresolution based texture feature extraction techniques produces a large number of complex features and many of the features may not be significant. Keeping this aspect in mind, PCA has been used as feature reduction technique in order to reduce the dimension of feature vector. Additionally, the mRMR has been chosen as feature selection techniques to eliminate the less relevant features. At the end, both the utilized techniques, improve the classification performance of the CAD system and reduce the computational time. The db4 offered best characteristics among the Daubechies wavelet family considered for precise severity investigation of the MR images.

The significant contribution of this thesis work can be summed up as the development of a CAD system for severity analysis of mitral regurgitation using echocardiographic images. The CAD system developed for the severity analysis of MR is capable to classify the different categories of the MR stages with reasonable accuracy. The achieved classification accuracy of the proposed CAD systems helped to enhance the productivity of clinicians while supporting them with some useful information.

ACKNOWLEDGEMENTS

It is my desire and a great pleasure to offer my sincere thanks to all those who have contributed, in whatever way, to the completion of my work.

First, I take this opportunity to express my sincere gratitude to toward my supervisors Dr. M. L. Dewal, Professor and Dr. R. S. Anand, Professor, Department of Electrical Engineering, Indian Institute of Technology Roorkee, Roorkee, India for their constant encouragement and motivation throughout the duration of this research work. I also express my sincere gratitude to Dr. Anurag Rawat, Associate Professor, Department of Cardiology, Swami Rama Himalayan University, Dehradun, India who helped me during the collection of data for the study and gave the background knowledge of the dataset. I have been very fortunate to receive their continuous academic advice, endless patience, and priceless guidance and support throughout this work.

I am also thankful to my research committee members, Prof. Vinod Kumar, Prof. P. K. Garg, Dr. P. Sumathi, Dr. M. L. Sharma, and Dr. Barjeev Tyagi, for their constructive suggestions during several meetings held for this research work. I would also like to thank the Head of the Department and other faculty members of Electrical Engineering Department, IITR for their moral support and providing the excellent laboratory facilities during this research work at Indian Institute of Technology Roorkee, Roorkee. I would thank the Ministry of Human Resources Development (MHRD), Government of India for providing the fellowship for carrying out this research work. I wish also to mention the memorable conversation I have with Prof. M. K. Vasantha and Dr. Vinay Pant. I also thank the technical and office staff of the department, especially Mr. Mohan Singh, Mr. Rishabh Verma, Mr. Jogeshwar Prasad, Mr. Amir Ahmad and Mr. Veer Chand for their cooperation and help in official work related to this research. Also, superintendent in Instrumentation and Signal Processing Laboratory, Mr. Jogeshwar Prasad deserve my highest appreciation.

I also sincerely acknowledge the financial support and assistantship provided by the Ministry of Human Resource Development, Government of India. I also thank the Department of Electrical Engineering, Indian Institute of Technology Roorkee, Roorkee, India, for providing me the opportunity to pursue the Ph.D. program. I extend my sincere acknowledge to the Department of Cardiology, Swami Rama Himalayan University, Dehradun, India, and the clinicians of Echo Lab, Mr. Dev Singh and Mrs. Babita Ji who support me to procure the data set and gave the medical ethical clearance for this study.

I would like to thank the anonymous reviewers of my research work, who gave me the suggestions to improve the quality of the research work and the direction for the additional work.

My journey in IIT Roorkee is blessed with many friends who played a major role in maintaining a constantly high level of motivation, and thus in the progress of my work. I would give special acknowledgment to my fellow researchers, Dr. N. Biradar, Dr. A. R. Yadav, Mr. Jayendra Kumar Dr. Deep Gupta, Dr. Sachin Singh, Dr. Roshan Kumar, Dr. KSH Milan, Dr. Om Hari Gupta, Dr. Bhavik Patel, Dr. Jitendra Singh, Dr. Gaurav Kabra, Dr. Mohit Yadav, Mrs. Soumi Ray, Mr. Yogesh Sariya, Mr. Haresh Shabhadia, Mr. Akhilesh Mathur, Mr. Krishna Murari Pandey, Mr. Tushar Tyagi, Dr. Shiv Raman Thapliyal, Mr. Naveen Chandra, Mr. Anuj Upadhyay, Mr. Yogesh Makwana and many more.

I wish to express my hearty gratitude to my parents and all my family members, for their endless moral support and encouragement. Finally, I am very thankful to all-merciful God who gave me blessing and wisdom to carry out this Ph.D. research work.

(Arun Balodi)

TABLE OF CONTENTS

LIST OF FIGURES

LIST OF TABLES

LIST OF ACRONYMS

2D	Two Dimensional
3D	Three Dimensional
AD	Anisotropic Diffusion
ANN	Artificial Neural Networks
ATMED	Asymmetrical Triangular Function with a Median Filter
AV	Aortic Valve
BP-NN	Backpropagation Neural Network
CAD	Computer-aided Diagnosis
CCA	Curvilinear Component Analysis
CLBP	Completed Local Binary Pattern
CMY	Cyan Magenta Yellow
CNN	Convolutional Neural Network
CSLBP	Center-symmetric Local Binary Pattern
CT	Computed Tomography
CW	Continuous Wave
DCT	Discrete Cosine transform
DHS	Doppler Heart Sounds
DPAD	Detail Preserving Anisotropic Diffusion
DWT	Discrete Wavelet Transform
ENL	Effective Number of Looks
EROA	Effective Regurgitant Orifice Area
EVLBP	Extensive Volume Local Binary Pattern
FDTA	Fractal Dimension Texture Analysis
FF-NN	Feed Forward Neural Network
FMRI	Functional Magnetic Resonance Imaging
FNLM	Fast Nonlocal Mean
FoM	Figure of Merit
FOS	First Order Statistics

FPS	Fourier Power Spectrum
GLDS	Gray Level Difference Statistics
GLGCM	Gray Level-gradient Co-occurrence Matrix
GLRLM	Gray Level Run Length Matrix
GP	Gaussian Pyramid
GT	Gabor Transform
GTSVM	Growing Time Support Vector Machine
HFF	Hybrid Fuzzy Filter
HMM	Hybrid Hidden Markov Model
IDL	Image Decomposition Level
IDPC	Image Detail Preserving Coefficient
IMC	Information Measure of Correlation
IQM	Image Quality Metrics
k-NN	k-Nearest Neighbors
LBP	Local Binary Pattern
LBP-HF	Local Binary Pattern Histogram Fourier Features
LBPri	Rotation Invariant Local Binary Pattern
LBPriu2	Rotation Invariant Uniform Local Binary Pattern
LBPu2	Uniform Local Binary Pattern
LDA	Linear Discriminant Analysis
LMSC	Local Statistics Mean Variance
LMSE	Laplacian Mean Square Error
LOO-CV	Leave-one-out Cross Validation
LP	Laplacian Pyramid
LS-SVM	Least Squares Support Vector Machines
LTEM	Laws Textures Energy Measure
LV	Left Ventricle
LVEIO	Left Ventricular Early Inflow-Outflow Index
LVSD	Left Ventricular Systolic Dysfunction
MI	Myocardial Infarction

MR	Mitral Regurgitation
MRI	Magnetic Resonance Imaging
mRMR	Minimal Redundancy Maximum Relevance
MS	Mitral Stenosis
MSE	Mean Square Error
MV	Mitral Valve
NCC	Normalized Correlation Coefficient
NCD	Nonlinear Coherent Diffusion
NGTDM	Neighborhood Gray Tone Difference Matrix
NLM	Nonlocal Mean
NMSE	Normalized Mean Square Error
NN	Neural Network
OCT	Optical Coherence Tomography
OSRAD	Oriented Speckle Reducing Anisotropic Diffusion
PCA	Principal Component Analysis
PET	Positron Emission Tomography
PISA	Proximal Isovelocity Surface Area
PLAX	Parasternal Long Axis
PM	Papillary Muscle
PNN	Probabilistic Neural Network
PR	Pulmonary regurgitation
PSNR	Peak Signal to Noise Ratio
PV	Pulmonary Valve
PW	Pulse Doppler
R Vol	Regurgitant Volume
RBF	Radial Basis Function
RF	Random Forest
RGB	Red Green Blue
RMSE	Root Mean Square Error
RV	Right Ventricle

SAR	Synthetic Aperture Radar
SFM	Statistical Feature Matrix
SGLCM	Spatial Gray-level Co-occurrence Matrices
SI	Speckle Index
SMPI	Speckle Suppression and Mean Preservation Index
SNR	Signal to Noise Ratio
SPECT	Single Photon Emission Computed Tomography
SRAD	Speckle Reducing Anisotropic Diffusion
SSI	Speckle Suppression Index
SSIM	Structural Similarity Index Metrics
STFT	Short-time Fourier Transform
SVM	Support Vector Machine
TEE	Transesophageal Echocardiography
TMAV	Triangular Moving Average Center Filter
TMED	Triangular function with median center filter
TMVR	Transcatheter Mitral Valve Repair
TTE	Transthoracic Echocardiography
TV	Tricuspid Valve
US	Ultrasound
VC	Vena Contracta
VHD	Valvular Heart Disease
VSD	Ventricular Septal Defects
WP	Wavelet Packets

CHAPTER 1

INTRODUCTION

This chapter presents an introduction to the proposed research work carried out. Firstly, the components of a computer aided classification system are briefly discussed to provide a background of medical image analysis. Secondly, the importance of the feature extraction in classification. At last, literature regarding each task is discussed separately. The objectives of current research work have also been outlined.

1.1 Motivation

The heart is the vital organ of the human body that pumps blood throughout the body and supply nutrients to the tissues along with oxygen and removing carbon dioxide and other wastes from the body. Nowadays, the number of cardiovascular diseases such as valvular heart disease is on the rise throughout the world [1]. Valvular heart disease is the disease that affects the four valves of the heart (the aortic and mitral valves on the left and the pulmonary and tricuspid valves on the right). The improper diagnosis of the diseases due to the absence of symptoms until the disease has reached its advanced stage has also made the situation worse. However, if the disease is diagnosed in the early phase, the patients can survive longer. Nevertheless, the symptoms may change from patient to patient. Medical imaging modalities permit a physician to make analyses and treatment more exact. Furthermore, it helps in acquiring logical information of different diseases. Therefore their effect on other anatomical structures to oversee appropriate treatment, intra-agent route, and surgical planning can be observed [2–4].

Conventionally, several imaging modalities such as X-ray, computed tomography (CT), ultrasound (US), magnetic resonance imaging (MRI), positron emission tomography (PET), single photon emission computed tomography (SPECT) and functional magnetic resonance imaging (fMRI) have been utilized for taking the medical images of internal body parts of patients for the diagnosis of different diseases. These are accessible for procuring the remarkable views of different organs in various perspectives [2,5,6]. Among the above medical imaging modalities, the images obtained from the ultrasound B-scans are broadly utilized in diagnosis because of its cost viability, transportability, acceptability, and safety it offers. The ultrasound of the heart is known as echocardiography.

Many images are obtained for better reconstruction but it lengthens the time of acquisition and introduces motion artifacts [7, 8]. It is operator-dependent and often significant training is required to acquire good quality and correct data. Further, it is difficult to analyze manually the acquired data due to the poor quality of images and drawbacks of the imaging modalities, during the diagnosis at various stages. It is also challenging to extract or infer the necessary information from the acquired data by the technicians. Also, the manual analysis is a subjective methodology; it compromises on the accuracy of diagnosis and severity estimation [9–16]. It is very difficult to reproduce quantitative measurements. This triggers the need for a reliable computer-aided diagnosis (CAD) system based on software-based techniques for automatic analysis of the medical images. The current thesis in above perspective aims to enhance the diagnostic potential of conventional B-mode ultrasound imaging modality for the diagnosis and severity analysis of mitral regurgitation (MR).

1.2 Overview of Computer-aided Diagnosis (CAD) System

The aim of a CAD system is to reduce the interobserver and intraobserver error by classifying sensed object into predefined classes. In our case, the sensed objects are the echocardiographic image dataset in three views which need to be classified into three classes of mitral regurgitation as mild, moderate, and severe. The components of typical classification system are depicted in the following block diagram of Fig. 1.1.

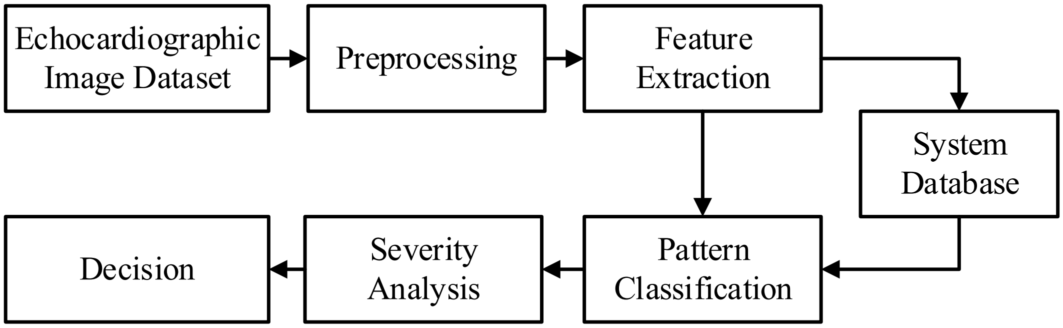

Fig. 1.1: Block diagram of classification system

The function of each blocks shown in Fig. 1.1 are described as follow:

- *Echocardiographic Image Dataset:* The processing starts with procuring the echocardiographic image dataset which contains the images of patients suffering from MR in three views in three classes (mild, moderate, and severe).

- *Preprocessing:* Here the data is recorded in video mode, hence it has to convert into frames. For better classification results, the images are preprocessed to reduce the effects of illumination. The selection of color space may also affect the performance of classification system.

- *Feature Extraction:* It acquires relevant data representation to extract discriminative information. Templates created from extracted features are stored in the system database during the training phase for the purpose of matching when the test sample is presented during classification phase.

- *Pattern Classification:* Classification involves comparison of features extracted from the test sample with templates stored in the system database. Based on scores obtained from the comparison, the output of the pattern classification block indicates the estimated class of the input test image.

- *Severity Analysis:* In the last step, after getting the decision from the individual view, the multi-voting is used to get the final decision.

1.3 Characteristics of Textural Information in Biomedical Images

The texture analysis is broadly investigated in numerous area of image processing such as computer vision, pattern recognition, and medical image analysis. The design of CAD system based on texture analysis for medical images has pulled in consistently developing consideration over the most recent couple of years. Among various processing stages shown in Fig. 1.1, feature extraction stage is the most critical stage. In order to perform classification, it is essential to represent the available data appropriately. If the features are not discriminative enough, even the best classifier cannot provide decent classification performance. The feature extraction algorithms should be able to have the capacity to catch between class varieties and in the meantime, limit the impact of between class variety. Moreover, the approaches to texture analysis are categorized as [17]:

- *Statistical methods:* The statistical approaches represent the texture by the non- deterministic properties. In these methods the texture can be mathematically represented by a set of first or second order statistics. The first order statistics relate to the probability of individual pixels having particular intensity values. The second-order statistics identify with the joint probability of two arbitrary pixels in the picture having particular sets of intensity values.

- *Model-based methods:* This approach utilized fractal and stochastic models for the texture analysis. These approaches attempt to interpret an image by use of, respectively, generative image model and stochastic model. The extracted parameters of the models are used for image analysis. The fractal parameters can be viewed as a measure of irregularity or heterogeneity of spatial arrangements. The main issue with the stochastic model parameters is the computational complexity in the estimation of model parameters.

- *Transform-based methods:* These methods such as Fourier (DFT, DCT), Gabor, and wavelet, transform the image into a different space, with the aim of highlighting texture properties (such as frequency or size) and maximize the geometrical separability of different types of textures. The Fourier based approach is generally renowned for suffering from lack of spatial localization. Gabor filter gives better spatial localization while wavelet transforms features have several advantages as there is a wide range of wavelet functions.

1.4 Literature Review

Medical images give the information about the internal anatomy of human body. Generally, these images are analyzed by the radiologist for clinical analysis and medical intervention. However, manual examination of these images is a time-consuming process that also has the high probability of human error. To this end, the importance of computer-aided diagnosis (CAD) system has been widely acknowledged by the practitioners and researchers [18–25]. The ultrasound-based echocardiography turns into the first line image modality in the analysis and appraisal of valvular disease [19,23,25].

A limited study has been reported in literature delivering technical information on texture analysis of echocardiographic images with respect to valvular insufficiency such as regurgitation and stenosis. The overall research has been done in the area of quantitative analysis of valvular insufficiency, boundary detection of heart chambers, and very less information related to segmentation of mosaic patterned regurgitant jet against the colored background. The majority of the studies on echocardiography focuses on clinical aspects of the regurgitant jet and the vena contracta width assessment.

This section presents a review of published literature on quantification of valvular regurgitation specifically mitral regurgitation, the despeckling techniques for echocardiographic images, and the available texture analysis methods for various diseases such as carotid plaque, breast cancer, liver lesions, etc.

1.4.1 Overview on Quantification of Mitral Regurgitation

The accurate assessment of the degree of valvular regurgitation is a challenging issue for the practitioners such as cardiologists. A fast and accurate method is desirable for the evaluation of mitral regurgitation (MR). In spite of the fact that few methods have been hypothesized to evaluate MR, each method has its own advantages and shortcomings.

The vena contracta (VC) is portrayed as the narrowest central flow area of the regurgitant jet that occurs at, or just downstream to, the orifice of the regurgitant valve [26, 27]. It is somewhat smaller than the mitral orifice because of boundary impacts, hence, the effective regurgitant orifice area (EROA) can be measured by the VC [28]. Numerous studies demonstrated that the VC width measured by utilizing color Doppler echocardiography is broadly utilized for the evaluation valvular regurgitation [29–39]. In case of MR, the VC diameter can vary over time [40]. The diameter of VC should be measured at the season of its maximal width for MR. A modified parasternal long-axis view is best to image the VC with the transducer along the side deciphered, if necessary, to allow complete visualization of the MR jet [41].

The proximal isovelocity surface area (PISA) [42] method become a most popular method for the estimation of the volume flow rate in valvular regurgitation [43,44]. Min Pu et al. [45] exhibited a competent method to evaluate MR known as proximal flow convergence, which may overestimate the flow when the flow field is stressed. Mutlu et al. [46] compared the color Doppler methods for analysis of MR utilized TTE and TEE images. Here, two parameters have been calculated named effective orifice area (EOA) and MR volume. Bhachu et al. [47] utilized a control volume strategy to investigate the hypothetically exact and safe MRI procedure to measure mitral regurgitation. In spite of the fact that reviews from in-vitro flow have indicated incredible outcomes as far as accuracy, the testing of this procedure in-vivo has not yet been portrayed by any reviews. Baspinar et al. [48] reported that the PISA method is sufficient to predict rheumatic MR accurately. Little et al. [49] analyzed the exactness of continuous 3-D color Doppler VC region and also 2-D VC diameter in their vitro model to assess MR seriousness.

Marsan et al. [50] proposed the possibility and exactness of real-time 3-dimensional (3D) echocardiography for the estimation of MR, with velocity-encoded cardiac magnetic resonance (VE-CMR). Biner et al. [51] performed a quantitative assessment of MR based on color flow Doppler jet area to assess the inter-observer agreement of PISA and VC for differentiating severe from nonsevere MR. They have felt that color Doppler-based quantitative estimations for evaluating MR as intense or non-intense relying upon inter-observer analogy. Quader et al. [52] concluded that 3D echocardiography can overcome some of the limitations of 2D multiplane transesophageal echocardiography (TEE). It is decisive in the evaluation of patients who are going through mitral valve surgery. As 3D echo is complementary to 2D, multiple TEE should be utilized as part of the mitral valve preoperative assessment. Lee et al. [53] introduced a simple-to-use echocardiographic parameter, left ventricular early inflow-outflow index (LVEIO). This study demonstrates that the LVEIO correlates with severe MR independently, whereas MR jet area, vena contracta width, and effective regurgitant orifice area measured by the PISA method correlate with MR in combination.

At present, available echocardiographic techniques for quantifying valvular regurgitation are confined by various factors, including uncertainties in orifice location and a hemispheric convergence assumption that often results in over/under estimation of flow rate and regurgitation orifice area [54–56]. However, Grayburn and Bhella [57] reported 60 % variation in all the parameters computed by various clinicians. Various studies have been reported on the MR based cases of mitral valve repair or replacement. Further, Ge et al. [58] suggested that transcatheter mitral valve repair (TMVR) is safe and effective for the patients with severe MR. Kaneko et al. [59] conducted an observational panel study to clarify the prevalence and prognosis of functional MR (FMR) and left ventricular systolic dysfunction (LVSD). Kron et al. [60] analyze the prediction of recurrent MR after mitral valve repair. This model used logistic regression to estimate the probability of recurrence or death.

Many researchers have discussed the measurements related to left atrium and left ventricle [61–65]. In [66], double thresholding strategy is utilized for left ventricle endocardium recognition. A snake-based algorithm is used for endocardial boundary detection in [67]. Active contour model was first proposed in [68]. There are many research papers which depend on deformable models or active contour model [63, 69–72]. An energy minimizing deformable spline influenced by constraint and image forces that pull it toward object contours is called active contour. Snakes are largely used in applications like boundary detection, object tracking, shape recognition, segmentation, edge detection, stereo matching.

1.4.2 Overview on Despeckling of Echocardiographic Images

The ultrasound-based echocardiographic images experienced the interference of the impedance invited because of the fluctuating backscattered echoes of the arbitrarily appropriated dissipates, acknowledged as speckle. Speckle noise is multiplicative in nature which makes the visual analysis of ultrasound images very difficult [73,74]. It occurs in all imaging modalities utilizing coherent waves for illumination such as synthetic aperture radar, and optical coherent tomography. The speckle noise is omnipresent in all cross-sectional views in echocardiography [75] and it is more effective compared to the additive noise [76]. The principal delineation of speckle in the literature is based on the characterization of laser speckle by Goodman [77]. The granular rebound is not a consequence of any blood structure yet rather develops as a result of instability diffusing from the self-assertively appropriated platelets [78]. The dot design does not depend on upon the properties of the disseminating medium [79].

The synthetic aperture radar (SAR) images also suffered from speckle [80]. The most prominently utilized despeckling filters in SAR community in the statistical category include Lee [81,82], Frost [83,84], and Kuan [85,86]. The strategy for homomorphic filtering [87,88] resembles the logarithmic point operations utilized as a part of histogram improvement, in which dominant bright pixels are de-emphasized. The median filter is a nonlinear filter and a specific case of an order statistic filter, which applies to all the pixels whether they are corrupted or not. The weighted median filter has an advantage compared to median filter that it preserves the edges [89]. The other arrangement of filters depended on the neighborhood statistical parameters, for example, the mean, maximum, minimum, and the average values. The Wiener filter, proximity-based filter [90] and statistic filters were likewise tried for noise reduction in the images. These filters can preserve the edges but do not enhance them as required in most of the medical ultrasound based applications. They have also been analyzed for speckle noise reduction in the ultrasound images of kidney, liver, carotid artery and heart [7, 91–95].

Perona and Malik [96] proposed an approach based on the nonlinear anisotropic diffusion (AD) methods, where the anisotropic diffusion equations provide the approach for selective image smoothing. In diffusion filtering, noise at the edges cannot be successfully eliminated. To overcome this problem, the concept of coherence-enhancing diffusion based on diffusion tensors models was proposed in [97]. The nonlinear coherent diffusion (NCD) method of [98] was a tensor-valued AD scheme for the removal of speckle noise. The noise suppression and edge enhancement based on the instantaneous coefficient of variation was advocated by Yu and Acton [7]. This technique was based on modifications of AD filter and was known as speckle reducing anisotropic diffusion (SRAD) filter. This method makes fine details to be more visible in the image but has a limitation in preserving subtle features because of blurring of the edges. Giloba et al. [99] proposed nonlinear complex diffusion filter (NCDF) used for image enhancement. Various modifications were suggested by various authors to improve the performance of the SRAD filter [100]. A detail preserving anisotropic diffusion (DPAD) technique was proposed in [101] to evaluate the comparability between the threshold controlling the level of diffusion and variation in noise coefficient by consolidating different alterations to the SRAD filter. An oriented speckle reducing anisotropic diffusion (OSRAD) was proposed in [102] for enhancing the capability of varying diffusion with direction to speckle adaptive diffusion filtering. Liu and Liu [103] proposed a different approach for the construction of diffusion tensor using a four directional derivative based AD for noise reduction in the standard test image of Lena and a synthetic test image. A modified nonlinear complex diffusion filter was proposed by Saini et al. [104] proposed a despeckle filter by modifying the diffusion coefficient and time step size for ultrasound images of MR.

The nonlocal filters do not make any assumption on the location of pixels in the image during denoising a particular pixel. The distance between the present pixel and the neighbor pixel does not affect the weight assigned to the pixel during the restoration process. The nonlocal mean (NLM) algorithm, estimates every pixel value as a weighted normal of other comparative noisy pixels. However, the center issue with NLM is that it can't exploit the smoothness of the edge contour that can isolate the white from black areas [105]. Buades et al. [106] proposed an approach utilizing image patches for the reduction of additive noise. Coupe et al. [105] extended the Bayesian system to determine an NLM filter for reduction of speckle noise in the ultrasound images. Deledalle et al. [107] extended the NLM filter. The noise reduction process appeared to be the "weighted maximum likelihood estimation" issue. The weights were determined to utilize a data-driven process. This probabilistic patch based channel was supported for speckle noise reduction in the SAR images. Guo et al. [94] joined the maximum likelihood estimation and NLM in their proposed modified nonlocal (MNL) filter for speckle noise reduction in the echocardiographic images.

Numerous researchers have looked at the despeckling methods for different sorts of images. The performance of the despeckling filter is measured utilizing different performance parameter, for example, edge enhancing index (EEI), speckle suppression index (SSI), image detail preserving coefficient (IDPC), feature preserving index (FPI) and speckle image analysis, image quality metrics (IQM), texture feature analysis, visual quality assessment, mean square error (MSE), signal to noise ratio (SNR), peak signal to noise ratio (PSNR), β, normalized MSE (NMSE), speckle index (SI), effective number of looks (ENL), ρ, structural similarity index (SSIM) and execution time, despeckling assessment index, figure of merit (FoM), and edge region MSE, along with the visual quality [8, 108–115]. As these ultrasound images suffered from speckle, the experts with adequate experience get confused for making a conclusion in the analysis of the image. Speckle noise restrains the application of image processing and analysis algorithms such as edge detection and segmentation.

1.4.3 Overview on Characteristic Features of Echocardiographic Images

The characteristic feature extraction step is the most important and critical step. If the features are not discriminative enough, even the best classifier cannot provide good classification accuracy. The feature extraction techniques should be able to capture inter-class variations and at the same time, minimize the effect of the intra-class variations. Thus the effective feature extraction is an active area of research. Several studies have been reported in literature utilizing statistical texture descriptors such as first-order statistics (FOS) [116], gray level difference matrix (GLDM) [117], gray level difference statistics (GLDS) [118], neighborhood gray tone difference matrix (NGTDM) [119], statistical feature matrix (SFM) [120] and Laws textures energy measure (Laws TEM) [121] are extracted for classification of mitral regurgitation. Various CAD systems have been proposed using these statistical texture features [19, 122–125].

Ojala et al. [126] introduced a local texture descriptor named as the local binary pattern (LBP) that is resistive to lighting changes with low computational complexity. The uniform local binary pattern (LBP^{u2}), rotation invariant local binary pattern (LBP^{ri}) and rotation invariant uniform local binary pattern (LBP^{riu2}) are the extension of original LBP, where the dimension of the feature vector is reduced [127]. LBP has been widely used in classification problems and has given superior performances in various pattern recognition application such as face recognition and biometrics [126, 128–131]. In medical domain, LBP has been utilized to identify malignant breast cells [132], to find relevant slices in brain magnetic resonance volumes [133, 134] and as a texture feature extracted from thyroid slices [135]. Various variants of LBP have been proposed in last few years such as local directional pattern, local ternary pattern [136, 137].

Transform domain feature extraction techniques such as discrete cosine transform (DCT) [138], discrete wavelet transform (DWT) [139], Gabor transform [140, 141] are utilized in the classification framework. The multiresolution image analysis is the most popular tool to extract significant texture features from an image [142, 143]. Gaussian pyramid (GP) [144, 145] and Laplacian pyramid (LP) [146, 147] have been widely used as multiresolution schemes for texture analysis of images. Image pyramid consists of the sequence of various images of different resolution which changes in regular steps [148].

1.4.4 Overview on Feature Dimension Reduction and Feature Selection

Feature extraction methods often generate a large number of features which increase the computational cost of the CAD system. In order to enhance the performance of CAD system in terms of computational cost, dimension reduction techniques such as principal component analysis (PCA), minimal redundancy maximum relevance (mRMR) are commonly used techniques. These techniques transform a high dimensional data into lower dimensional subspace by retaining the most meaningful features to facilitate the classification task.

The PCA has found application in many different areas such as image texture feature reduction [149–153]. The major advantage of PCA includes less memory requirement for creating training set and low noise sensitivity as it retains high variance components and discards small variations, while the main disadvantage of PCA is the dependency on linear data [154]. To overcome this, Buchala et al. [155] proposed a nonlinear projection method known as curvilinear component analysis (CCA), which outperforms PCA with much lesser components. Zhang et al. [156] utilized a DWT technique to extract features and thereby dimension of features were reduced by applying PCA. Khan et al. [157] proposed a CAD system for classifying cancers to specific diagnostic categories based on their gene expression signatures using artificial neural networks (ANNs) after using PCA as feature reduction technique.

The minimal redundancy maximum relevance (mRMR) has been used by several researchers for feature selection as per their discriminative properties [158, 159]. Niaf et al. [160] proposed a CAD system for prostate cancer based on magnetic resonance (MR) imaging using support vector machine (SVM), linear discriminant analysis, k-nearest neighbors and naive Bayes classifiers. Furthermore, feature selection methods were compared based on t-test, mutual information, and mRMR criterion. Ding et al. [161] proposed a CAD system for thyroid histograms using the statistical and textural features and then the most effective and reliable features among them were selected by using an mRMR algorithm. Gomez et al. [162] investigated the co-occurrence statistics combined with six gray-scale quantization levels to classify breast lesions using ultrasound images. To reduce feature space dimensionality, the feature space was ranked using mutual information technique with mRMR criterion.

1.4.5 Overview of Classification based on Features

The final stage of every CAD system is the design of a classifier which aims to acquire knowledge of the extracted features in order to assign the severity label to the given test samples. Jain et al. [163] outlined that the selection of a classifier is a difficult task and it depends on either availability or the knowledge of the end user. Hence, researchers have used various classifiers such as support vector machine (SVM), neural network (NN), AdaBoost, k-means classification and random forest (RF) [164–169]. These systems have demonstrated capacity of performing the task with reasonable performance parameters such as classification accuracy, sensitivity, specificity, and computation time using texture features. The diverse strategies proposed for the different sicknesses have considered the US, X-beam, CT-scan and other methodology to acquire the data set.

Christodoulou et. al. [19] proposed an approach for the characterization carotid plaque into two categories, symptomatic and asymptomatic, utilizing ten different texture features sets named FOS, SGLDM, GLDS, NGTDM, SFM, Laws TEM, FDTA, FPS and shape parameters along with two classifiers i.e. modular neural network composed of self-organizing map (SOM) and k nearest neighbors (KNN). Boukerroui et al. [170] presented an approach for breast lesion segmentation utilizing DWT and gray level co-occurrence matrix (GLCM). Chen et. al. [20] proposed a CAD system for the breast cancer using texture feature, morphological feature, model-based feature, of the ultrasound images using the artificial neural network (ANN) and backpropagation neural network (BP-NN).

Obayya et al. [164] proposed a classification system using multilayer feed-forward neural network to measure the heart rate variability signals in order to discriminate between normal subjects and patients suffering from congestive heart failure (CHF). Hanbay et al. [22] proposed an expert system based on least squares support vector machines (LS-SVM) for diagnosis of valvular heart disease (VHD). Wavelet packet decomposition (WPD) and fast-Fourier transform (FFT) methods are used for feature extraction from Doppler signals. LS-SVM is used in the classification stage. Threefold cross-validation method is used to evaluate the proposed expert system performance. Maglogiannis et al. [165] proposed a CAD framework for heart valve diseases using heart sounds. This system identifies a heart sound as healthy or having a heart valve disease using the support vectors machine-based machine learning technique. Tang et al. [171] presented a review of CAD procedures for breast cancer, identification of calcifications, masses, architectural distortion, and bilateral asymmetry. Chuan et. al. [122] used gray level co-occurrence matrix, statistical feature matrix, gray level run-length matrix, Laws texture energy measures, neighboring gray level dependence matrix, wavelet features, Fourier feature based on local Fourier coefficients features along with support vector machines(SVM) to select significant textural features to classify the nodular lesions of a thyroid.

Biner et al. [51] recently reported poor agreement among expert observers for grading MR severity based on jet area, VCW, and PISA. This underlines the need for the development of more accurate, reproducible, and perhaps automated analysis. Nikolaos et. al. [172] proposed a classification approach utilizing multiresolution features for carotid atherosclerosis from the B-Mode ultrasound. Discrete wavelet transform, the stationary wavelet transform, wavelet packets (WP), and Gabor transform (GT), as well as several basis functions, have been compared in this paper and found that WP based features outperformed than others. The classification of the images was done using two classifiers, i.e., SVM and probabilistic neural networks. Virmani et. al. [173] proposed a scheme using multiresolution wavelet packet texture descriptors with mean, standard deviation and energy for characterization of liver ultrasound images. In this paper a comparison is given between Haar, Daubechies (db4 and db6), biorthogonal (bior3.1, bior3.3 and bior4.4), symlets (sym3 and sym5) and coiflets (coif1 and coif2). Gao et. al. [23] presented a CAD system for ultrasound liver images. The gray level gradient co-occurrence matrix (GLGCM) and gray level co-occurrence matrix (GLCM) features were extracted and seven most powerful features were selected for classification using back propagation neural network (BP-NN). Zhou et al. [174] proposed a texture feature descriptors based on shearlet transform to characterize breast tumors in ultrasound images using two classifiers SVM and AdaBoost.

Mandeep et. al. [123] presented a classification method for liver ultrasound images utilizing statistical texture features such as spatial gray level co-occurrence matrix, gray level difference statistics, first order statistics, Fourier power spectrum, statistical feature matrix, Laws texture energy measures and fractal features. Sun et al. [175] proposed a moving windowed Hilbert transform (MWHT), to extract the diagnostic features named as the center of gravity and the frequency width of the frequency distribution [FG, FW] and gives boundary curve models for the diagnostic features [T12, T11] to diagnose ventricular septal defects (VSD). To evaluate the detection ability of the proposed diagnostic features, a classification boundary method based on the SVM technique is proposed to determine the classifiers to diagnose the VSD sounds. Hedeshi et al. [24] proposed the use of particle swarm optimization (PSO) algorithm with a boosting approach to extract rules for recognizing the presence of coronary artery disease in a patient.

Sudarshan et. al. [124] discussed various components used to develop a CAD system with respect to myocardial infarction (MI) utilizing first-order statistics, gray-level co-occurrence matrix (GLCM), Laws texture energy (LTE), and local binary pattern (LBP) with two classifiers SVM and KNN. Gharehbaghi et al. [176] proposed a framework for binary classification of the time series with cyclic characteristics. The framework presents an iterative algorithm for learning the cyclic characteristics by introducing the discriminative frequency bands (DFBs) using the discriminant analysis along with k-means clustering method. Moghaddasi et al. [177] proposed novel feature i.e., extensive local binary pattern (ELBP) and extensive volume local binary pattern (EVLBP) to detect micro-patterns of echocardiography images in order to determine the severity of MR. Moreover, SVM, linear discriminant analysis (LDA) and template matching techniques are used as classifiers to determine the severity of MR based on textural descriptors. Balodi et al. [178] investigates the possibility to recognize the severity of MR, in a classification system utilizing statistical texture features of the regurgitant region. Liu et al. [179] proposed a CAD system for the diagnosis of cirrhosis using a deep convolutional neural network (CNN) model to extract features in order to classify using SVM into normal or abnormal cases. Sharma et al. [180] proposed a decision support system for renal disease using GLCM based statistical features and SVM classifier into normal and MRD images. Abdel et al. [181] presented a CAD system for breast cancer to detect and further classify tumors into benign and malignant ones utilizing random forest (RF) classifier.

1.5 Research Objectives

The principal objective of the present research work is to improve the diagnostic capability of conventional B-Mode ultrasound for the diagnosis of valvular diseases specifically mitral regurgitation. This objective is planned to be obtained through following steps:

1. *The collection of a comprehensive and representative image database*: Keeping in mind the end goal to create proficient and robust classifier plans, it is important to train the classifiers with an exhaustive image database with representative images from every subclass. Accordingly, the gathering of a thorough image database with delegate cases from each class, including (i) mild, (ii) moderate, and (iii) severe, is taken up as the first objective of the present research work.

2. *Despeckling of echocardiographic images*: A comparative study is required on the above-discussed despeckling filters on MR TTE images. Despeckling applications of total variation, bilateral and fuzzy concepts filters will be tested and effort would be made to improve the performance of the hybrid fuzzy filter. The despeckling techniques would be tested using image quality metrics such as the figure of merit (FOM), structural similarity (SSIM) index, and beta metric (β) along with traditional parameters.

3. *Feature extraction*: The efficiency and effectiveness of the CAD system rely on upon the nature of the texture features extracted from the MR images. Along with these lines, the accentuation in this work has been to propose feature extraction techniques for the severity analysis of MR images which are listed below:

   - Spatial domain texture feature extraction technique
   - Gaussian image pyramid based texture feature extraction technique
   - Discrete wavelet transform (DWT) based texture feature extraction technique

4. *Feature selection*: Mitral regurgitation shows unique mosaic pattern at different levels of severity. The texture patterns of TTE images would be useful in the categorization of systole further into the mild, moderate and severe classification. The proposed texture feature extraction techniques produce large complex features, and among them, several features may not be significant for discrimination of the severity of MR. Along with these lines, to diminish the feature vector data and enhance the MR severity classification accuracy a feature selection technique, minimal redundancy maximal relevance

(mRMR) and feature dimensionality reduction technique, principal component analysis (PCA) have been investigated.

5. *Classification*: The selection of classifier further enhances the efficiency of the system. Therefore, two supervised classifiers SVM (linear SVM, polynomial SVM, radial basis function (RBF) kernel SVM) and random forest RF classifier have been investigated to get the optimum classification accuracy from the CAD system.

6. *Clinical validation*: Clinical validation of the final results is one of the most challenging tasks in medical image analysis applications. Results are usually compared with the visual perception evaluation by specialists. It is true that such comparisons are often affected with the experience of the expert. However, it is relatively safe to consider automated methods as second opinions intended to aid the user. This practice has been shown to be useful in many CAD applications.

1.6 Organization of Thesis

The thesis is organized in seven chapters, that introduce the topic and states the objectives. The rest of the thesis report is organized as follows:

Chapter 2 presents the overview of the heart valve functions and the diseases. In addition, it also describes the imaging modalities employed for the assessment of valvular abnormalities. The details of the dataset sources and datasets used for the study also discussed.

Chapter 3 presents a comparative analysis of despeckling filters for the B-mode images The despeckling filters are compared using image quality metrics such as the figure of merit (FOM), structural similarity (SSIM) index, and beta metric (β) along with traditional parameters. A new improved hybrid filter is proposed and analyzed.

Chapter 4 presents the spatial domain texture analysis of MR. The performance of the texture feature extraction technique is evaluated utilizing two supervised classifiers SVM, RF and the effect of the feature reduction technique are investigated.

Chapter 5 presents the concise description of the Gaussian pyramid (GP) approach for the image decomposition. The GP-based texture feature extraction techniques are presented to get the significant features for grayscale images of MR. Finally, the efficiency of these techniques for the severity analysis of MR is presented.

Chapter 6 presents the description of the discrete wavelet transform (DWT) based texture feature extraction techniques for grayscale images of MR. The effectiveness of these techniques is evaluated in this chapter.

Chapter 7 summarizes the conclusions drawn from the exhaustive experimentation carried out in the present research work on “Analysis of mitral regurgitation using echocardiographic images. This chapter also presents the limitations of the present work and emphasizing the scope for future work in this field.

CHAPTER 2

GENESIS OF HEART FUNCTION AND DISEASES

This chapter presents the overview of the heart valve functions and the related diseases. In addition, it also describes the imaging modalities employed for the assessment of valvular abnormalities. The advantages and disadvantages of echocardiographic imaging along with the importance of acquiring images in multiple views using various acoustic windows are also discussed.

2.1 Heart Structure and Function

The heart is a muscular organ in humans and other animals, which pumps blood through the blood vessels of the circulatory system. The size of an average adult heart is about 14 cm in length and 9 cm wide. The heart has a mass of 200 to 425 grams. A normal heart beats 100,000 times in a day and pumps more than 4,300 gallons of blood throughout the body. The pericardium encompasses the heart and it is a twofold layered structure. The heart's significant veins are secured by the external layer of the pericardium. These veins are associated with different structures of the body. The pericardium's internal layer is associated with the heart muscles. A fluid covering segregates the layers of membrane and allows the dynamic movement of the heart [3, 182]. The blood flow through the chambers and valves of the heart is shown in Fig. 2.1. The heart structure contains four chambers and four valves working synchronously. The upper two chambers are known as left atrium (LA) and right atrium (RA) while the lower one is named as left and right ventricles. Left and right chambers are detached by a mass of muscle called septum. The region of the septum that partitions the atria is called inter-atrial septum and the area that separates the ventricles is called the inter-ventricular septum. The four valves of heart synchronously work to maintain the regular flow of oxygenated and de-oxygenated blood. Tricuspid valve (TV) is located between the right atrium and right ventricle. It controls the flow of blood between the right atrium and the right ventricle to pass through the pulmonary valve (PV) and thereby manages blood spill out of the right ventricle (RV) into the pulmonary arteries which carry forward blood to the lungs to get oxygen. The mitral valve (MV) located in between the left atrium and left ventricle. It is

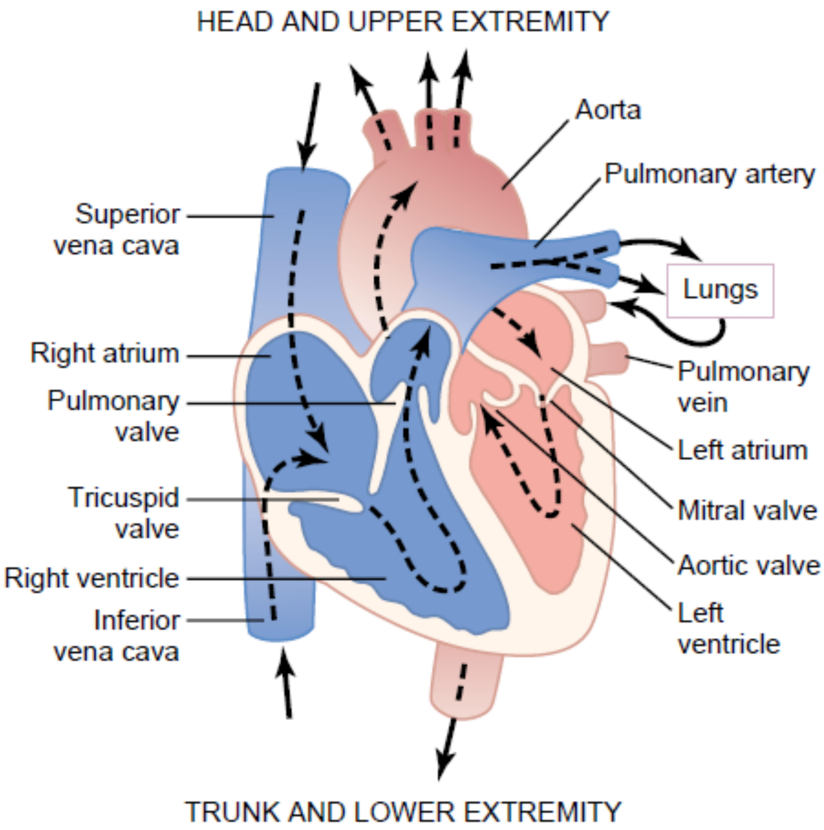

Fig. 2.1: Structure of the heart and heart valves. [3]

also known as the bicuspid valve because it has two cusps, an anterior and a posterior cusp. The blood flows through MV during diastole and systole in between LA and LV. Aortic valve (AV) is at the entrance of aorta. During ventricular relaxation, it prevents blood from moving from the aorta into the left ventricle. It permits the oxygenated blood from the left ventricle (LV) into the aorta, where from oxygenated blood is passed to the rest of the body [3, 182].

2.2 Mitral Valve Physiology

The mitral valve (MV) connects the left atrium (LA) and the left ventricle (LV) as shown in Fig. 2.2. The mitral valve opens during diastole to allow the blood flow from the LA to the LV. During ventricular systole, the mitral valve closes and prevents backflow to the LA. The MV leaflet tissues are organized in three layers: fibrosa, spongioa, and ventricularis. Table 2.1 describes location, composition, and function of these layers [3]. The normal function of the MV depends on its 6 components, which are (i) the left atrial wall, (ii) the annulus, (iii) the leaflets, (iv) the chordae tendineae, (v) the papillary muscles, and (vii) the left ventricular wall. All the valvular apparatus such as the annulus, leaflets, and sub-valvular apparatus work in a complex manner for the proper functioning of the valve.

The pressure in the LV increases during the systole or the contraction of the LV. This increased pressure leads to the closing of MV and restricts the flow of blood from leaking into the LA. At this time, the blood flows through the aortic valve to the aorta and to the body. All the valvular apparatus such as the annulus, leaflets, and sub-valvular apparatus work in a complex manner for the proper functioning of the valve.

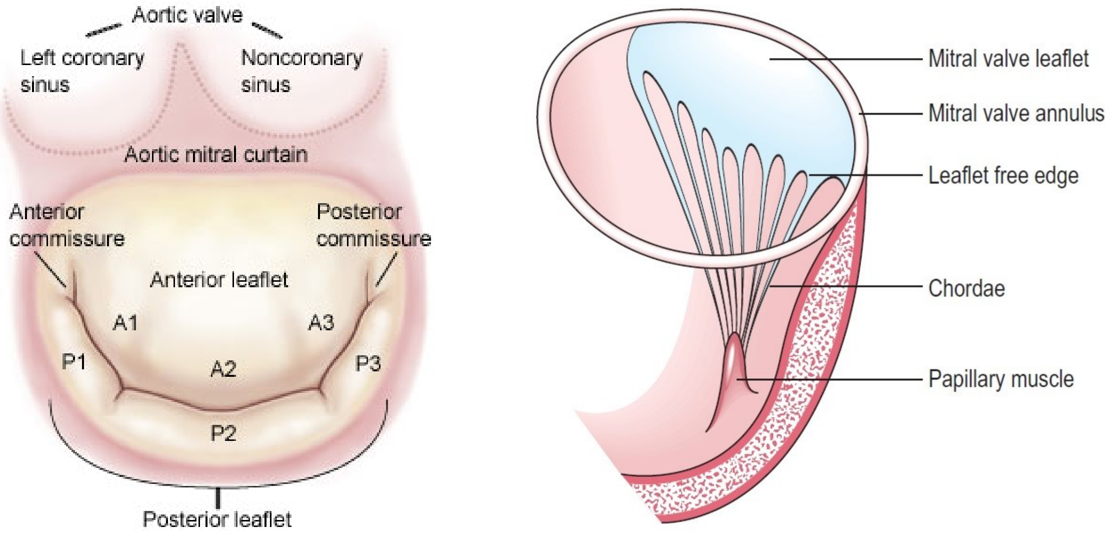

(a) (b)

Fig. 2.2: (a) Mitral valve (b) Mitral valve leaflets [3]

2.3 Mitral Valve Diseases

The heart diseases are the abnormalities which are related to the heart valves, valve functions, and the function of heart's electric conduction system, the heart muscles itself, and the coronary arteries malfunctions. Some common heart diseases are rheumatic heart disease, hypertensive heart disease, ischemic heart disease, cerebrovascular disease, and inflammatory heart disease [3, 183]. Mitral valve diseases are divided into three types:

1. Mitral Stenosis (MS): Narrowing of the MV orifice impeding the diastolic flow of blood

Table 2.1: Layers of valve tissues

Layer	Location	Composition	Function
Fibrosa	Faces the LV	High concentration of collagen, thickest layer	Bears most of the load during coaptation
Spongiosa	Middle layer	High concentration of glycosaminoglycans (GAG) and proteoglycans (PG)	Provides shear between outer support layers and diffuses gasses and nutrients
Atrials (Ventricularies for semilunar valves	Faces the LA	High concentration of collagen, and elastin thinnest layer	Elastin allows for strain when, valve is open

from the LA to LV.

2. Mitral Regurgitation (MR): The backward flow of blood from LV to LA during systole.
3. Mitral valve prolapse: This is the common condition affecting up to 5 % of the population. Posterior displacement or the anterior-posterior or both mitral valve leaflets bent towards the LA.

2.4 Mitral Regurgitation

Mitral regurgitation (MR) is the most common heart valve disorder, which affects 2% of the population [184]. It is known as the reverse blood flow from the left ventricle (LV) into the left atrium (LA) during the systole process. If MR is not progressive then the backward leakage of blood has no significant consequences. But, as this leakage increases then the LV has to work hard to fulfill the oxygenated blood demand of the body. To fulfill this increased demand, the heart muscles (myocardium and circulatory system) undergo a sequence of changes. These type of changes take a long period of time which depends on the severity of the regurgitation. Weak apparatuses are the sources of a sudden heart attack. The heart compensates for this and tries to pump harder that results in heart failure [185].

2.4.1 Causes of Mitral Regurgitation

The MR is classified as primary and secondary. The primary MR is caused by an abnormality in the mitral valve. Whereas, secondary MR is caused by an abnormality in the left ventricle of the heart. It may increase from mild to moderate to severe due to the various cardiac diseases or other heart valve abnormalities. The possible causes of MR include:

Mitral valve prolapse: The mitral prolapse may range from mild to severe due to the abnormal size or damage to the mitral valve tissues.

Infective endocarditis: Infective endocarditis is a bacterial infection of the inner lining of the heart muscle (endocardium). This inner lining also covers the heart valves, and it is these valves which are primarily affected by infective endocarditis. If the infection remains untreated, multiplying bacteria may eventually destroy the valves and result in heart failure.

Rheumatic fever: Rheumatic fever occurs due to the throat infection which further develops body illness. Inflammation of the heart valves and some more valvular complications occur because of the rheumatic fever.

Congenital heart abnormality: MR may occur in the patients having child-born abnormalities in the heart.

Trauma: When the valve chords are broken then there is a sudden displacement of the leaflets and leaflets are not able to withstand their normal position. These flailed leaflets are not able to join and allow the valvular leakage which is severe.

Other types of heart disease: Heart attacks, and muscle injuries and abnormalities may lead to MR.

2.4.2 Mitral Regurgitation Signs and Symptoms

In many cases, patients show up no symptoms of MR, Signs and indications of MR, which rely on upon its severity and how rapidly the condition creates, can include, blood flowing turbulently through the heart (heart murmur), shortness of breath (dyspnea), exhaustion, heart palpations, fluttering heartbeat, swollen feet. MR is often mild and advances gradually. There might be no manifestations for a considerable length of time and be unconscious of this condition, and it might not advance.

2.4.3 Mitral Regurgitation Diagnosis

MR may be diagnosed if a heart murmur is heard by the clinician with a stethoscope. This change in sound is due to backflow of blood through the mitral valve. Common tests to diagnose mitral valve regurgitation include an echocardiogram, electrocardiogram (ECG), chest

X-ray, cardiac MRI, exercise tests or stress tests, cardiac catheterization, and CT angiogram. An electrocardiogram and the chest radiography demonstrate left atrial enlargement or cardiomegaly. Transthoracic echocardiography is indicated for all patients with suspected MR to confirm its presence, assess etiology (e.g., the presence of mitral valve disease and leaflet prolapse, or evidence of underlying dilated cardiomyopathy), and determine its severity [186]. Evaluation of MR severity by echo requires an integrated assessment of several parameters, including etiology (primary vs. secondary), regurgitant jet size by color Doppler, regurgitant jet density by continuous wave Doppler, pulmonary vein and mitral valve inflow by pulse wave Doppler, as well as EROA (the area through which the valve leaks in systole) and regurgitant volume. Transesophageal echocardiography is indicated for patients who are not adequately imaged by transthoracic echocardiography and before surgery to assess feasibility of repair. Cardiac magnetic resonance imaging is also indicated in patients with chronic primary MR to assess LV and RV volumes, function, or MR severity and when these issues are not satisfactorily addressed by transthoracic echocardiography.

Echocardiography and Doppler have their own utility in the evaluation of extent of MR, however they exhibit their own advantage and disadvantages and limitations. Echo-Doppler is an extremely used tool for the diagnosis of MR. The mild MR can be seen in 20-40 % of the patients with structurally normal hearts. A careful inspection of the leaflet and subvalvular anatomy, along with morphology and function of the left ventricle and papillary muscles, is required for the analysis of MR. The American College of Cardiology (ACC) and the American Heart Association (AHA) have jointly given the guidelines in the area of cardiovascular diseases [186]. Table 2.2 describe these characteristics along with the use of Doppler parameters in evaluating MR severity. Doppler parameters and grading severity of MR are presented in Table 2.3. These quantitative parameters help clinicians to sub-classify the moderate regurgitation group into mild to moderate and moderate to severe.

Table 2.2: Qualitative and quantitative parameters for grading the MR severity

Parameters	Mild	Moderate	Severe
Qualitative			
MV morphology	Normal/abnormal	Normal/abnormal	Flail leaflet/ruptured PMs
Color flow MR jet	Small, central	Intermediate	Very large central jet or eccentric jet adhering, swirling and reaching the posterior wall of the LA
Flow convergence zone[a]	No, small	Intermediate	Large
CW signal of MR jet	faint/parabolic	Dense/parabolic	Dense/triangular
Semi-quantitative			
VC width (mm)	<3	Intermediate	≥ 7 (>8 for biplane)[b]
Pulmonary vein flow	Systolic dominance	Systolic blunting	Systolic flow reversal[c]
Mitral inflow	A wave dominant[d]	Variable	E-wave dominant (>1.5 m/s)[e]
TVI mit/ TVI Ao	<1	Intermediate	>1.4
Quantitative			
EROA (mm^2)	< 20	20-29; 30-39[g]	≥ 40
R Vol (mL)	< 30	30-44; 45-59[g]	≥ 60
LV and LA size and the systolic pulmonary arterial pressure[f]			

CW, continuous wave; LA, left atrium; EROA, effective regurgitant orifice area; LV, left ventricle; MR, mitral regurgitation; R Vol, regurgitant volume; VC, vena contracta.

[a] At a Nyquist limit of 50 - 60 cm/s.

[b] For average between apical four- and two-chamber views.

[c] Unless other reasons of systolic blunting (atrial fibrillation, elevated LA pressure).

[d] Usually after 50 years of age.

[e] In the absence of other causes of elevated LA pressure and of mitral stenosis.

[f] Unless for other reasons, the LA and LV size and the pulmonary pressure are usually normal in patients with mild MR. In acute severe MR, the pulmonary pressures are usually elevated while the LV size is still often normal. In chronic severe MR, the LV is classically dilated. Accepted cut-off values for non-significant left-sided chambers enlargement: LA volume, 36 mL/m^2, LV end-diastolic diameter,56 mm,LV end-diastolic volume,82 mL/m^2, LV end-systolic diameter,40 mm,LV end-systolic volume,30 mL/m^2,LA diameter,39 mm, LA volume ,29 mL/m^2.

[g] Grading of severity of organic MR classifies regurgitation as mild, moderate, or severe, and sub classifies the moderate regurgitation group into mild-to-moderate (EROA of 20 to 29 mm or a R Vol of 30 to 44 mL) and moderate-to-severe (EROA of 3039 mm^2 or a R Vol of 4559 mL) [187].

Table 2.3: Echocardiographic and Doppler parameters used in the evaluation of mitral regurgitation severity: Utility, Advantages and Limitations

Parameters	**Usefulness/advantages**	**Limitations**
LV and LA size	Enlargement sensitive for chronic significant MR, important for outcomes. Normal size virtually excludes significant chronic MR.	Enlargement seen in other conditions. May be normal in acute significant MR
MV leaflet/support apparatus	Flail valve and ruptured papillary muscle specific for significant MR	Other anormalities do not imply significant MR
Doppler parameters		
Jet area-color low	Simple, quick screen for mild or severe central MR; evaluates spatial orientation of jet	Subject to technical, hemodynamic variation; significantly underestimates severity in wall-impinging jets
VC width	Simple, quantitative, good at identifying mild or severe MR	Not useful for multiple MR jets; intermediate values require confirmation. Small values; thus small error leads tolarge % error
PISA method	Quantitative; Presence of flow convergence at Nyquist limit of 5060 cm/s alerts to significant MR. Provides both, lesion severity EROA) and volume overload (R Vol)	Less accurate in eccentric jets; not valid in multiple jets. provides peak flow and maximal EROA.
Flow quantaization PW	Quantitative, valid in multiple jets and eccentric jets. Provides both lesion severity (EROA, RF) and volume overload (R Vol)	Measurement of flow at MV annulus less reliable in calcific MV and/or annulus. Not valid with concomitant significantAR unless pulmonic site is used.
Jet profileCW	Simple, readily available	Affected by LV compliance, blood pressure, acuity
Peak E velocity in MR or TR	Simple, readily available, A-wave dominance	Influenced by LA pressure, LV relaxation, MV area, and atrial fibrillation. Complementary data only, does not quantify MR severity
Pulmonary vein flow	Simple, Systolic flow reversal is specific for severe MR	Influenced by LA pressure, atrial fibrillation. Not accurate if MR jet directed into the sampled vein

LV: Left ventricle, LA: Left atrium, CW, continuous wave, EROA: Effective regurgitant orifice area, MR: Mitral regurgitation, PISA: Proximal isovelocity surface area, PM: Papillary muscle, PR: Pulmonary regurgitation, RA: Right atrium; R Vol: Regurgitant volume [187]

2.5 Echocardiography

Echocardiograph has emerged as the essential apparatus for noninvasive evaluation of the cardiovascular system. The fundamental principles of echocardiography, including the mechanical elements of echocardiographic equipment, are the same as indicative ultrasound all in all. Nevertheless, there are parts of echocardiography that set it apart from general ultrasonography. Since the heart is a dynamic organ, and in light of the fact that echocardiography should moreover capture that movement, the comprehension of echocardiography requires an apprehension of both cardiovascular life systems and physiology.

The sound signal is characterized by two factors i.e., amplitude and frequency. The sound of a frequency higher than 20 kHz (f $>$ 20 kHz) can not be perceived by the human ear and is known as ultrasound [3]. The ultrasound signal of 1.5 MHz to 7.5 MHz is used in clinical imaging. The velocity of the sound signal varies with the nature of the propagating medium. The acoustic impedance demonstrates the measure of resistance offered to the voyaging sound wave through the medium [188]. The acoustic impedance values and attenuation effects for different biological materials are given in Table 2.4. The shorter the wavelength, the higher is the resolution while the smaller the wavelength of the ultrasound signal, the less is its penetration power.

Table 2.4: Propagation speed through various tissues

Material	Propagation speed (c) ms^{-1}	Impedance (Z) $10^6\ kgm^{-2}s^{-1}$	Attenuation coefficients (α) at 1 MHz ($dB\ cms^{-1}$)
Air	330	0.0004	1.2
Blood	1570	1.61	0.2
Brain	1540	1.58	0.9
Fat	1450	1.38	0.6
Liver	1550	1.65	0.9
Muscles	1590	1.7	1.5 to 3.5
Bone	4000	7.8	13
Soft tissue	1540	1.63	0.6
Water	1480	1.48	0.002

Ultrasound results from the property of certain crystals to transform electrical oscillations into mechanical oscillations known as piezoelectric effect. In ultrasound imaging system, the ultrasound signal is transmitted into the body by properly locating a medical ultrasound probe, these sound waves are reflected back and the machine deciphers the reflected echo by translating its strength and timing. The amplitude of the signal is the quality of the sound wave transmitted and received back. The extent of the reflected ultrasound signal decides the brightness and the intensity displayed on the computer screen forming an image of the body tissue known as ultrasonography [188–190]. In order to get proper acoustic contact, a jelly is placed between the skin and the transducer. The signals that return to the transducer give evidence of depth and intensity of reflection. These are transformed electronically into grayscale images on the ultrasound machine's screen or printed on paper. Here, high and low echo reflections are white and gray, respectively while no reflection is black.

2.5.1 Modes of Echocardiography

Echocardiography used in clinical areas can be classified into three modes: Two-dimensional (2-D, B-mode or real time), Motion or M-mode, and Doppler echocardiography (continuous wave, pulsed wave, and color flow). These different modes of echocardiography are used during each of the echocardiographic examination. One type of echocardiographic examination creates a complimentary finding from the other modes of the examination. Therefore, the different modes are performed simultaneously.

Two-dimensional Echocardiography

The 2D echocardiography plays a major role in the diagnosis of valvular abnormalities and cardiac structure-based studies. The 2D echo provides a snapshot in time of a cross-section of tissues. The continuous display of these snapshots displayed on TV screen shows 'real time imaging' of the heart chambers, valves and blood vessels. The ultrasound beam is swept across the area of interest and the probe rotates the beam at certain angles to scan the area. The reflected ultrasound produces an electrical signal, which produces a dot on the TV screen to build up a moving image from the desired area. Some of the important applications of the 2D echocardiography are: (i) study of the heart anatomy and structural relationships, (ii) study of valvular and cardiac chamber abnormalities, (iii) study of dynamics of heart in real

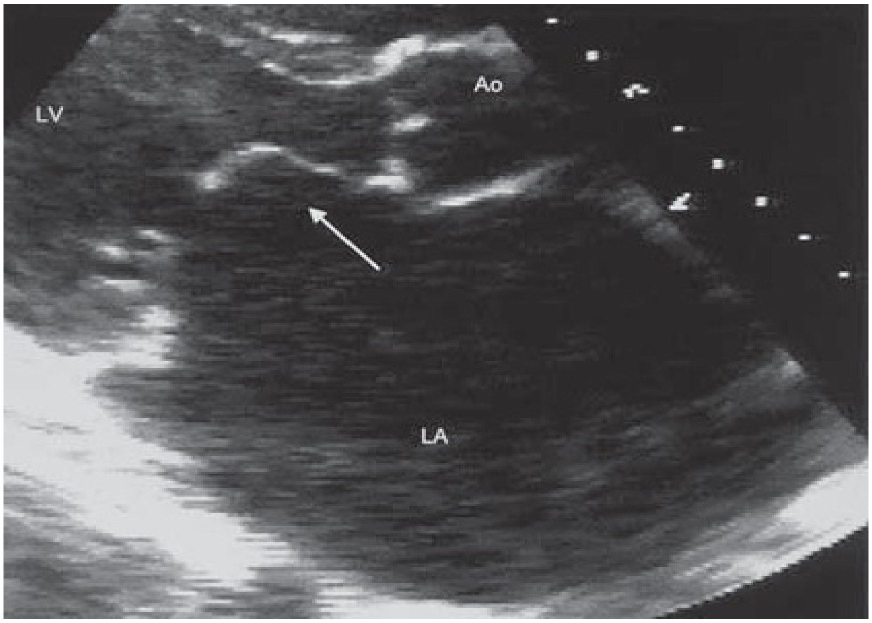

Fig. 2.3: Two-dimensional echocardiographic image of mitral valve [3]

time in different acoustic windows, (iv) computing the stroke volume, cardiac output, volume and ejection fraction, (v) study of valvular architecture like number of leaflets, size of orifice, size of leaflets, (vi) proper positioning of the M-Mode image and Doppler echo, (vii) assist in image-guided interventions and (viii) diagnosis of intracardiac masses, and pericardial diseases. Fig. 2.3 shows a 2D echocardiographic image of the mitral valve.

M-mode Echocardiography

The M-mode was the preferred imaging modality in the early days of ultrasound. M-mode is defined as a time-motion display of the ultrasound wave along a chosen ultrasound line. It provides a mono-dimensional view of the heart. All of the reflectors along this line are displayed along the time axis. The advantage of the M-mode is its very high sampling rate, which results in a high time resolution so that even very rapid motions can be recorded, displayed, and measured. The disadvantage is that the ultrasound line is fixed to the tip of the ultrasound sector. It is difficult to align the M-mode perpendicular to the structures which are displayed (i.e. the septum), thus leading to false measurements. Anatomical M-mode circumvents this limitation by reconstructing the M-mode from the 2D image (post-processing). The anatomical M-mode permits free positioning of the cursor line. However,

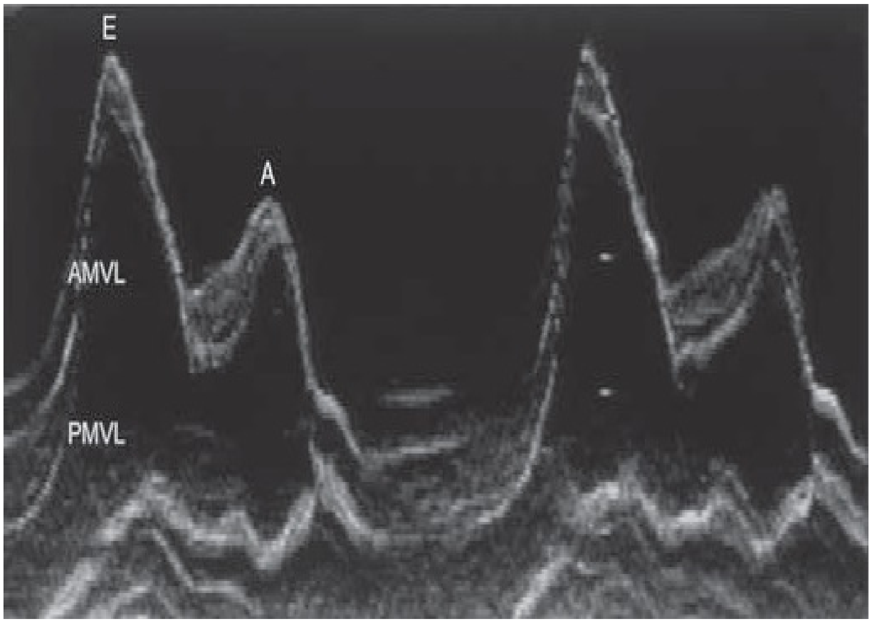

Fig. 2.4: M-mode display of the mitral valve [3]

the time resolution is significantly less than that of the conventional M-mode. There is the mitral valve, the left ventricle wall (at the level of the chordae tendineae), and the aortic root (aorta/ left atrial appendage) views that are included through the standard M-mode view as shown in Fig. 2.4.

Doppler Echocardiography

The Doppler images are used by the clinicians in routine clinical diagnosis, not as a substitute but as a complementary task. The concept of Doppler effect is employed in the estimation of blood flow velocity where the change in reflected frequency occurs due to the motion of blood cells or tissue of the cardiac structure. A shift in the frequency occurs due to the relative motion of the source, reflected and the received sound waves where the transducer used is the source and also the receiver with the red blood cells acting as the reflector. It is observed that maximum velocity information can be obtained when the ultrasound beam is aligned parallel to the direction of flow of blood. An accurate measurement of blood flow velocity is possible if the direction of blood flow is parallel to the direction of the ultrasound beam. The results are highly dependent on the transducer angle angle θ.

$$F_d = \frac{2f_0}{c} V cos\theta \tag{2.1}$$

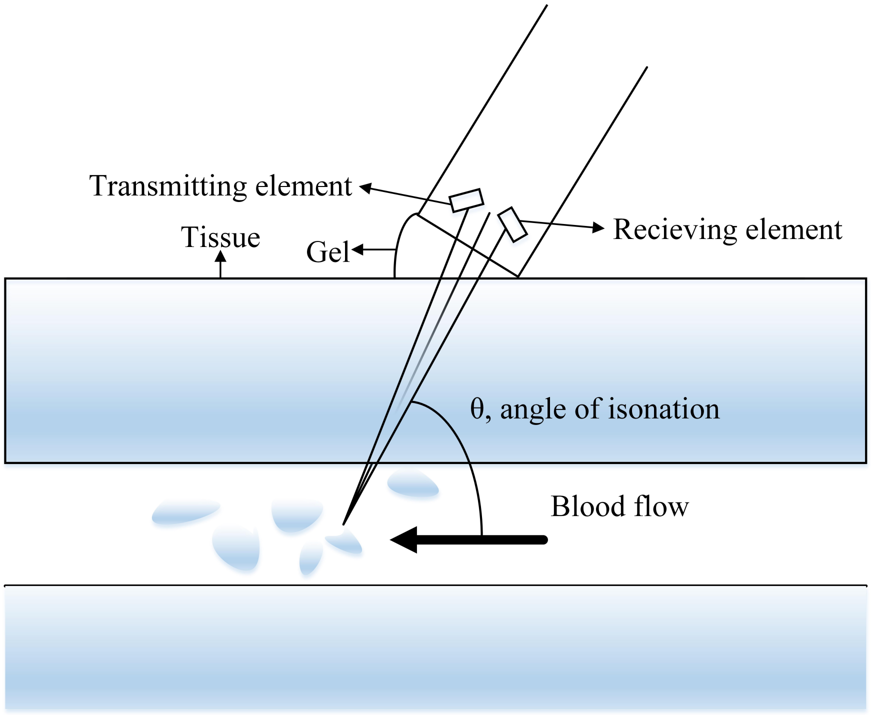

Fig. 2.5: The Doppler effect

The equation 2.1 describes the relationship that determines the blood flow velocity, where, F_d is the Doppler frequency, f_0 is the original frequency, V is the blood flow velocity, and c is the velocity of light.

Clinically, three types of Doppler echocardiography are employed (i) continuous wave (CW) Doppler, (ii) pulsed wave (PW) and Doppler and (iii) Color Flow Doppler as shown in Fig. 2.6 and color flow mapping Fig. 2.7.

In CW Doppler, dual crystals are used in order to send and receive the ultrasound waves at the same time continuously. It is useful for measuring high velocities as there is no maximum measurable velocity (Nyquist limit). A CW Doppler only offers information about the blood flow. There is no anatomic information available.

In PW Doppler, the transducer alternately transmits and receives the ultrasound data to a sample volume. It allows measuring blood velocities at a single point, or within a small window of space. It requires the ultrasound probe to send out a pulse signal to a certain depth (chosen by the operator) and then stay quiet and just listen for the reflected frequency shift from that particular depth. The computer then calculates the velocity of flow at the chosen

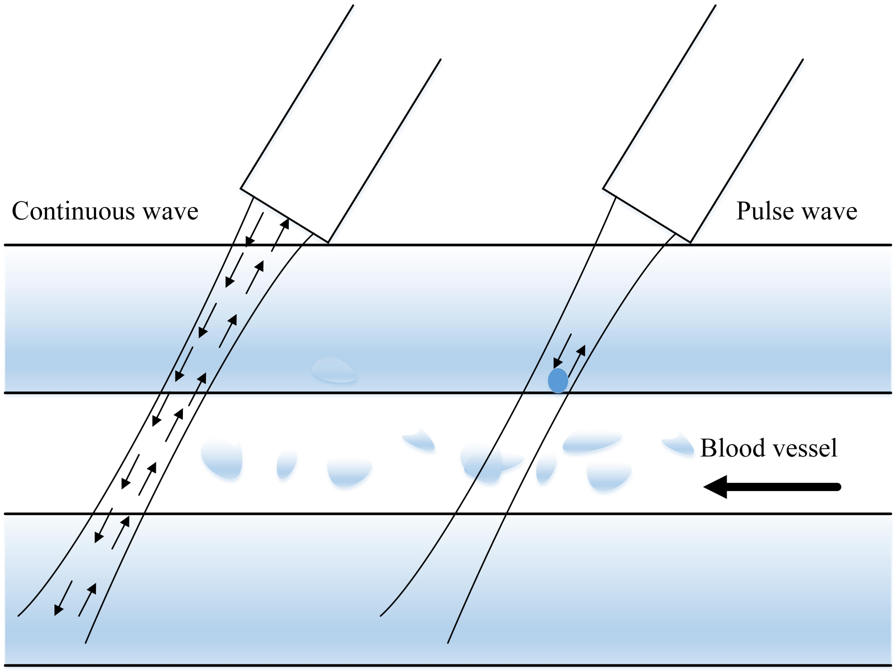

Fig. 2.6: The pulse wave and continuous wave Doppler

point. Because the machine has a waiting time to listen for a return, there is a limit to how fast it can accurately measure the velocity of blood flow. When the blood moves too fast, it cannot accurately give the velocity based on Doppler shift and a phenomenon called aliasing occurs.

Color flow Doppler echocardiography is a combination of M-mode and 2-D modalities with blood flow imaging and a type of PW Doppler echocardiography. Multiple scans can be carried out taking the multiple samples along the scan line with color flow Doppler. A color coding such as BART (blue away and red towards the transducer) is employed to differentiate the sample volumes for mean velocity and directions. The blood flow is displayed on the 2-D echocardiographic image during the MR into the left atrium at the time of systole as shown in Fig. 2.7. The colors (red and blue) in color flow imaging, represent the direction of a given color jet and the different velocities that can be represented by the hues from dull to bright. A turbulent jet shows a mosaic of many colors. A two-dimensional display of flow is shown according to the size, direction, and velocity. There is useful information in the flow map of an image. According to the direction, the red color is assigned to the flow which is towards the transducers and blue for the flow away from the transducers.

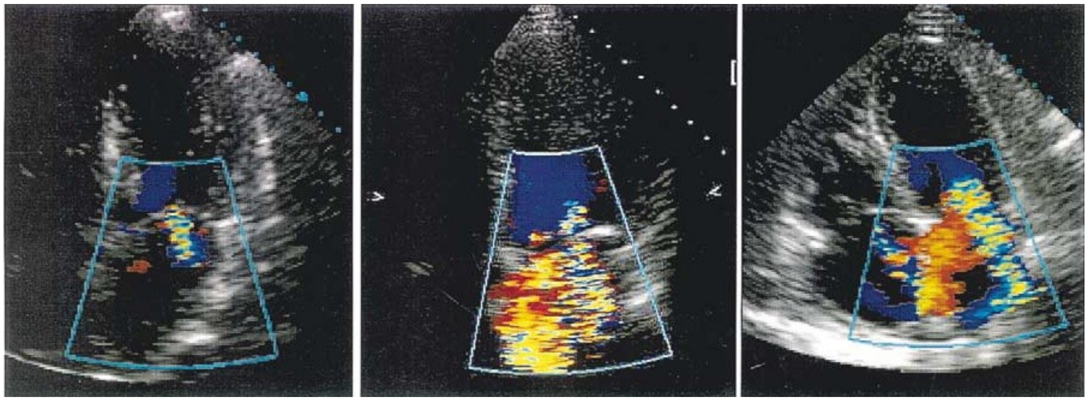

Fig. 2.7: The color flow Doppler echocardiography: Mild central MR, Severe central MR, Severe eccentric MR [3]

2.5.2 Echocardiographic Windows and Views

In transthoracic echocardiography (TTE), positions of transducer probe placed on the patient's anterior chest wall is known as echo window. This allows good penetration of the ultrasound signals without much absorption and attenuation by lung or ribs. The subject usually lies in the left lateral position and ultrasound jelly is placed on the transducer to ensure good images. There are three major echocardiographic windows, which are used in the visualization of cardiac structure, namely: parasternal window, apical window, and subcostal window. The major windows are pictorially shown in Fig. 2.8 to better understand the process of image acquisition. In the parasternal window, the images can be acquired either by

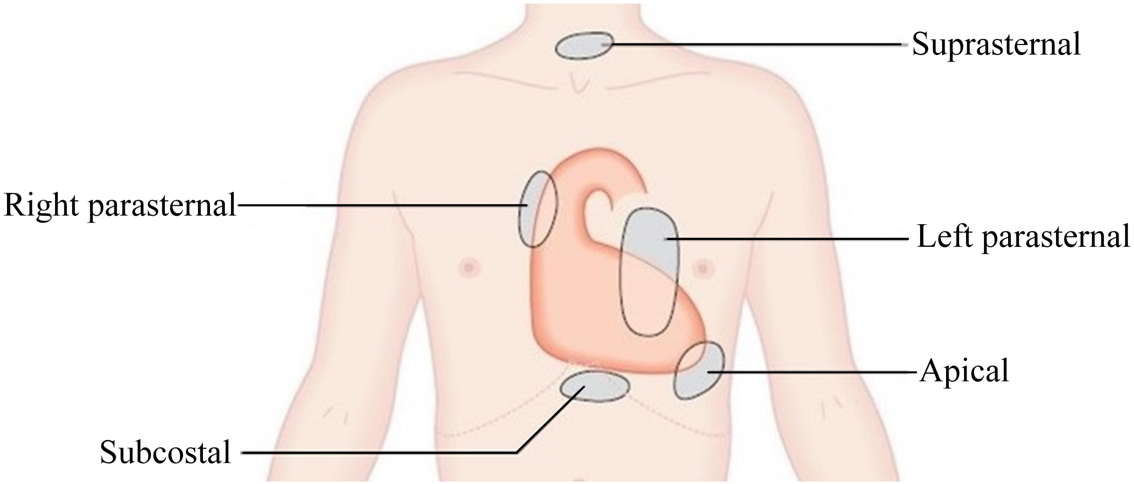

Fig. 2.8: The echo windows [3]

using long axis or short axis. In the parasternal window, the images can be acquired either using long axis or in short axis. In the short axis the image can be acquired at four levels namely: base of the cardiac structure (level of AV), the level of MV, left ventricular papillary muscles and left ventricular apex. In the apical window, the images are acquired in apical 2 chamber (A2C) view and apical 4 chamber (A4C) view.

Parasternal Long Axis (PLAX) View

The parasternal long axis (PLAX) view is used to measure the size and contractility of the right and the left ventricle. This is used to analyze the functioning of an aortic and mitral valve and to further assess the morphological and structural changes. It can also be used to observe the regurgitation mechanism and assess the severity through the color Doppler echocardiography. While acquiring the images in PLAX view, the notch on the probe should be directed towards the sternum, at 9-10 o'clock position. The transducer is used to obtain images of the heart in long axis, with slices from the base of the heart to the apex as illustrated in Fig. 2.9. The structure seen in this view include inter-ventricular septum (IVS) and posterior wall (PW), right ventricle (RV), left ventricle (LV), mitral valve (MV), aortic valve (AV), aortic root (AoR), left atrium (LA), descending aorta, and pericardium.

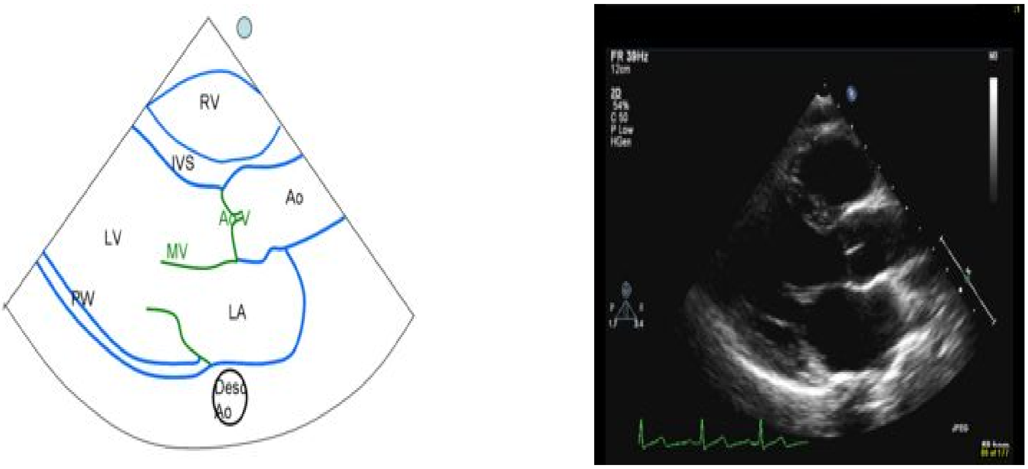

(a)

(b)

Fig. 2.9: (a) Parasternal long axis (PLAX) view (b) Mitral valve leaflets [3]

Apical Window

The images acquired using the apical window in two chamber and in four chamber view shown in Fig. 2.10. The structures seen in A4C include left and right ventricle, left and right atrium, mitral valve, tricuspid valve, interventricular (IV) and interatrial (IA) septum, LV apex, lateral wall LV, and free wall RV. In A2C view, the component that we can see include left ventricle (LV): the anterior wall, the apex and the inferior wall, mitral valve (MV): the posterior leaflet is on the left of the screen, the anterior leaflet is on the right of the screen (connected to the anterior wall of the LV) and left atrium (LA).

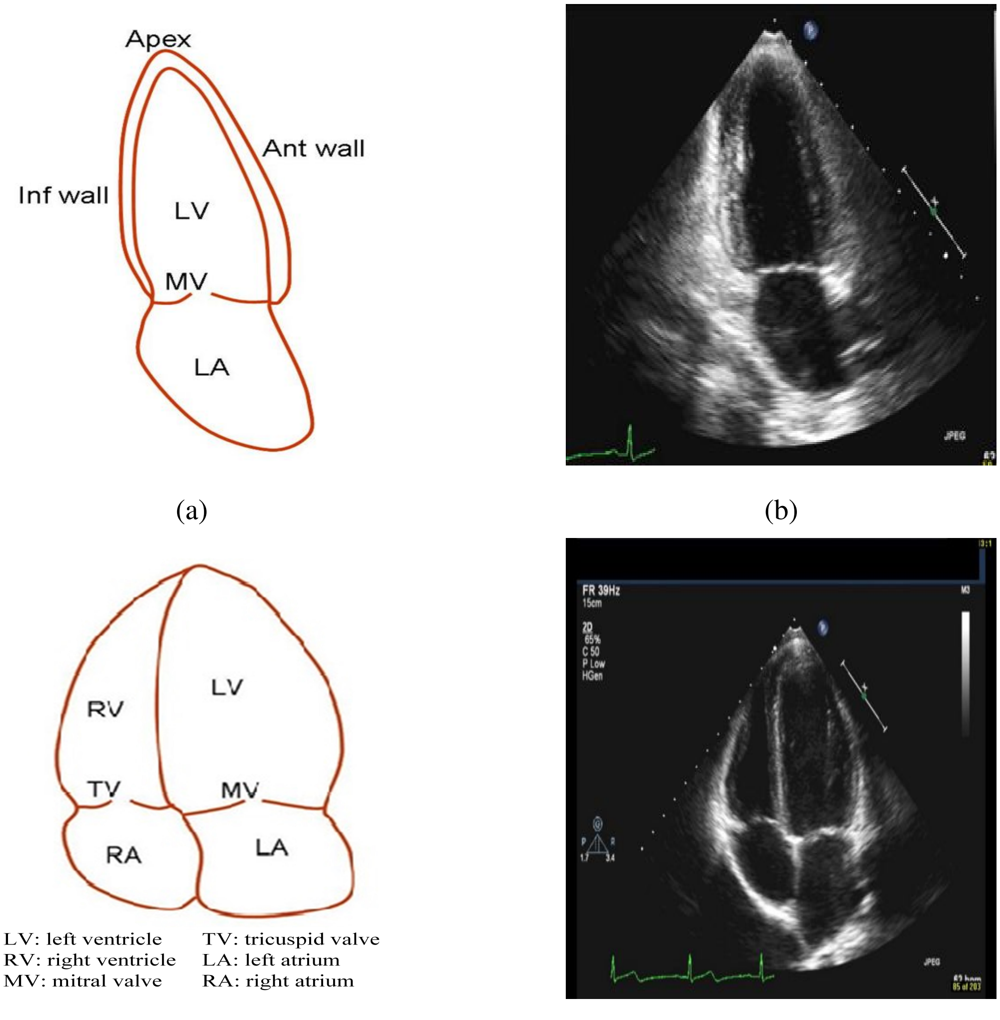

(a) (b)

(c) (d)

Fig. 2.10: (a) Apical 2 chamber (A2C), (b) Mitral valve leaflets (c) Apical 4 chamber (A4C) view (d) Mitral valve leaflets [3]

2.5.3 Advantages and Disadvantages of Echocardiographic Imaging

The echocardiography, a ultrasound imaging technique is a real-time, safe, secure, powerful, non-invasive and portable, painless, no ionizing radiation, economical, concurrent, needing no special environment and is clinically readily accessible technique, widely used in diagnosis of valvular diseases such as aortic stenosis and insufficiency because of its continuing improvements in the image quality [3].

Echocardiography is an operator-dependent technique and thus the usefulness of imaging depends on the operating skills of the technician or cardiologist trying to visualize the condition of the patient's heart. Therefore echocardiographic imaging requires rigorous training and experience. Even well-trained experts may have a high inter-observer and intra-observer variations during the diagnosis as even till date manual racing are necessary to compute the physical size of the chambers and valves [191].

2.6 Acquisition of Echocardiographic Data

In order to start the research work for the analysis of MR, the very first step is the acquisition of echocardiographic image data set. The dataset acquisition for the research work is carried out under the memorandum of understanding (MoU) between the Indian Institute of Technology Roorkee (IITR), Roorkee, India and Swami Rama Himalayan University (SRHU), Dehradun, India. SRHU ethical committee consent, cooperation, time involvement and discussion with echo experts and the researchers have helped in the problem formulation, data collection, and verification of results. This research work has been carried out by taking proper stringent measures of maintaining the level of dignity and confidence about the patients' personal details. The data collection is one of the major constraints as it depends upon the frequency of the patients visiting SRHU Dehradun, for diagnosis of valvular heart disease. Due to this, data collection takes a large span of time. In addition, the medical ethics and ethical clearance have to be followed for acquiring the data to carry out the research work.

2.6.1 Medical Ethics and Ethical Clearance

The medical ethics are fundamentally the moral qualities which must be taken after amid clinical practice and medical imaging research. Ethical guidelines show the coupling standards on scientists, radiologists and also the patients/subjects required in the exploration movement. The presented research work is identified with human healthcare and the collection of a comprehensive database of B-Mode MR, ultrasound images of various subclasses and views from different patients is absolutely important. The medical ethics committee of SRHU Dehradun approved the research proposal after examining the research problem, and following ethics has been taken in care during the research.

1. The researcher has restricted himself to the approved topic/protocol of the research and strictly adhere to the rules and regulations of the university.
2. The researcher has maintained strict confidentiality on the data information. No individual name in this process have been mentioned. Only pool results have been documented in the results.
3. The researcher has not involved in any procedure which infringe or interfere with the medical ethics.
4. The researcher has not given any input to the participating radiologists, as it may bias their opinion regarding the medical management.
5. The data collected by the researcher has been used for academic purposes only.

2.6.2 Image Dataset

The image dataset used in this study has been collected from the patients (men, women, and children) who underwent a medical examination at the Department of Cardiology, for the diagnosis of MR, during the period of August 2014 to March 2015 at SRHU, Dehradun with the help of two domain experts. The Philips ultrasound machine used in the department of cardiology at SRHU Dehradun, shown in Fig. 2.11, with transducers of 2-5 MHz range has been utilized for acquiring the data. The mitral valve can be visualized in three views, namely, apical 2 chamber (A2C), apical 4 chamber (A4C) and parasternal long axis (PLAX) as discussed in Section 2.5.2.

The A2C view shows the anterior and inferior walls of the LV. The A4C view demonstrates all four chambers (left/right ventricle and left/right atrium) of the heart. It is the best

Fig. 2.11: Ultrasound system by Philips

view to visualize the apex of the left ventricle and to study the mitral inflow (diastolic function and mitral stenosis). The PLAX view is useful for the measurement of the size of the right and left ventricle and for interpretation of valvular function. It permits us to understand the morphology and motion of the interventricular septum.

A total data of 115 patients has been accumulated utilizing transthoracic echocardiography (TEE) in the video mode for each patient in three views, namely, A2C, A4C, and PLAX. Further, these captured videos have been converted into frames. Now from each video, three

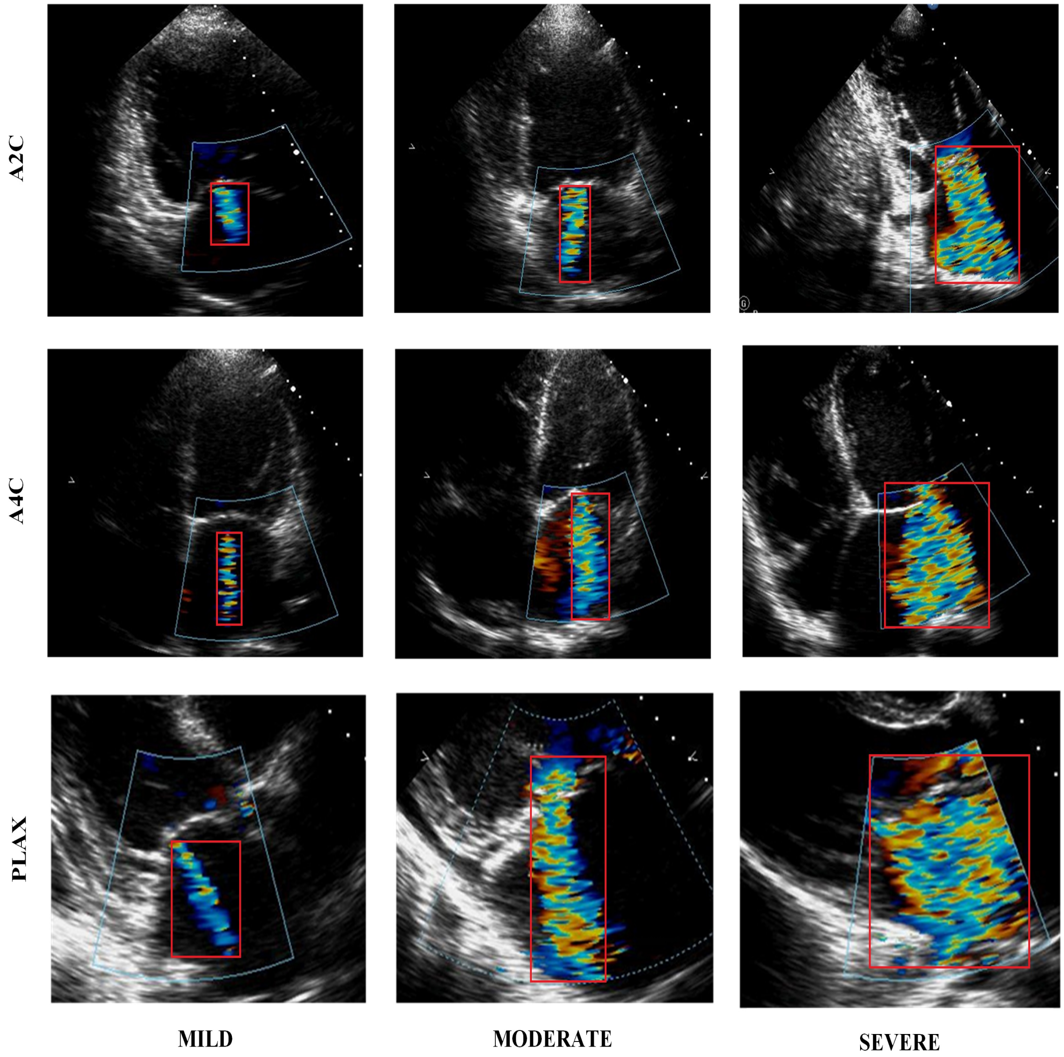

Fig. 2.12: MR severity in three views: A2C, A4C and PLAX

images from 3 cardiac cycles (systole-diastole) per patient have been taken in consultation with practicing clinicians. A total of 1035 $(115 \times 3 \times 3)$ images in the three views has been thus accumulated. The size of ultrasound images used for the analysis of MR is 800×600 pixels. The information of data collected in different views for the purpose of the study is given in the Table 2.5. A rectangular window has been selected through an arbitrary criterion which embraces the mosaic jet regurgitant area of every image in the data in a particular view for the analysis. The severity analysis has been done by tracing this mosaic pattern manually by the clinician. This mannual tracing may cause inter and intra observer error.

Table 2.5: Data collected in different windows

Views	Mild	Moderate	Severe	Total
A2C	135	140	55	330
A4C	160	115	70	345
PLAX	155	105	85	345

2.6.3 Image Assessment Protocols

The grading of the acquired images has been done by well-qualified experts independently in three classes, i.e. mild, moderate and severe as per the latest American College of Cardiology/American Heart Association (ACC/AHA) guidelines for valvular heart disease (VHD). The radiologists with good experience ensured that all the images are of diagnostic quality (free from artifacts), and confined the representativeness of each image class, such as mild, moderate and severe. The images are graded with according to the severity of MR.

2.7 Summary

This chapter presents the physiology of the heart and valves. The valvular insufficiency related to mitral valve also discussed in detail in this chapter. It is also discussed the echocardiography imaging modality, advantages and disadvantages of echocardiography, the quantitative and qualitative parameters used for the analysis of MR. This chapter gives the detail about the data set used in this work for the severity analysis of MR.

CHAPTER 3

DESPECKLING OF ECHOCARDIOGRAPHIC IMAGES

This chapter describes the despeckling filters used for speckle noise reduction in B-mode transthoracic echocardiographic (TTE) images. The chapter begins with the phenomenon of speckle formation in the ultrasound imaging, followed by noise modeling and image quality metrics (IQM). This chapter also proposed a hybrid fuzzy filter for the edge preserving despeckling filters for the TTE images and evaluated in terms of the IQM, visual quality assessment with clinical validation.

3.1 Genesis of Speckle Noise

An ultrasound based echocardiography is the first choice in the diagnosis and analysis of abnormalities related to the heart. Speckle is a granular noise that inherently exists in and degrades the quality of the active radar, synthetic aperture radar (SAR) [73, 77, 192], medical ultrasound [8, 9, 75, 193, 194] and optical coherence tomography (OCT) [92, 195] images. Its impact is much more noteworthy than additive noise sources, for example, sensor noise [194]. The speckle noise reduces the contrast resolution and masks the texture details which confines the exact interpretation and advancement of CAD systems for different diseases [8, 89, 100, 196–198]. The speckle noise reduction without decimating the image features to enhance the TTE images for precise location, diagnosis, boundary characterization and interpretation of valvular abnormality precisely in real time. A considerable amount of research has been reported in literature targeting both qualitative and quantitative despeckling techniques [8, 110, 111, 199, 200]. Individual techniques have their merits and demerits [73]. The most of the despeckling techniques have certain counter effects summarized as follows:

1. The performance of despeckling filters is sensitive to the size of kernel window. The smoothing of the output images increased with the window size. However, if the window size is small the smoothing effect is reduced but the speckle noise remains same.

2. A few despeckling techniques utilized the thresholding which is picked tentatively. The unseemly decision of the threshold may incite normal filtering and noisy boundaries, thusly leaving the sharp components unfiltered.

3. Generally, the despeckle channels do not improve the edges, they just restrain smoothing close to the edges.

3.2 Model of the Speckle Noise

Speckle is the fine-grained textural design determined in B-mode TTE images procured utilizing different acoustic windows and views. In order to analyze the despeckling techniques it is very important to have a mathematical model of speckle noise. The nature of the speckle noise is multiplicative. The output of the ultrasound imaging is given in Eq. 3.1.

$$f(i,j) = g(i,j) \cdot n(i,j) + a(i,j) \tag{3.1}$$

where, $g(i,j)$, $f(i,j)$, $n(i,j)$, and $a(i,j)$ signifies noise free image, noisy image, multiplicative noise, and additive noise, respectively, and i, j are the spatial coordinates in the two-dimensional space [95, 111, 112]. The speckle noise is caused by the random scattering phenomenon in imaging resolution cell while the additive noise caused by the sensors which is very small compared to the multiplicative noise, hence, the additive noise $a(i,j)$ generally eliminated.

$$f(i,j) = g(i,j) \cdot n(i,j) \tag{3.2}$$

A logarithmic operation convert this multiplicative noise into additive noise and the filters used for additive noise has been tested on the logarithm transformed images [112] as given in Eq. 3.3.

$$log[f(i,j)] = log[g(i,j)] + log[n(i,j)] \tag{3.3}$$

$$f_{ij} = g_{i,j} + n_{i,j} \tag{3.4}$$

where, f_{ij} = $log[f(i,j)]$, $g_{i,j}$ = $log[g(i,j)]$, and n_{ij} = $log[n(i,j)]$. The speckle noise $n(i,j)$ is modeled by Rayleigh distribution initially but after the log transformation it is estimated as the Gaussian noise. The output is obtained by taking exponential of the filtered image and the formula is given in Eq. 3.5.

$$\hat{g}(i,j) = exp\,(\text{Filter}\,(log\,(f(i,j)))) \tag{3.5}$$

where, “Filter” represents filter technique used for despeckling.

3.3 Despeckle Filters for Ultrasound Images

In this section, the despeckling filters are described in five categories: local adaptive filter or synthetic aperture radar (SAR) filters, local statistics filtering, anisotropic diffusion, nonlocal mean, and fuzzy filters.

3.3.1 Local Adaptive Filter

Adaptive filters work in the spatial domain to remove the speckle noise. They do not make any presumption related to signal and noise models. These filters have the smoothing property naturally and smoothen the edge information as well. The speckle noise is reduced by varying the size of the filter kernel window.

Lee filter [81] proposes an adaptive filter utilizing the minimum mean square error filtering criterion for the despeckling purpose. The output of this filter is visually enhanced and image structure is well preserved, but it induced blocky effect and removed sharp features. Since it does not require any transformation, it has very high efficiency.

Forst filter [84] is based on the local statistics similar to Lee filter for the removal of speckle noise in SAR images. It uses adaptive least squares estimation criterion and the denoised image is the convolution of the noisy image with a defined mask. The main disadvantage of this filter is the significant loss in image details and blurred boundaries.

Kuan filter [86] based on the different weighting function. The advantage of this filter is that it preserved the image structure. The drawbacks of this filter are over-smoothing, blurring of edges.

3.3.2 Local Statistics Filtering

In these filters the local statistics such as mean, variance, skewness, kurtosis etc. from a small fixed window around a pixel of interest to estimate the non-degraded value at that point for speckle noise reduction. The size of the local window may vary from 3 × 3 up to 15 × 15.

Linear despeckle filter (Lsmv)

These filter utilizes first order statistics such as variance and mean of the neighborhood. The algorithms of this category are based on the following equation

$$f_{i,j} = \overline{g} + k_{i,j}(g_{i,j} - \overline{g}) \tag{3.6}$$

where, $f_{i,j}$, is the modified pixel, $g_{i,j}$, is the noisy pixel, $\overline{g}$, is the mean value of image size ($N_1 \times N_2$) region surrounding and including pixel $g_{i,j}$. The weighting factor $k_{i,j}$ is a function of the local statistics given in Eq. 3.7.

$$k_{i,j} = \frac{1 - \overline{g}^2\sigma^2}{\sigma^2 + \sigma_n^2} \tag{3.7}$$

where σ and σ_n represents the variances in the moving window and the entire image respectively. A window of 5 × 5 size was considered for the filtering operation. The filter decreases the variance of speckle noise in the output image and improves the overall image quality by enhancing edges [81].

Wiener Despeckle Filter (Wiener)

Wiener filter employs a pixel wise adaptive method [84, 91, 110] executed as provided in Eq. 3.6. The weighting factor $k_{i,j}$, is given in 3.8.

$$k_{i,j} = \frac{\sigma^2 - \sigma_n^2}{\sigma^2} \tag{3.8}$$

The moving window size for the wiener despeckle filter in this study was 5 × 5 and the number of iterations set to one. The Wiener filter increases the optical perception, of the ultrasound image, but it doesn't preserve edges when compared with the lsmv filter.

Median Filter (median) despeckle Filters

The median filter [91, 110] is a nonlinear operator where the middle pixel in the window is replaced with the median value of its neighbors. Three different windows (normal window, x-shape window and cross shape window) have been utilized here and the center pixel is replaced by calculating the median of these windows. Here, the size of the window has been taken 5 × 5, and the number of iterations to each image was two. The median filter is effectively suited for enhancing the optical cognition, but repeated application destroys the image boundaries.

Non-linear Filter (Kuwahara)

This filter searches for the most homogeneous neighborhood around each pixel [201]. The center pixel of the 1 × 5 neighborhood is replaced by the median gray value of the 1 × 5 mask. The number of iterations is selected by the user. In this field, the number of iterations selected for the despeckle filter Kuwahara was set to two [110]. The Kuwahara filter is able to apply smoothing on the image while preserving the edges.

Geometric Despeckle Filter (Geometric)

The geometric filter uses a nonlinear noise reduction technique. It compares the intensity of the central pixel of 3 × 3 in the neighborhood based on their comparative values [202]. The intensity of the pixel located at the center of 5×5 window is compared with eight neighbors. Depending on the intensity values of neighborhood pixels, the value is either incremented or decreased so that the values stand out compared to others. The size of moving the window in this study is set to 5×5 with a number of iteration being equal to 2. The visual quality of the image improves on using the geometric filter but at the same time, the image is smoothed considerably also with some noisy edge retained. Some of the edges and finer details are mostly lost.

3.3.3 Non Local Mean Filter

Nonlocal means (NLM) filter was proposed by Buades [106]. In basic NLM filter the intensity value of the pixels can be related to the pixel intensity of complete image. The expression for restored intensity of a pixel is given in Eq. 3.9.

$$NL(u)(Y_i) = \sum_{y_j \in \Omega^{dim}} w(y_i, y_j).u(y_j) \tag{3.9}$$

where, $w(y_i, y_j)$ represents the weight given to $u(y_j)$ in order to reinstate the pixel y_i. The $w(y_i, y_j)$ estimates the similarity between (y_i and y_j) with constraints such as $w(y_i, y_j) \in [0, 1]$, $\sum_{y_j \in \Omega^{dim}} w(y_i, y_j) = 1$. These weights are calculated as given in Eq. 3.10.

$$w(y_i, y_j) = \frac{1}{Z_i} e^{-\frac{\left\| u(N_i) - u(N_j) \right\|_{2,a}^{2}}{h^2}} \tag{3.10}$$

where, N_i and N_j are intensities of local neighborhood centers on pixels y_i and y_j, Z_i represents the normalization constant and h is degree of filtering which controls the decay of the exponential function. The NLM algorithm is computational complex. To address this issue, an optimized implementation of the NLM filter, block wise NLM (BNLM) was proposed [105]. Further, probabilistic early termination (PET) based Fast NLM [203] was introduced to reduce the computational complexity.

3.3.4 Anisotropic Diffusion Filter (AD)

Perona and Malik [96] presented the anisotropic dispersion (AD) method for additive noise. This filter reduced the limitations of spatial filtering by significantly reducing the speckle noise and improves the image quality. This method stimulates diffusion in the homogeneous region and bound at edges. The advantage of this method is intra-region smoothing, edge conservation. But it degrades image contrast and blur edges. It uses the concept of heat diffusion and the mathematical model is taken up from the second order partial differential heat equation can be expressed as given in Eq. 3.11.

$$\frac{\partial s(x,y;t)}{\partial t} = div(g\left\|\nabla s(x,y;t)\right\|)\cdot\nabla s(x,y;t) \tag{3.11}$$

where, div is the divergence operator and $g(.)$ is the diffusion parameter. The coefficient $(g\left\|\nabla s(x,y;t)\right\|)$ varying normally in the range of [0, 1] allows the controlling of the diffusion regularization process more accurately. If g is a constant parameter, i.e. independent of image position (x, y) or time t, it leads to a linear diffusion equation as written in Eq. 3.12.

$$\frac{\partial s}{\partial t} = div(g\cdot\nabla s(x,y;t)) = g\nabla^2 s(x,y;t) \tag{3.12}$$

To preserve the edges, Perona and Malik also suggested two diffusion parameters that can be expressed as in Eq. 3.13.

$$g(\|\nabla s(x,y;t)\|) = \frac{1}{1+\left(\frac{\|\nabla s(x,y;t)\|}{K}\right)^2} \tag{3.13}$$

$$g(\|\nabla s(x,y;t)\|) = exp\bigg(-\bigg[\frac{\|\nabla s(x,y;t)\|}{K}\bigg]\bigg)^2 \tag{3.14}$$

where, K is the edge magnitude parameter which is responsible for the response of AD filter. if $\|\nabla s(x,y;t)\| \gg K$, then the diffusion coefficient becomes zero $(g(\|\nabla s(x,y;t)\|) \rightarrow 0)$ and we achieve all pass filter. On the other hand, if $\|\nabla s(x,y;t)\| \ll K$, then the diffusion coefficient becomes one $(g(\|\nabla s(x,y;t)\|) \rightarrow 1)$ and becomes isotropic diffusion.

Speckle Reducing Anisotropic Diffusion Filter (SRAD)

The isotropic diffusion filter enhance the speckle noise rather to reduce it. Yu et. al. [7] proposed an adaptive method based on partial differential equation named as speckle reducing anisotropic diffusion (SRAD). It is outlined by first representing the discrete form of the AD equation by replacing the diffusion coefficient $g\big((\nabla s(x,y;t))_p\big)$ with the instantaneous coefficient of variation (ICOV) and it can be written as in Eq. 3.15.

$$s(x,y;t+\Delta t) = s(x,y;t) + \frac{\Delta t}{|\eta_{i,j}|} \sum_{p\in\eta_{i,j}} g\big((ICOV(x,y;t))_p\big) \cdot \big((\nabla s(x,y;t))_p\big) \tag{3.15}$$

and,

$$g(ICOV) = \frac{1}{1+\left(\frac{ICOV^2 - ICOV_0^2}{ICOV_0^2 + ICOV_0^4}\right)} \tag{3.16}$$

$$g(ICOV) = exp\left[-\left(\frac{ICOV^2 - ICOV_0^2}{ICOV_0^2 + ICOV_0^4}\right)^2\right] \tag{3.17}$$

where, $|\eta_{i,j}|$ is the total number of the pixels in the spatial neighborhood of the pixel $\eta_{i,j}$ and δt is the time step parameter. The $ICOV_0$ is speckle scale function that effectively controls the amount of smoothing applied to an images by SRAD. The $ICOV$ estimated in terms of the approximations to the derivatives of s in the given 3 × 3 template can be written as in Eq. 3.18

$$ICOV = \sqrt{\frac{\left(\frac{1}{2}\right)\left(\frac{\|\nabla s\|}{s}\right)^2 - \left(\frac{1}{4}\right)^2\left(\frac{\nabla^2 s}{s}\right)^2}{1+\left(\frac{1}{4}\right)^2\left(\frac{\nabla^2 s}{s}\right)^2}} \tag{3.18}$$

This $ICOV$ combines a normalized gradient magnitude operator and a normalized Laplacian operator to act like an edge detector for a noisy image. The speckle scale function is also estimated by Eq. 3.19:

$$ICOV_0 = \frac{1.4826 \times MAD(\nabla I)}{\sqrt{2}} \tag{3.19}$$

where, MAD stands for the median absolute deviation. The divergence can be iteratively calculated as follows with the time step size of δt and sufficiently small spatial step size of $d = 1$ in x and y direction within a template having size of 3 × 3 at iteration t.

$$f(x,y;t) = \frac{1}{d^2}\begin{bmatrix} g(x+1,y;t)(s(x-1,y;t) - s(x,y;t)) \\ +g(x-1,y;t)(s(x+1,y;t) - s(x,y;t)) \\ +g(x,y+1;t)(s(x,y+1;t) - s(x,y;t)) \\ +g(x,y-1;t)(s(x,y-1;t) - s(x,y;t)) \end{bmatrix} \tag{3.20}$$

The final SRAD update function results is given in Eq. 3.21

$$s(x,y;t+1) = s(x,y;t) + \frac{\Delta t}{4} f(x,y;t) \tag{3.21}$$

3.3.5 Fuzzy Filter

In the fuzzy filter, the center of the filtered image is the normalized sum of the weighted input pixels of the moving window. These filters are based on different membership function [204, 205]. These filters are analyzed in the logarithmic domain. The output of fuzzy filters for the input $f(i,j)$ is estimated using the Eq. 3.22

$$y(i,j) = \frac{\sum_{(r,s)\in A} F[f(i+r,j+s)].f(i+r,j+s)}{\sum_{(r,s)\in A} F[f(i+r,j+s)]} \tag{3.22}$$

where, $F[f(i,j)]$ is the window function defined in terms of fuzzy membership functions and "A" is the area. Based on the different window functions, fuzzy filters can be triangular function with median center (TMED) and moving average (TMAV). Similarly, with asymmetrical triangular function with median (ATMED) center and moving average (ATMAV) center. The fuzzy filter with a triangular function and median value within a window as the center value is given in Eq. 3.23

$$F[f(i+r,j+s)] = \begin{cases} 1 - \frac{\left|f(i+r,j+s) - f_{med}(i,j)\right|}{f_{mm}(i,j)} \\ \quad \text{for} \quad \left|f(i+r,j+s) - f_{med}(i,j)\right| \leqslant f_{mm}(i,j) \\ 1 \quad \text{for} \quad f_{mm} = 0 \end{cases} \tag{3.23}$$

$$f_{mm}(i,j) = max[f_{max}(i,j) - f_{med}(i,j), f_{med}(i,j) - f_{min}(i,j)] \tag{3.24}$$

where, $f_{max}(i,j)$, $f_{min}(i,j)$, and $f_{med}(i,j)$ represent the maximum, minimum, and median values, respectively, with $s, r \in A$, the window at indices (i,j).

The fuzzy filter with a triangular function and moving average value within a window as the center value is given in Eq. 3.25

$$.F[f(i+r,j+s)] = \begin{cases} 1 - \frac{\left|f(i+r,j+s) - f_{mav}(i,j)\right|}{f_{mm}(i,j)} \\ \quad \text{for} \quad \left|f(i+r,j+s) - f_{mav}(i,j)\right| \leqslant f_{mv}(i,j) \\ 1 \quad \text{for} \quad f_{mv} = 0 \end{cases} \tag{3.25}$$

$$f_{mv}(i,j) = max[f_{max}(i,j) - f_{mav}(i,j), f_{mav}(i,j) - f_{min}(i,j)] \tag{3.26}$$

where, $f_{max}(i,j)$, $f_{min}(i,j)$, and $f_{mav}(i,j)$ represent the maximum, minimum, and moving average values, respectively, with $s, r \in A$, the window at indices (i,j).

The median filtering using fizzy asymmetrical triangulation membership function with median center (ATMED) is given in Eq. 3.27.

$$F[f(i+r,j+s)] = \begin{cases} 1 - \dfrac{\left|f_{med}(i,j) - f(i+r,j+s)\right|}{f_{mm(i,j)}} - f_{min}(i,j) \\ \quad \text{if} \quad f_{min}(i,j) \leqslant f(i+r,j+s) \leqslant f_{med}(i,j) \\ 1 - \dfrac{\left|f(i+r,j+s) - f_{med}(i,j)\right|}{f_{max}(i,j)-f_{med}(i,j)} - f_{min}(i,j) \\ \quad \text{if} \quad f_{med}(i,j) \leqslant f(i+r,j+s) \leqslant f_{max}(i,j) \\ 1 \quad \text{if} \quad \begin{array}{l} f_{med(i,j)} - f_{min}(i,j) = 0 \; or \\ f_{max}(i,j) - f_{med}(i,j) = 0 \end{array} \end{cases} \tag{3.27}$$

3.4 Proposed Hybrid Fuzzy Filter

In the proposed work, a new despeckling approach is proposed by embedding the NLM filter with homomorphic fuzzy (HF) filter and tested on ultrasound images of MR. The fuzzy filters are acceptable in the logarithmic domain but the edges are not preserved. The NLM filters are very good in term of edge preservation when used for speckle noise reduction. Therefore the edge preservation capability of NLM is integrated with the fuzzy filters. The proposed technique is termed as a hybrid fuzzy filter (HFF). The proposed technique is depicted in Fig. 3.1.

The steps incorporated in the proposed approach are step-wise described below:

Step 1: Consider standard noise free image, resize the image to 512 × 512, convert it to gray scale and embed each of the images with synthetic speckle noise.

Step 2: Project the noisy image into the logarithmic space according to Eq. 3.3. The output is of the form $f = log(double(f) + 1)$; where f is the noisy image.

Step 3: Fuzzy filters (TMED, TMAV, and ATMED) have been applied to the noisy image in logarithmic space.

Step 4: The output of the fuzzy filter is projected back to the nonlogarithmic domain using Eq. 3.4. It is represented by $g = exp(y) - 1$, where y is the output of the fuzzy filter.

Step 5: The output image at step 4 is given as input to NLM filter.

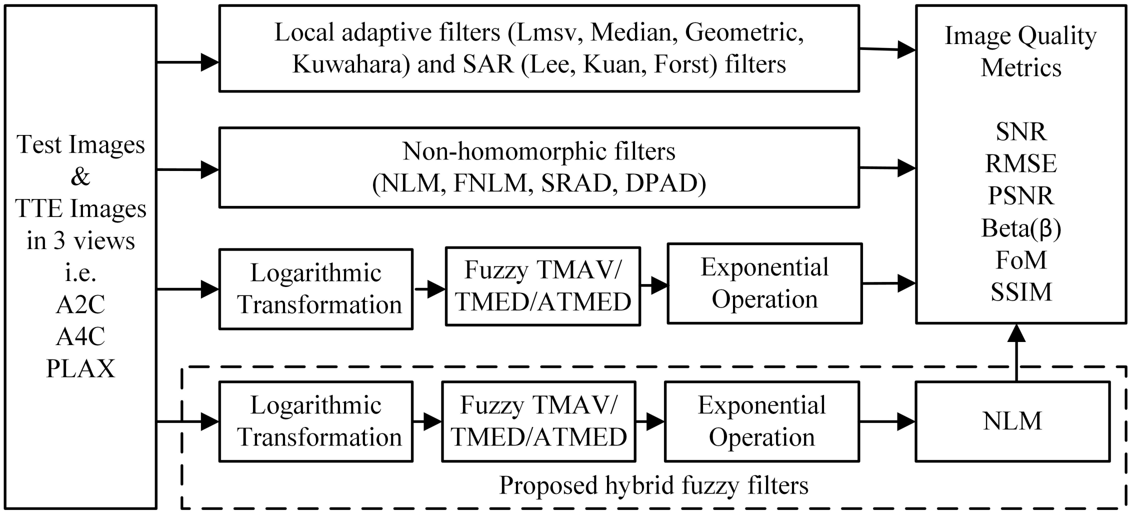

Fig. 3.1: Flow diagram of proposed methodology

Step 6: Finally, the output of the last step is the denoised image and the performance parameter and visual quality assessment have to perform.

3.5 Image Quality Metrics for Performance Evaluation

A large number of the researchers have utilized standard full reference-based measurements for assessing the execution of the despeckling filters. These parameters required the reference image or noise free image. These parameters includes signal to noise ratio (SNR) [73], peak signal to noise ratio (PSNR) [112], mean square error (MSE) [8, 112], normalized mean square error (NMSE), structural similarity index (SSIM) [8, 111, 115, 206], and root mean square error (RMSE). The ultrasound images inherently suffered from speckle noise, so noise free ultrasound images are not available for reference. These traditional parameters may not reflect the true performance in case of the clinical images.

The possible solution to this problem would be to use parameters such as speckle suppression index (SSI) [94, 207], speckle suppression and mean preservation index (SMPI), correlation coefficient (ρ), normalized correlation coefficient (NCC), Laplacian mean square error (LMSE), and normalized error summation (Err3, Err4) [8, 111]. The edge preservation is estimated by calculating the Prats figure of merit (FoM) [8], beta metric (β) and image quality index (IQI). These parameters do not require noise-free image as a reference for computing the performance. The SNR indicates the amount of reduction in noise after denoising, while PSNR measures the difference between original and despeckled image. The SNR evaluates the level of speckle as the proportion of mean to the standard deviation of the amplitude values. The FoM measure the displacement of edge details between original and denoised image. The structural similarity between the two images is given by SSIM and it ranges between 0-1, where, unity represent the identical images. The beta (β) lattices had utilized for assessing edge preservation, the SSI, and SMPI for speckle suppression and EPI for evaluating edge preservation. The MSE measures the change in average intensity after filtering. The NCC is the measure of arrangement prior and then afterward despeckling. The details of these parameters are available in [8, 94, 109, 111, 112, 115, 207, 208].

$$PSNR(f_{den}, f_{org}) = 20 \times log_{10} \left[\frac{255}{\sqrt{MSE(f_{den}, f_{org})}} \right] \tag{3.28}$$

$$MSE(f_{den}, f_{org}) = \frac{1}{MN} \sum_{i=1}^{M} \sum_{j=1}^{N} (f_{den} - f_{org})^2 \tag{3.29}$$

$$FoM(f_{den}, f_{ref}) = \frac{1}{max(N_{den}, N_{ref})} \sum_{j=1}^{N_{den}} \frac{1}{1 + \gamma d_j^2} \tag{3.30}$$

$$\beta = \frac{D(\Delta f_{den} - \overline{\Delta} f_{den}, \Delta f_{org} - \overline{\Delta} f_{org})}{\sqrt{D(\Delta f_{den} - \overline{\Delta} f_{den}, (\Delta f_{den} - \overline{\Delta} f_{den}).D(\Delta f_{org} - \overline{\Delta} f_{org}, (\Delta f_{org} - \overline{\Delta} f_{org})}} \tag{3.31}$$

$$SSIM(f_{org}, f_{den}) = \frac{1}{M} \sum \frac{(2\mu_{org}\mu_{den} + C_1)(2\sigma_{org}\sigma_{den} + C_2)}{(\mu_{org}^2 + \mu_{den}^2 + C_1)(\sigma_{org}^2 + \sigma_{den}^2 + C_2)} \tag{3.32}$$

$$SSI = \frac{\sqrt{VAR(f_{den})}}{Mean(f_{den})} \frac{Mean(f_{org})}{\sqrt{VAR(f_{org})}} \tag{3.33}$$

$$SMPI = Q \frac{\sqrt{VAR(f_{den})}}{\sqrt{VAR(f_{org})}} \tag{3.34}$$

with,

$$Q = K + |Mean(f_{den}) - Mean(f_{org})|$$

$$K = \frac{max(Mean(f_{den})) - min(Mean(f_{den})}{Mean(f_{org})}$$

$$SNR = 10\log_{10}\frac{\sum_{i=1}^{M}\sum_{j=1}^{N}(f_{den}^2(i,j)\ +\ f_{org}^2(i,j)}{\sum_{i=1}^{M}\sum_{j=1}^{N}(f_{den}(i,j)\ -\ f_{org}(i,j))^2} \tag{3.35}$$

where, γ is the penalization factor and have fixed value 1/9, n_d and n_r are the number of pixels in original and processed images respectively, d_j is the Euclidean distance, Δf_{den} and $\Delta forg$ represent the filtered version of original and processed images, pixel mean intensities in the region Δf_{den}, $\Delta forg$ are represented by $\overline{\Delta} f_{den}$ and $\overline{\Delta} f_{org}$ respectively, c_1 and c_2 are constants, $\sigma f_{org}, \sigma f_{den}$ and $2\mu f_{org}, \mu f_{den}$ are the standard deviations and means of TTE images compared, $\sigma_{f_{org}f_{den}}$ represents the covariance, $c_1, c_2 \leq 1$ are the constants, N_{den} and N_{ref} are the number of pixels in original and processed images respectively. $C_1 = (K_1L)^2, C_2 = (K_2L)^2$, where L is the dynamic range of pixel intensities (255, for 8 bits gray-scale images), $K_1, K_2 \ll 1$.

3.6 Experimental Results and Discussions

The despeckling filters has been evaluated utilizing standard test images and clinical echocardiographic images. These filters are investigated by utilizing image quality measurements and furthermore the visual quality of the despeckled images are confirmed by the experts. The MATLAB in-built function “imnoise” is utilized to add speckle noise with variance 0.01-0.1 to the test images, whereas, echocardiographic images are inherently noisy. The filter parameters being utilized in the implementation of filters are tabulated in Table 3.1.

The image quality metrics discussed in Section 3.5 are tabulated in Table 3.2, for two test images one is standard test image and second is synthetic image using homomorphic fuzzy (HF) filters (TMED, TMAV, and ATMED), along with NLM filter.

As it can be observed from the Table 3.2 that the performance of the fuzzy filters and NLM filter degraded with the increase in noise variance for the two test images. The outcomes demonstrate that the NLM filter is better than the other three filters followed by HF filter based on ATMED regarding traditional performance parameters such as PSNR, MSE, and SNR. It is additionally observed that SSIM and FoM for TMAV filter are better than other three filters while as far as beta (β) and NCC, the NLM filter performs extraordinary contrasted with rest channels. The higher the estimations of SSIM and FoM show lesser distortion and higher edge preservation in the denoised image. Comparative examinations are carried on TTE

Table 3.1: Parameters used in implementation of despeckling filters

Category	Filter Name	Abbreviation	Parameters
Local Adaptive	Local statistics mean variance	Lsmv	Window size = 5×5, iterations = 2
	Wiener	Wiener	Window size = 5×5, iterations = 1
	Median	Median	Window size = 5×5, iterations = 2
	Kuwahara	Kuwahara	Window size = 5×5
	Geometric despeckle filter	Geometric	Window size = 3×3
Synthetic aperture radar (SAR)	Lee	Lee	Window size = 5×5
	Forst	Forst	Window size = 5×5
	Kuan	Kuan	Window size = 5×5
Anisotropic diffusion	Anisotropic diffusion filter	PMAD	Diffusion constant = 30, rate of diffusion = 0.25, iteration = 20
	Speckle reducing anisotropic diffusion filter	SRAD	Diffusion constant = 30, time step = 0.02, ρ = 1
Non local mean	Non local mean	NLM	
	Fast non local mean	FNLM	
Fuzzy	Triangular function with median center	TMED	Window size = 3×3
	Triangular moving average center filter	TMAV	Window size = 3×3
	Asymmetrical triangular function with a median filter	ATMED	Window size = 3×3
Proposed	Hybrid fuzzy filter (TMAV + NLM)	HFF1	
	Hybrid fuzzy filter (TMED + NLM)	HFF2	
	Hybrid fuzzy filter (ATMED + NLM)	HFF3	

images without adding speckle noise and it is observed that the outcomes are like those cited above for standard test images.

In the local statistics based filters, the denoised image goes blurry as the window size

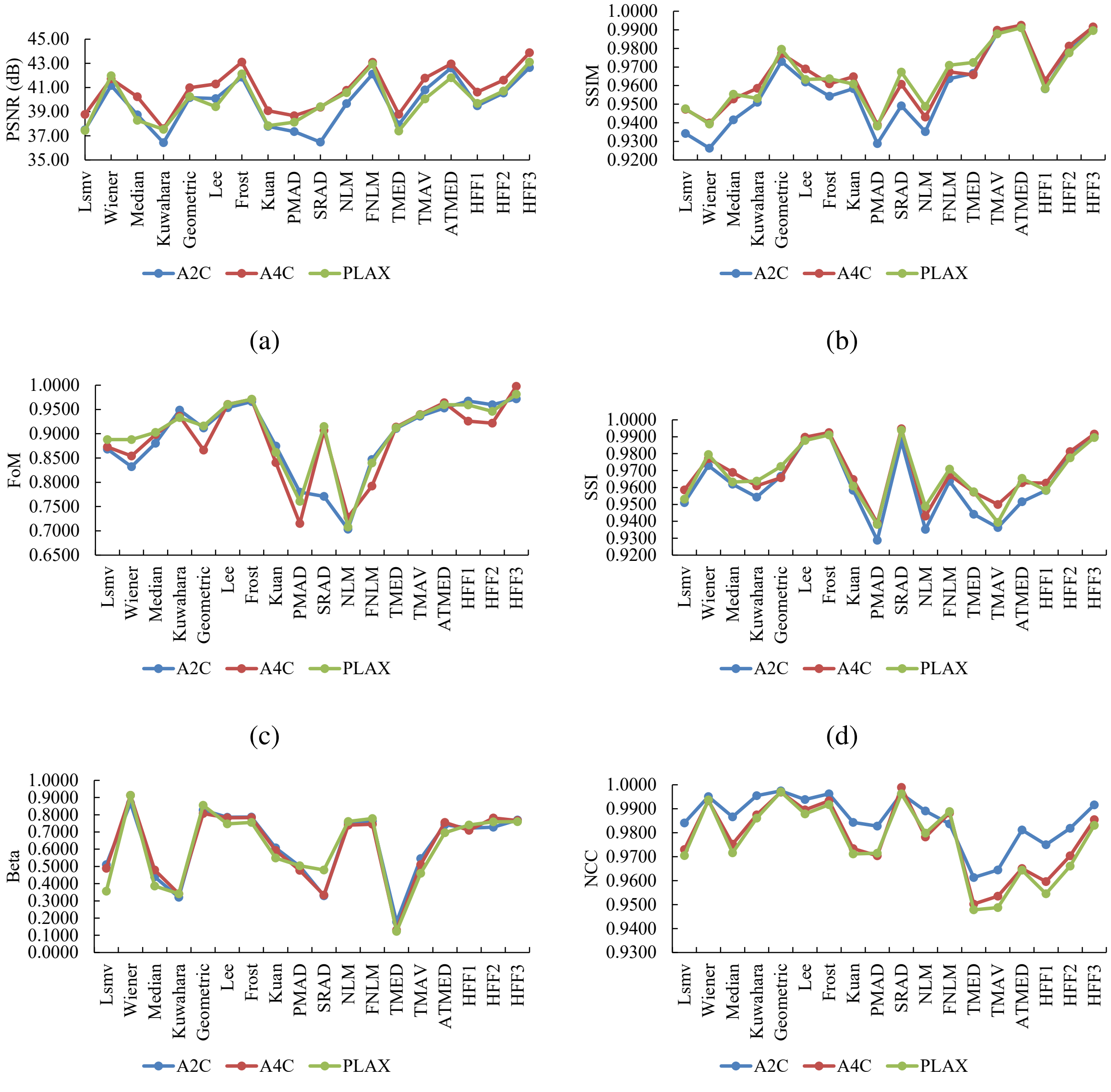

(a) (b)

(c) (d)

(e) (f) NCC

Fig. 3.2: Comparison for performance parameters for TTE images (a) PSNR (b) SSIM (c) FoM (d) SSI (e) Beta (β) (f) NCC

(a) Original image (b) Noisy image (c) Lsmv (d) Wiener

(e) Median (f) Kuwahara (g) Geometric (h) Lee

(i) Frost (j) Kuan (k) NLM (l) FNLM

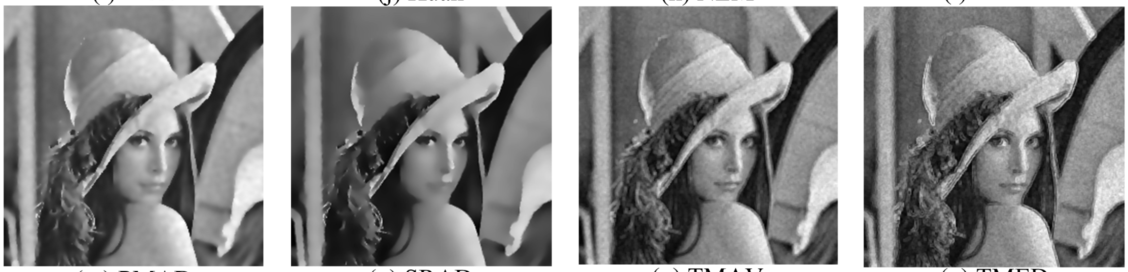

(m) PMAD (n) SRAD (o) TMAV (p) TMED

(q) ATMED (r) HFF1 (s) HFF2 (t) HFF3

Fig. 3.3: Visual quality comparison of denoised Lena image for noise level equal to 0.01 using different filters

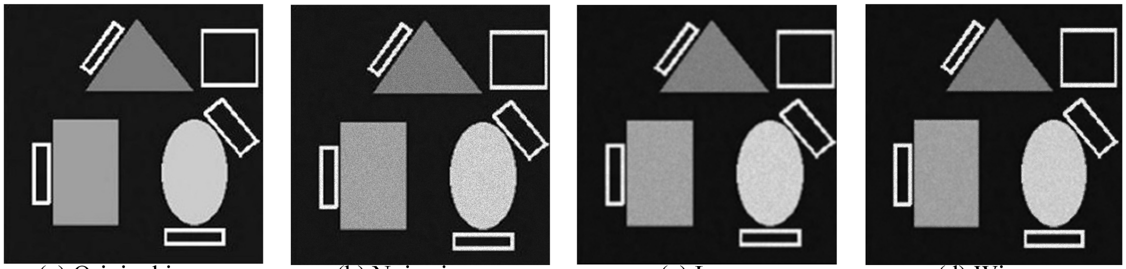

(a) Original image (b) Noisy image (c) Lsmv (d) Wiener

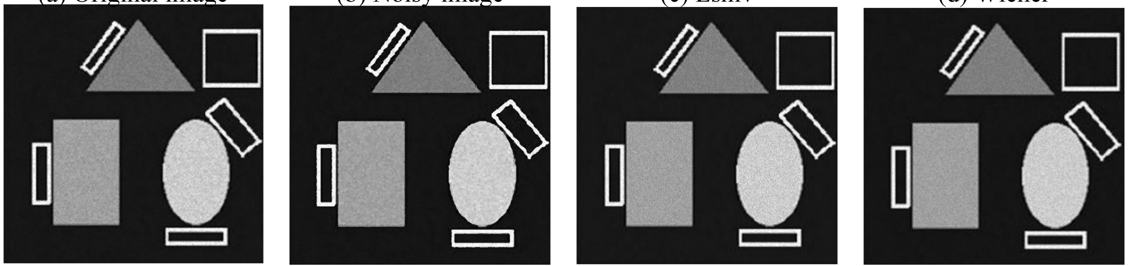

(e) Median (f) Kuwahara (g) Geometric (h) Lee

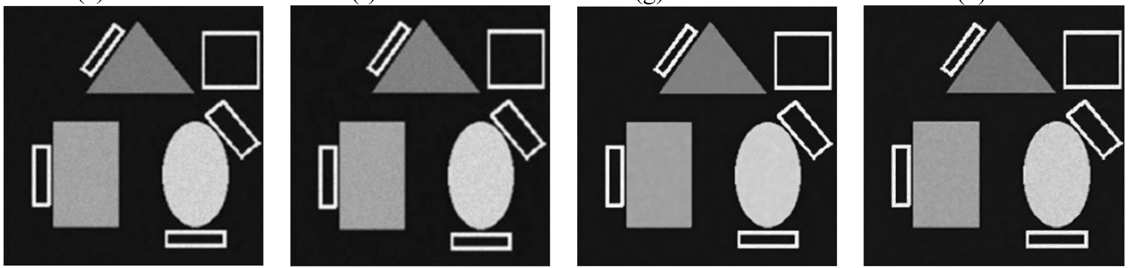

(i) Frost (j) Kuan (k) NLM (l) FNLM

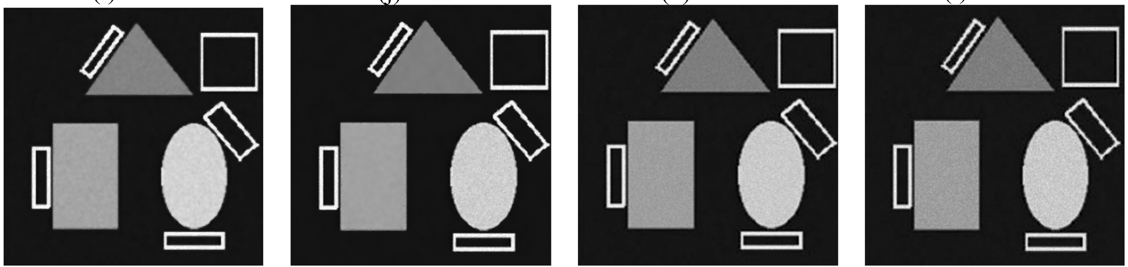

(m) PMAD (n) SRAD (o) TMAV (p) TMED

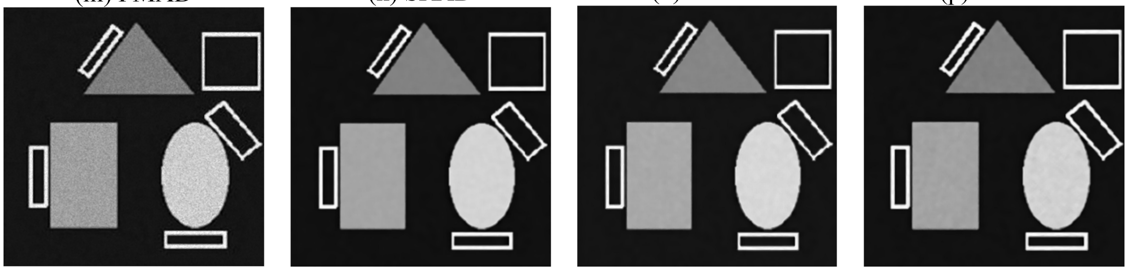

(q) ATMED (r) HFF1 (s) HFF2 (t) HFF3

Fig. 3.4: Visual quality comparison of denoised Synthetic image for noise level equal to 0.01 using different filters

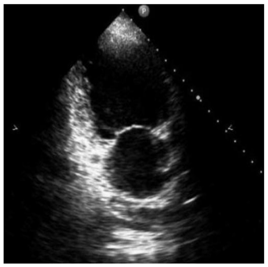
(a) Original image

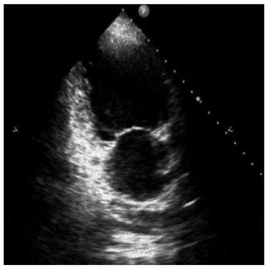
(b) Noisy image

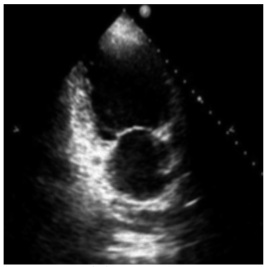
(c) Lsmv

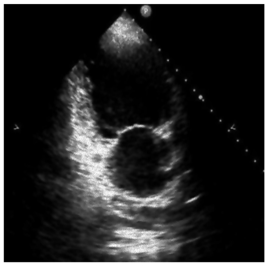
(d) Wiener

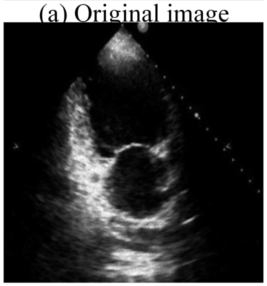
(e) Median

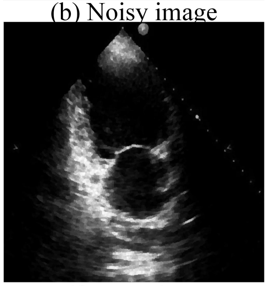
(f) Kuwahara

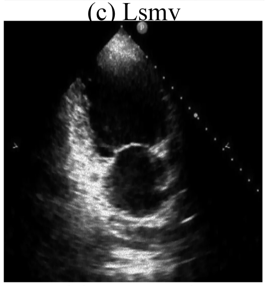
(g) Geometric

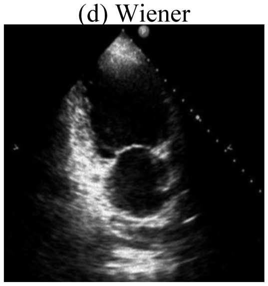
(h) Lee

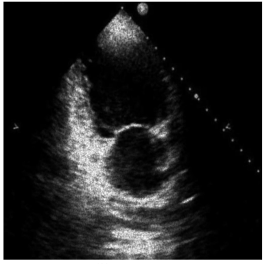
(i) Frost

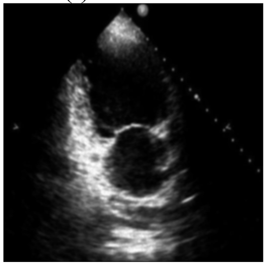
(j) Kuan

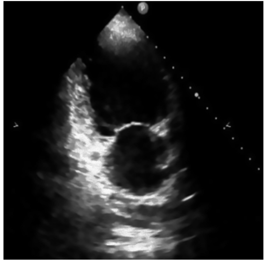
(k) NLM


(l) FNLM

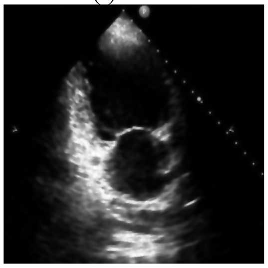
(m) PMAD

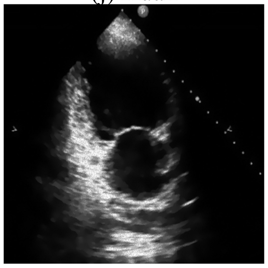
(n) SRAD


(o) TMAV

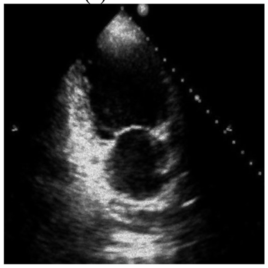
(p) TMED

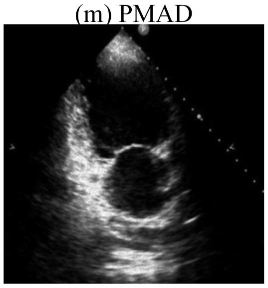
(q) ATMED


(r) HFF1

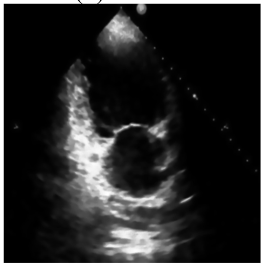
(s) HFF2

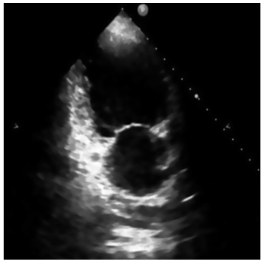
(t) HFF3

Fig. 3.5: Visual quality comparison of denoised A2C image for noise level equal to 0.01 using different filters

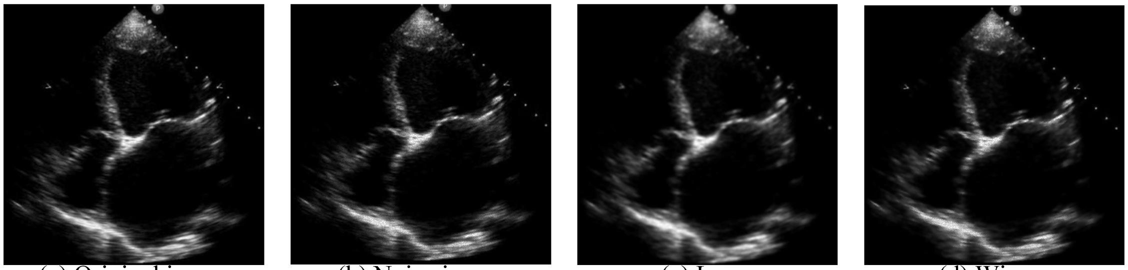

(a) Original image (b) Noisy image (c) Lsmv (d) Wiener

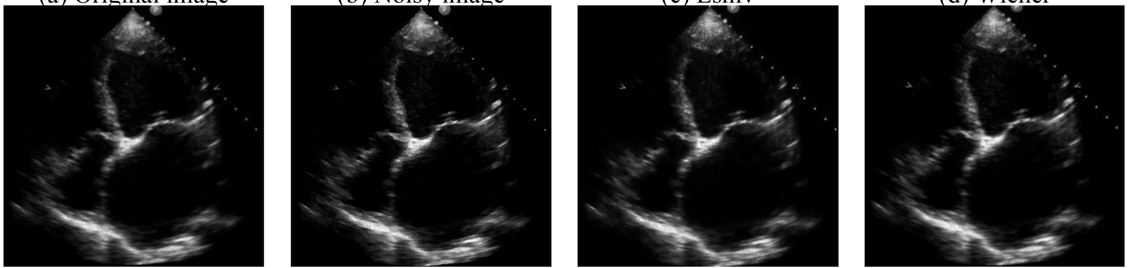

(e) Median (f) Kuwahara (g) Geometric (h) Lee

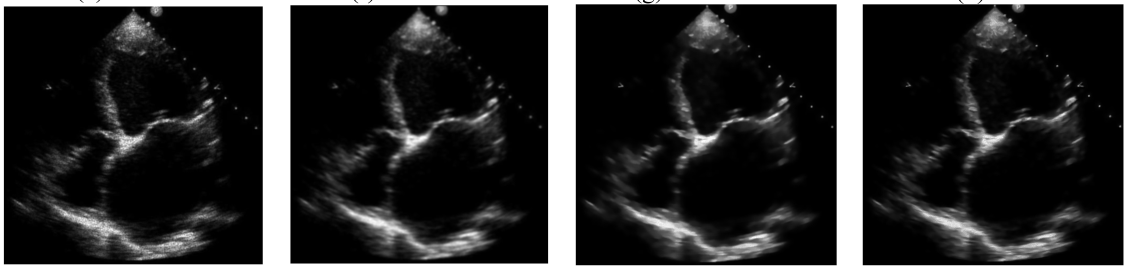

(i) Frost (j) Kuan (k) NLM (l) FNLM

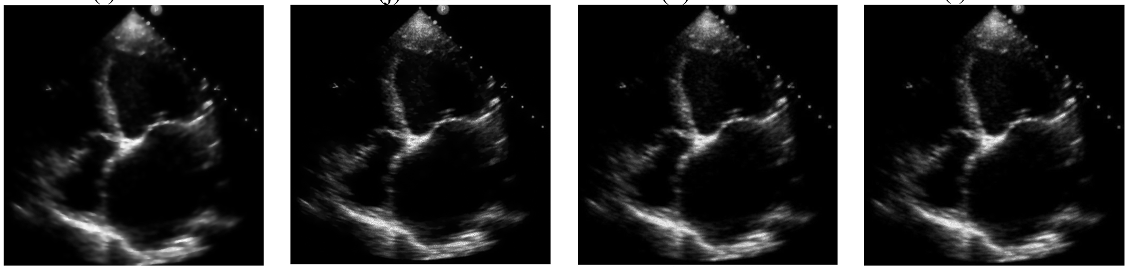

(m) PMAD (n) SRAD (o) TMAV (p) TMED

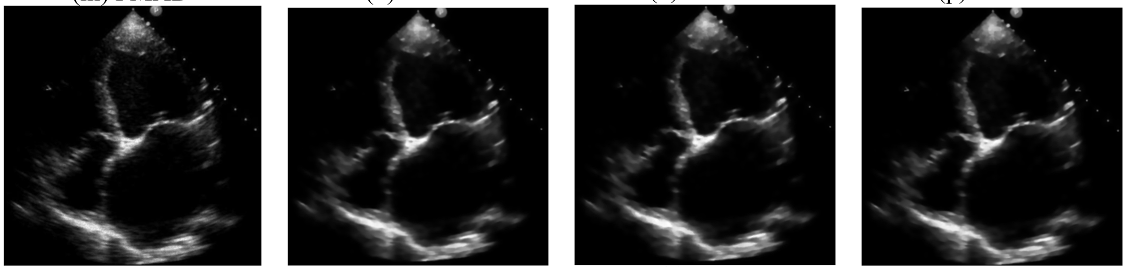

(q) ATMED (r) HFF1 (s) HFF2 (t) HFF3

Fig. 3.6: Visual quality comparison of denoised A4C image for noise level equal to 0.01 using different filters

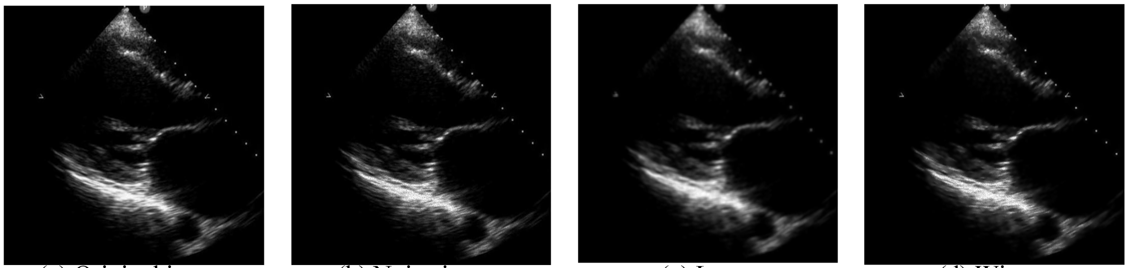

(a) Original image (b) Noisy image (c) Lsmv (d) Wiener

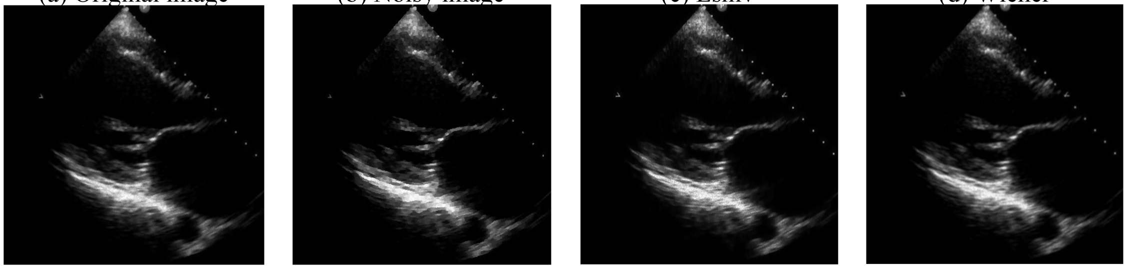

(e) Median (f) Kuwahara (g) Geometric (h) Lee

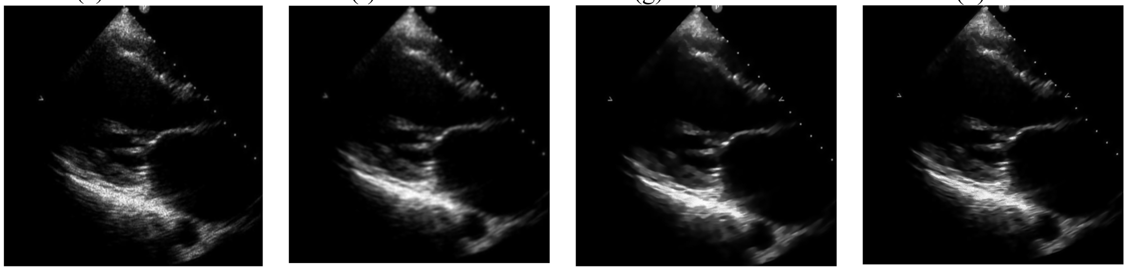

(i) Frost (j) Kuan (k) NLM (l) FNLM

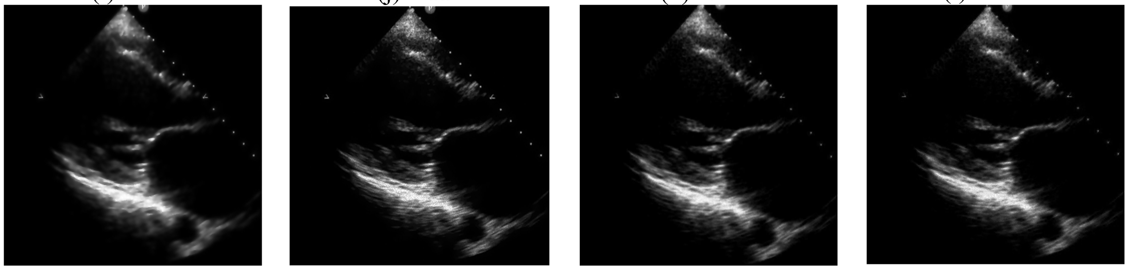

(m) PMAD (n) SRAD (o) TMAV (p) TMED

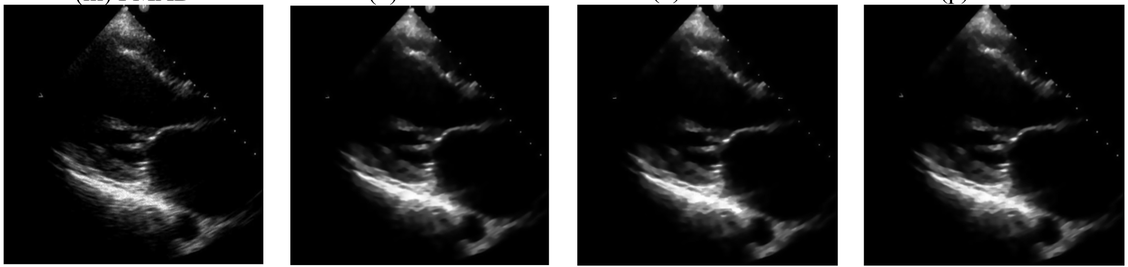

(q) ATMED (r) HFF1 (s) HFF2 (t) HFF3

Fig. 3.7: Visual quality comparison of denoised PLAX image for noise level equal to 0.01 using different filters

Table 3.2: Comparison of image quality metrics for test images with noise variance varying from 0.01 to 0.1 using TMED, TMAV, ATMED, and NLM filter

		TMED	TMAV	ATMED	NLM	TMED	TMAV	ATMED	NLM	TMED	TMAV	ATMED	NLM
Image	Noise	PSNR				SSIM				FoM			
Lena	0.01	32.25	35.36	35.80	36.63	0.7620	0.8828	0.8050	0.8908	0.8492	0.8797	0.7487	0.7944
	0.03	29.10	32.35	30.70	32.97	0.6070	0.7767	0.6444	0.7100	0.5095	0.7157	0.4638	0.7794
	0.05	26.68	29.96	28.60	29.02	0.5212	0.7033	0.5574	0.5522	0.4434	0.5636	0.4283	0.5961
	0.10	22.44	25.55	26.57	22.87	0.3935	0.5705	0.4392	0.3676	0.3749	0.4319	0.3807	0.4243
Synthetic	0.01	30.95	34.22	36.78	40.83	0.8829	0.9430	0.9038	0.9606	0.4339	0.4781	0.4356	0.6063
	0.03	28.86	32.02	32.82	34.31	0.8101	0.8917	0.8333	0.8596	0.4082	0.4368	0.4036	0.4409
	0.05	26.95	30.17	30.70	30.39	0.7705	0.8588	0.7945	0.8003	0.3771	0.4226	0.3630	0.3591
	0.10	23.51	26.55	27.61	25.56	0.6999	0.7960	0.7340	0.7504	0.3487	0.3887	0.3516	0.3325
		SSI				Beta				NCC			
Lena	0.01	0.9623	0.9576	0.9627	0.9523	0.1173	0.3326	0.3796	0.5356	0.9822	0.9859	0.9936	0.9958
	0.03	0.9058	0.8975	0.9124	0.9071	0.1089	0.2577	0.2293	0.1817	0.9566	0.9681	0.9865	0.9922
	0.05	0.8600	0.8496	0.8714	0.8832	0.0935	0.2178	0.1758	0.1073	0.9275	0.9475	0.9775	0.9894
	0.10	0.7869	0.7638	0.7980	0.8666	0.0719	0.1562	0.1226	0.0600	0.8516	0.8927	0.9552	0.9820
Synthetic	0.01	0.9860	0.9869	0.9878	0.9900	0.2103	0.4846	0.5280	0.7039	0.9492	0.9631	0.9825	0.9934
	0.03	0.9703	0.9716	0.9742	0.9783	0.1678	0.3729	0.3618	0.2871	0.9206	0.9422	0.9683	0.9869
	0.05	0.9539	0.9571	0.9624	0.9717	0.1471	0.3187	0.2863	0.1759	0.8845	0.9178	0.9533	0.9813
	0.10	0.9234	0.9271	0.9369	0.9634	0.1082	0.2358	0.2079	0.0938	0.8027	0.8582	0.9188	0.9640
		MSE				IQI				SNR			
Lena	0.01	75.61	37.00	42.06	27.60	0.5703	0.6937	0.6078	0.6264	26.62	29.74	29.21	31.05
	0.03	156.20	74.01	108.11	80.66	0.4590	0.5778	0.4851	0.4842	23.37	26.65	25.09	26.39
	0.05	273.05	128.30	175.51	200.26	0.3997	0.5162	0.4268	0.4001	20.82	24.18	22.96	22.44
	0.10	723.65	353.79	352.29	656.51	0.3087	0.4197	0.3481	0.2973	16.29	19.54	19.85	17.31
Synthetic	0.01	104.42	49.22	27.28	10.75	0.3808	0.4884	0.4219	0.3371	22.40	25.72	28.36	32.45
	0.03	168.98	81.70	67.88	48.22	0.3016	0.3972	0.3316	0.3166	20.19	23.43	24.35	25.91
	0.05	262.26	125.20	110.62	118.91	0.2671	0.3523	0.2932	0.3041	18.14	21.47	22.17	21.98
	0.10	579.14	287.56	225.40	361.11	0.2162	0.2859	0.2500	0.2731	14.37	17.61	18.95	17.14

increases which causes the loss of the image texture. It can be observed from the Fig. 4 (c)- 4 (g), that there is smoothing at the output of Lmsc filter. The geometric filter is known for edge preservation when employed for speckle noise reduction but retains noisy edges in the denoised image. The noise is effectively removed in Wiener filter and the edges are well preserved. The outcome of geometric filter preserves the texture as it has good edge preservation index beta (β) but contain small speckle noise. The outcome of Lee and Kuan filter incites visual artifacts as observed in Fig. 4 (h)-4 (j), while Frost filter brings about the

Table 3.3: Comparison of edge preserving parameters for ultrasound images in three views

	A2C	A4C	PLAX	A2C	A4C	PLAX	A2C	A4C	PLAX
Methods	PSNR (dB)			SSIM			FOM		
Lsmv	37.50	38.77	37.44	0.9342	0.9472	0.9475	0.8683	0.8729	0.8880
Wiener	41.17	41.72	41.98	0.9263	0.9399	0.9393	0.8323	0.8542	0.8880
Median	38.74	40.23	38.29	0.9416	0.9528	0.9554	0.8804	0.8981	0.9029
Kuwahara	36.43	37.59	37.53	0.9510	0.9586	0.9531	0.9488	0.9362	0.9332
Geometric	40.17	40.98	40.25	0.9729	0.9772	0.9796	0.9119	0.8663	0.9162
Lee	40.08	41.29	39.42	0.9619	0.9689	0.9633	0.9537	0.9606	0.9601
Frost	41.86	43.10	42.13	0.9543	0.9609	0.9638	0.9661	0.9709	0.9712
Kuan	37.78	39.08	37.84	0.9583	0.9648	0.9609	0.8748	0.8406	0.8618
PMAD	37.35	38.67	38.13	0.9288	0.9389	0.9382	0.7798	0.7152	0.7607
SRAD	36.47	39.36	39.41	0.9491	0.9608	0.9673	0.7711	0.9064	0.9148
NLM	39.68	40.76	40.58	0.9353	0.9430	0.9488	0.7035	0.7279	0.7081
FNLM	42.12	43.09	42.93	0.9637	0.9674	0.9709	0.8472	0.7922	0.8398
TMED	37.91	38.78	37.40	0.9666	0.9658	0.9724	0.9107	0.9136	0.9123
TMAV	40.81	41.77	40.05	0.9882	0.9898	0.9878	0.9363	0.9396	0.9388
ATMED	42.62	42.96	41.80	0.9913	0.9925	0.9911	0.9529	0.9639	0.9599
HFF1	39.49	40.62	39.68	0.9583	0.9626	0.9583	0.9674	0.9259	0.9595
HFF2	40.54	41.61	40.71	0.9786	0.9812	0.9776	0.9599	0.9217	0.9461
HFF3	42.65	43.88	43.11	0.9899	0.9916	0.9896	0.9720	0.9978	0.9813
	SSI			Beta			NCC		
Lsmv	0.9510	0.9586	0.9531	0.5107	0.4886	0.3565	0.9841	0.9730	0.9704
Wiener	0.9729	0.9772	0.9796	0.8686	0.9134	0.9134	0.9951	0.9934	0.9937
Median	0.9619	0.9689	0.9633	0.4398	0.4791	0.3858	0.9866	0.9752	0.9716
Kuwahara	0.9543	0.9609	0.9638	0.3214	0.3408	0.3408	0.9955	0.9874	0.9861
Geometric	0.9666	0.9658	0.9724	0.8280	0.8071	0.8551	0.9975	0.9970	0.9971
Lee	0.9882	0.9898	0.9878	0.7854	0.7829	0.7475	0.9938	0.9896	0.9879
Frost	0.9913	0.9925	0.9911	0.7869	0.7839	0.7560	0.9962	0.9933	0.9917
Kuan	0.9583	0.9648	0.9609	0.6081	0.5931	0.5496	0.9843	0.9734	0.9711
PMAD	0.9288	0.9389	0.9382	0.5011	0.4773	0.5043	0.9828	0.9704	0.9714
SRAD	0.9874	0.9948	0.9939	0.3292	0.3334	0.4792	0.9962	0.9990	0.9962
NLM	0.9353	0.9430	0.9488	0.7532	0.7394	0.7611	0.9891	0.9782	0.9798
FNLM	0.9637	0.9674	0.9709	0.7637	0.7448	0.7786	0.9837	0.9882	0.9889
TMED	0.9442	0.9572	0.9575	0.1781	0.1299	0.1225	0.9613	0.9502	0.9478
TMAV	0.9363	0.9499	0.9393	0.5457	0.5110	0.4602	0.9645	0.9536	0.9487
ATMED	0.9516	0.9628	0.9654	0.7422	0.7557	0.6959	0.9812	0.9650	0.9643
HFF1	0.9583	0.9626	0.9583	0.7231	0.7094	0.7407	0.9750	0.9596	0.9545
HFF2	0.9786	0.9812	0.9776	0.7276	0.7818	0.7592	0.9818	0.9704	0.9660
HFF3	0.9899	0.9916	0.9896	0.7696	0.7668	0.7602	0.9916	0.9854	0.9831

Table 3.4: Comparison of traditional parameters for ultrasound images in three views

	A2C	A4C	PLAX	A2C	A4C	PLAX	A2C	A4C	PLAX
Methods	MSE			SMPI			SNR (dB)		
Lsmv	22.07	16.35	22.38	3.0956	2.7293	3.6485	24.75	22.50	21.14
Wiener	4.74	3.30	3.13	3.1486	2.8358	3.7839	31.46	29.53	29.75
Median	16.56	11.67	18.40	3.3318	2.9591	3.8902	26.00	23.97	21.99
Kuwahara	28.23	21.41	21.89	3.5294	3.1612	4.0536	23.73	21.40	21.30
Geometric	4.75	3.91	3.70	3.5344	3.1532	4.0357	31.47	28.80	29.04
Lee	4.85	3.64	5.65	3.1074	2.7690	3.7129	31.36	29.08	27.17
Frost	3.22	2.40	3.80	3.1836	2.8425	3.7757	33.15	30.91	28.90
Kuan	20.70	15.20	20.41	3.1522	2.7605	3.6741	25.03	22.82	21.54
PMAD	22.81	16.72	19.07	3.0859	2.6992	3.6386	24.60	22.39	21.83
SRAD	27.92	14.24	14.19	3.2912	2.8592	3.8334	23.78	23.21	23.22
NLM	13.36	10.31	10.85	3.2407	2.8686	3.8082	26.94	24.52	24.30
FNLM	7.61	6.03	6.31	3.1923	2.8383	3.7795	29.40	26.88	26.69
TMED	27.85	21.29	26.61	3.6631	3.2226	4.1339	23.68	21.26	20.29
TMAV	34.61	26.88	33.33	3.5416	3.1331	4.0628	22.71	20.21	19.27
ATMED	21.32	15.93	19.15	3.2849	2.9191	3.8682	24.88	22.58	21.78
HFF1	20.08	16.28	22.57	3.6406	3.1823	4.0808	25.12	22.46	21.03
HFF2	10.30	8.18	12.26	3.7660	3.2685	4.1456	28.04	25.49	23.71
HFF3	4.28	3.12	5.17	3.3842	2.9752	3.9002	31.89	29.73	27.53
	Err3			Err4			LMSE		
Lsmv	7.68	6.87	8.55	11.31	10.34	13.41	0.7700	0.7890	0.8811
Wiener	3.06	2.60	2.63	3.84	3.30	3.39	0.2517	0.2497	0.1709
Median	7.47	6.60	8.84	11.95	10.82	14.78	0.8931	0.8416	0.9176
Kuwahara	8.63	7.75	8.27	12.08	10.99	12.24	6.1957	6.1100	3.9853
Geometric	3.07	2.84	2.88	3.80	3.56	3.67	0.3205	0.3536	0.2687
Lee	3.78	3.26	4.33	6.03	4.97	6.72	0.4275	0.4332	0.4981
Frost	3.08	2.63	3.54	4.94	4.02	5.48	0.3990	0.4030	0.4544
Kuan	7.87	7.67	9.16	12.18	13.97	16.55	0.6679	0.6797	0.7456
PMAD	6.96	6.16	6.74	9.00	8.16	8.93	0.7629	0.7924	0.7553
SRAD	7.70	6.18	6.37	9.89	8.45	8.82	5.1155	6.4074	2.9236
NLM	5.03	4.56	4.91	6.27	5.79	6.39	0.4538	0.4775	0.4483
FNLM	3.97	3.64	3.94	5.31	4.99	5.57	0.4187	0.4476	0.3949
TMED	8.11	7.36	8.89	11.49	10.58	13.43	1.7854	1.9269	1.8130
TMAV	9.18	8.44	10.10	12.98	12.24	15.33	0.7183	0.7664	0.8174
ATMED	7.00	6.21	7.32	10.02	8.88	10.90	0.4496	0.4301	0.5139
HFF1	7.47	6.92	8.66	10.96	10.17	13.29	0.6647	0.6768	0.7418
HFF2	5.49	4.98	6.60	8.42	7.54	10.50	0.7442	0.7788	0.8713
HFF3	4.02	3.41	4.70	7.05	5.73	7.93	0.5952	0.5979	0.6253

loss of texture.

The Lee and Frost filters have similar values for SSIM metric. The Frost and Kuan filter likewise protect the edge information. Average edge pixel distortion because of filtering is minimal in SAR filters as observed by the high FoM. In general, the SAR filters are computationally effective and have some speckle reduction but the output frequently seems obscured. The nonlocal mean filters (NLM, FNLM) have strong speckle reduction that can be observed from the Figs. 4 (k) and 4 (l) while having high computational complexity. From the image quality metrics, it is observed that the value of FoM and SSIM are high for NLM filters which show its effectiveness for preserving edges.

Figs. 4 (m) and 4 (n) show the output of AD based despeckling filters (PMAD, SRAD). These filters remove speckle noise but have smoothing at edges. Furthermore, the fuzzy filters such as TMED, TMAV, ATMED filter hold noise in the processed image. In view of the outcomes, it is observed that the texture is partially preserved using fuzzy ATMED filter.

Tables 3.2 and 3.3 compare the performance of the proposed hybrid filter (HFF) in terms of edge-preserving parameters and traditional parameters, respectively. The outcomes are being tabulated for each kind of filter to compare the performance of each filter. Strong speckle suppression is observed in proposed hybrid filter HFF3, followed by FNLM in terms of PSNR. The PSNR of the HFF3 filter (42.65 dB) has been improved compared to HF (42.62 dB) and NLM filter (39.68 dB). MSE is less for HFF when compared to many of the filters. Also the traditional parameters (PSNR, MSE, SNR, and NCC) for the proposed hybrid filter HFF3 are superior in comparison to HF filter, AD filters, and NLM filters. Results obtained using proposed HF filters are compared with other filters in terms of image quality metrics shown in Fig. 3.2. The performances of the HFF3 filters are superior in terms of SSI. SMPI values are superior compared to SAR filters. FoM is greater than one indicating better denoising performance. The fuzzy filters perform well in terms of IQI, FoM, and SSI with fractionally higher SMPI but have a poor beta metric.

The performances of the wiener, Frost, FNLM, and ATMED filters are similar in terms of PSNR. The beta value of the proposed filters increased when compared to hybrid filters and NLM filter. The correlation coefficient value is also improved in the HFF filters. All the edge preserving parameters (PSNR, SSIM, FoM, SSI, Beta (β) and NCC (ρ)) are having improved values in contrast with fuzzy filters and NLM filter. Further, denoising quality of HFF filter is being compared with fifteen despeckling filters and visual results are depicted in Fig. 3.3 - 3.7 and it is observed that the HFF3 filters outperformed all thus.

3.7 Summary

The despeckling applications of fifteen types of despeckling filters along with three proposed hybrid filters have been analyzed in this work in terms of blind and full-reference parameters. The traditional parameters often fail to reflect the true performance of the filters in the absence of a noise-free reference image. The parameters such as speckle suppression index, and beta metric are used to study the speckle suppression and edge preservation capability of each filter. The image quality and structural preservation are analyzed using SMPI, FoM, IQI, and SSI. Various types of benchmark filters are available and it would be very difficult to choose the best clinically acceptable filter. It is also necessary to remove speckle noise but with the edges preserved. The major contributions of this work are (i) it helps in selecting the best filters suitable for clinical TTE images among all types of filters and their constituents, (ii) it studies and evaluates the performance in terms of blind and full-reference based parameters, and evaluations of filters based image quality metrics are validated by practicing clinicians. Based on the quantitative evaluation and clinical validation, it is concluded that the proposed hybrid filter (HFF3) performed best compared to other in terms of edge preservation and denoising of speckle noise.

CHAPTER 4

SPATIAL DOMAIN TEXTURE BASED ANALYSIS OF MITRAL REGURGITATION

This chapter analyzes the performance of spatial domain texture extraction techniques for the severity analysis of mitral regurgitation (MR). This chapter also investigates the aspects of statistical features i.e. color spaces followed by the performance evaluation of these techniques by different classifiers.

4.1 Spatial Domain Texture Features

Texture can be characterized as a component of the spatial variation in pixel intensities. The texture may be constructed as including color, motion, flicker rate or even stereo disparity. Most researchers have confined the definition to mean a spatial arrangement of neighborhood intensity attributes which are correlated within the areas of the visual scene and corresponding to surface regions. Texture features play a critical role in the classification of image database. The three main methodologies utilized in image processing to portray the texture of a region are statistical, structural, and spectral. Statistical domain approaches manage the portrayal of textures as smooth, coarse, and grainy. Similarly, structural techniques manage the arrangement of image primitive, such as the description of the texture based on regularly spaced parallel lines. Spectral techniques depend on properties of the Fourier spectrum and utilized principally to distinguish global periodicity in an image by identifying high-energy, narrow peaks in the spectrum. The texture gives exceptionally noteworthy information for the diagnosis of the diseases when used as an input to a CAD system.

Table 4.1 summarizes various CAD systems proposed by several researchers for the characterization and classification of different diseases. These CAD systems have shown their ability with reasonable accuracy based on the texture features, extracted from the images of various medical image data sets in the combination with different classifiers.

Table 4.1: Existing CAD studies using statistical texture feature

Authors	Modality, Classification technique	Diagnosis	Features used
Christodoulou, 2003 [19]	Ultrasound, KNN	Carotid plaques	FOS, SGLDM, GLDS, NGTDM, SFM, TEM, FDTA, FPS
Chen, 2005 [20]	Ultrasound, K-mean classification	Breast cancer	Fractal feature
Chang, 2010 [209]	Ultrasound, ANN, BP-NN, linear classifier	Breast cancer	Texture feature, Morphological feature, Model based feature, Descriptor features
Chuan, 2010 [122]	Ultrasound, SVM	Thyroid nodules	GLCM, SFM, GLRLM, Laws feature, NGLDM, WF, FF
Nikolaos, 2011 [172]	Ultrasound, SVM, PNN	Carotid atherosclerosis	DWT, GT
Mandeep, 2013 [123]	Ultrasound, LDA	Liver images	SGLCM, GLDS, FOS, FPS, SFM, LAWs feature, Fractal feature
Sudarshan, 2013 [124]	Ultrasound, SVM, KNN		FOS, GLCM, LTE, LBP
Virmani, 2013 [173]	Ultrasound, SVM	Liver images	GLCM, GLRLM, FPS, LAWs texture feature
Gao, 2014 [23]	Ultrasound, NN	Liver images	GLGCM, GLCM

KNN: K-nearest neighbors, ANN: Artificial neural network BP-NN: Back-Propagation Neural Networks, PNN: Probabilistic neural network, FOS: First order statistics, SGLDM: Spatial gray level difference matrix, GLDS: Gray-level difference statistics, NGTDM: Neighborhood gray tone difference matrix, SFM: Statistical feature matrix, LTE: Law's texture energy, FDTA: Fractal dimension texture analysis, FPS: Fourier power spectrum, GLCM: Gray level co-occurrence matrix, GLRLM: Gray level run length matrix, NGLDM: Neighboring gray level dependence matrix, DWT: Discrete wavelet transform, GT: Gabor transform, SGLCM: Spatial gray-level co-occurrence matrices, LBP: Local binary pattern, GLGCM: Gray level-gradient co-occurrence matrix.

4.2 Aspects of Spatial Domain Features (Image Color Models)

A color model or space is a method by which we are able to specify, produce and visualize color. A color image provides more information about the image as compared to a single intensity image. A color texture may be defined as the distribution of colors over a surface, while grayscale textures consider only luminance [210]. The *RGB* color space is mostly accepted in image processing areas but most of the CAD systems have been developed for grayscale images. It is an important aspect to select the optimum color space out of the existing color spaces for a specific application. This chapter compares four color spaces i.e. *RGB*, *L*A*B**, *YCbCr* and *CMY* in terms of their effectiveness in color texture analysis.

4.2.1 RGB (Red Green Blue)

The *RGB* color space is the most accepted format by the image processing community. Red, green and blue are the three primary colors are added together to form the desired color. In this space, each color is represented as a triplet of red, green and blue (R, G, B) outputs from a color camera. This color scheme is device-dependent. *RGB* space is transformed into various other color spaces to improve the visibility of the image.

4.2.2 YCbCr (Luminance - Chrominance)

This is a digital color the system used for coding of TV pictures [211]. The *YCbCr* color space can be achieved by transforming RGB values using the following equation:

$$\begin{bmatrix} Y \\ Cb \\ Cr \end{bmatrix} = \begin{bmatrix} 16 \\ 128 \\ 128 \end{bmatrix} + \begin{bmatrix} 65.481 & 128.553 & 24.966 \\ -37.797 & -74.203 & 112 \\ 112 & -93.786 & -18.214 \end{bmatrix} \begin{bmatrix} R \\ G \\ B \end{bmatrix} \tag{4.1}$$

4.2.3 CMY (Cyan Magenta Yellow)

This is a subtractive color space and mainly used in color printing. The conversions are generally done through color management systems where *CMY* components are just the compliments of the *RGB* components [212].

$$\left.\begin{aligned} Cyan &= 255 - red \\ Magenta &= 255 - Green \\ Yellow &= 255 - Blue \end{aligned}\right\} \tag{4.2}$$

4.2.4 L*A*B*

The *L*A*B** color space is very close to human perception of color because it has a uniform distribution of colors. It is a non-linear color model and the conversions are reversible. The luminance L* scales from 0 to 100, while parameters A* (from green to red) and B* (from blue to yellow) in the range from -120 to 120 are the two chromatic components. It is derived from *RGB* as follows [213]:

$$\begin{bmatrix} X \\ Y \\ Z \end{bmatrix} = \begin{bmatrix} 0.412453 & 0.357580 & 0.180423 \\ 0.212671 & 0.715160 & 0.072169 \\ 0.019334 & 0.119193 & 0.950228 \end{bmatrix} \begin{bmatrix} R \\ G \\ B \end{bmatrix} \tag{4.3}$$

$$\left.\begin{aligned} L^{*} &= 116 \times f\left(Y/Y_n\right) - 16 \\ A^{*} &= 500 \times \left(f\left(X/X_n\right) - f\left(Y/Y_n\right)\right) \\ B^{*} &= 200 \times \left(f\left(Y/Y_n\right) - f\left(Z/Z_n\right)\right) \end{aligned}\right\} \tag{4.4}$$

where, $f(q)$ in Eq. 4.4

$$f(q) = \begin{cases} q^{0.333} & if\ q > 0.008856 \\ 7.787\,q\ +\ 0.137931 & otherwise \end{cases}$$

The X, Y, and Z are the CIE tristimulus values and X_n, Y_n, and Z_n are the tristimulus values for the illuminant.

4.2.5 Gray Scale

A gray scale image gives the information about the intensity of the pixels. A color image is converted into gray scale by the formula:

$$Y = 0.212671\,R + 0.715160\,G + 0.072169\,B \tag{4.5}$$

4.3 Methodology for Spatial Domain Texture Feature based MR Classification

The procedural steps involved in present work used for the severity classification of echocardiographic images of MR is represented in the form of block schematic and is shown in Fig. 4.1. The steps of the complete classification process explained as follows:

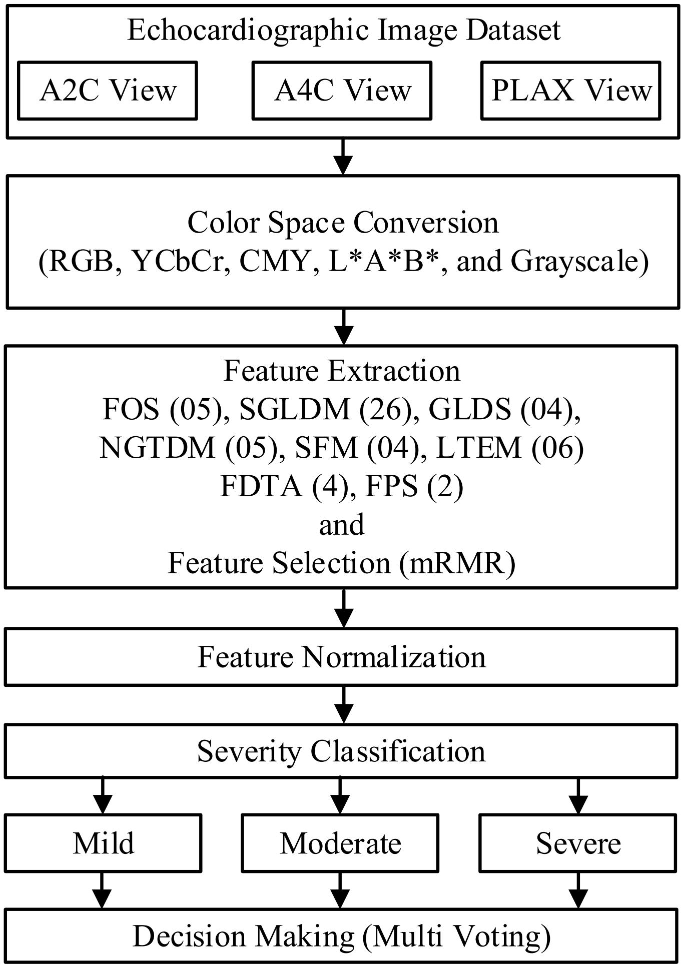

Fig. 4.1: Schematic for classification of MR using spatial texture feature extraction techniques.

Step 1: To compare the color spaces for the texture analysis of MR images. The color images are converted to other color space as explained in Section 4.2. Further, a subjective rectangular window is then chosen which incorporates the regurgitant jet area of each image for picking the region of interest.

Step 2: Here, spatial domain six texture descriptors namely first-order statistics (FOS), spatial gray level difference matrix (SGLDM), gray level difference statistics (GLDS), neighborhood gray tone difference matrix (NGTDM), statistical feature matrix (SFM), and Laws textures energy measure (LTEM) have been used to extract the texture feature.

Step 3: The extracted features contain the different range of numeral values which are normalized in the range of 0 to 1 before applying it to classifier utilizing the Eq. 4.6.

$$n(x_i) = \frac{(x_i - m_i)}{\sigma_i} \tag{4.6}$$

where, x is an original value $n(x_i)$ is the normalized value, m_i and σ_i represent the mean and standard deviation of the feature *i*.

Step 4: In step 4, supervised classifiers i.e. support vector machine (SVM) with three kernel functions i.e. linear, polynomial and radial basis function (RBF) and random forest (RF) has been used with 10-fold and leave-one-out cross-validation scheme. The characterization performance of the approach has been assessed by its classification accuracy, sensitivity, and specificity. Based on the classification accuracy the best texture features can be identified.

4.4 Texture Feature Extraction

An image texture gives the information about the intensities of an image in the spatial domain. It is an important characteristic for image analysis and plays a significant role in research areas such as image processing, remote sensing, and medical imaging, etc. The extracted texture feature of the images is used for texture discrimination, object shape determination, and the texture classification. In the following section texture feature descriptors are briefly explained which are used in present experiments:

4.4.1 First Order Statistics (FOS)

The basic information of images can be explored through statistical analysis of single pixels. The histograms represent the intensity distribution of pixel images [214]. For a given image statistical analysis of the distribution of pixel intensities are known as FOS [116]. In FOS, the main features that are taken into consideration are mean, median, standard deviation (SD), skewness and kurtosis. Mean of a gray-scale image is a measure of the average intensity of pixels, while SD is a measure of contrast. Skewness is a measure of the symmetry (it deal with the degree of histogram asymmetry around the mean) and kurtosis is the descriptor of the shape of the probability distribution. The formula for each of the FOS feature descriptors are given as:

$$Mean = \bar{x} = \frac{1}{MN}\sum_{i=1}^{M}\sum_{j=1}^{N} I\left(i,j\right) \tag{4.7}$$

$$Standard\ Deviation\ =\ \sigma\ =\ \sqrt{\frac{1}{MN-1}\sum_{i=1}^{M}\sum_{j=1}^{N}\left(I\left(i,j\right)-\bar{x}\right)^{2}} \tag{4.8}$$

$$Skewness\ =\ \frac{1}{MN}\sum_{i=1}^{M}\sum_{j=1}^{N}\left(\frac{I\left(i,j\right)-\bar{x}}{\sigma}\right)^{3} \tag{4.9}$$

$$Kurtosis\ =\ \frac{1}{MN}\sum_{i=1}^{M}\sum_{j=1}^{N}\left(\frac{I\left(i,j\right)-\bar{x}}{\sigma}\right)^{4} \tag{4.10}$$

4.4.2 Spatial Gray Level Dependence Matrices (SGLDM)

The SGLDM [117] is a statistical method in which co-occurrence matrices reflect the spatial distribution of gray levels in the ROI. SGLDM is computed by using the second-order joint conditional probability density functions (pdf) that consider two pixels (*k, l*) and (*m, n*) with the relative distance *d* and their relative orientation θ. A total 13 texture measures such as angular second moment, contrast, entropy, variance, correlation, inverse difference moment, sum variance, sum average, sum entropy, difference variance, difference entropy and information measures of correlation were computed. In this work, *d* = 1 and angles $\theta = 0°$, 45° , 90° and 135° were used for the computation of texture measures. The mean and standard deviation for the rows and columns of the matrix are expressed as:

$$\mu_x = \sum_{i=1}^{N_g}\sum_{j=1}^{N_g} ip\left(i,j\right) \tag{4.11}$$

$$\mu_y = \sum_{i=1}^{N_g}\sum_{j=1}^{N_g} jp\left(i,j\right) \tag{4.12}$$

$$\sigma_x = \sum_{i=1}^{N_g}\sum_{j=1}^{N_g} \left(i-\mu_x\right)^2 p\left(i,j\right) \tag{4.13}$$

$$\sigma_y = \sum_{i=1}^{N_g}\sum_{j=1}^{N_g} \left(j-\mu_y\right)^2 p\left(i,j\right) \tag{4.14}$$

where μ_x and μ_y are the means of p_x and p_y respectively; σ_x and σ_y are the standard deviation of p_x and p_y respectively; and N_g is the number of gray levels.

Probabilities of p_{x+y} and p_{x-y} that are related to specified intensity sums or differences, are defined as follows:

$$p_{x+y}\left(k\right) = \sum_{i=1}^{N_g} \sum_{j=1, i+j=k}^{N_g} p\left(i,j\right), k = 2,3,.....2N_g \tag{4.15}$$

$$p_{x-y}\left(k\right) = \sum_{i=1}^{N_g} \sum_{j=1, |i-j|=k}^{N_g} p\left(i,j\right), k = 0,1,2,.....\left(N_g-1\right) \tag{4.16}$$

Following features used in the present work are defined as follows:

$$Angular\ Second\ Moment = \sum_{i=1}^{N_g} \sum_{j=1}^{N_g} \left\{p\left(i,j\right)\right\}^2 \tag{4.17}$$

$$Contrast = \sum_{n=0}^{N_g-1} n^2 \left\{ \sum_{n=1}^{N_g} \sum_{j=1, |i-j|=n}^{N_g} p\left(i,j\right) \right\} \tag{4.18}$$

$$Entropy = -\sum_{i=0}^{N_g-1} \sum_{j=0}^{N_g-1} p\left(i,j\right) log\left(p\left(i,j\right)\right) \tag{4.19}$$

$$Variance = \sum_{i=1}^{N_g} \sum_{j=1}^{N_g} (i-m)^2 p\left(i,j\right) \tag{4.20}$$

$$Correlation = \sum_{i=0}^{N_g-1} \sum_{j=0}^{N_g-1} \frac{\left(i-\mu_x\right)\left(j-\mu_y\right)}{\sigma_x \sigma_y} p\left(i,j\right) \tag{4.21}$$

$$Inverse\ Difference\ Moment = \sum_{i=0}^{N_g-1} \sum_{j=0}^{N_g-1} \frac{1}{1+\left(i-j\right)^2} p\left(i,j\right) \tag{4.22}$$

$$Sum\ of\ Squares\ /\ Variance = \sum_{i=1}^{N_g} \sum_{j=1}^{N_g} \left(i-\mu\right)^2\ p\left(i,j\right) \tag{4.23}$$

$$Sum\ Average = \sum_{i=2}^{2N_g} i\ p_{x+y}\left(i\right) \tag{4.24}$$

$$Sum\ Entropy = -\sum_{i=2}^{2N_g} p_{x+y}\left(i\right)\ log\left\{p_{x+y}\left(i\right)\right\} \tag{4.25}$$

$$Difference\,Variance = Variance\,of\,p_{x-y} \tag{4.26}$$

$$Difference\,Entropy = -\sum_{i=0}^{N_g-1} p_{x-y}\left(i\right)\ log\left\{p_{x-y}\left(i\right)\right\} \tag{4.27}$$

Information Measure of Correlation (IMC)

$$IMC1 = \frac{HXY - HXY1}{max\left\{HX, HY\right\}} \tag{4.28}$$

$$IMC2 = \left(1 - exp\left[-2.0\left(HXY2 - HXY\right)\right]\right)^{\frac{1}{2}} \tag{4.29}$$

where,

$$HXY = -\sum_{i}\sum_{j} p\left(i,j\right)\ log\left(p\left(i,j\right)\right) \tag{4.30}$$

$$HXY1 = -\sum_{i}\sum_{j} p\left(i,j\right)\ log\left\{p_x\left(i\right)p_y\left(j\right)\right\} \tag{4.31}$$

$$HXY2 = -\sum_{i}\sum_{j} p_x\left(i\right)p_y\left(j\right)\ log\left\{p_x\left(i\right)p_y\left(j\right)\right\} \tag{4.32}$$

4.4.3 Gray Level Difference Statistics (GLDS)

The GLDS approach [118] is based on the assumption that useful texture information can be extracted using first order statistics of an image. The algorithm is based on the estimation of the probability density p_δ of image pixel pairs at a given distance δ = $(\triangle x,\ \triangle y)$, having a certain absolute gray level difference value. For any given displacement δ, let $f_\delta(x, y) = |f(x, y) - f(x + \delta_x, y + \delta_y)|$. Let p_δ be the probability density of $f\delta(x, y)$. If there are m gray levels, this has the form of an m-dimensional vector whose i^{th} component is the probability that $f\delta(x, y)$ will have value (i). Features were estimated for the following distances: δ = (0, 1), (1, 1), (1, 0), (1, -1). Some of the features that were computed are: 1) Mean, 2) Entropy, 3) Contrast, and 4) Energy.

4.4.4 Neighborhood Gray Tone Difference Matrix (NGTDM)

The textural features, NGTDM introduced by Amadasun and King [119] provide the visual properties of texture. In this work, a neighborhood size of 3 × 3, has been used for the extraction of the feature. An NGTDM is a column vector containing *G* elements. Its entires are computed which is based on measuring the difference between the intensity level of a pixel and the average intensity computed over a square, sliding window centered at the pixel. Suppose the image intensity level $f(x, y)$ at location (x, y) is $i, i = 0, 1, ...G-1$. The average intensity over a window centered at (x, y) is

$$\bar{f}_i = \bar{f}(x, y) = \frac{1}{W-1} \sum_{m=-K}^{K} \sum_{n=-K}^{K} f(x+m, y+n) \tag{4.33}$$

where K specifies the window size and $W = (2K+1)^2$. The i^{th} entry of the gray-tone difference matrix is

$$s_i = \sum_{x=0}^{M-1} \sum_{y=0}^{N-1} \left| i - \bar{f}_i \right| \tag{4.34}$$

for all pixels having the intensity level i. Otherwise, $s_i = 0$. Here, contrast, coarseness, busyness, complexity, and strength were calculated as:

$$Coarseness = \left(\epsilon + \sum_{i=0}^{G-1} p_i s_i \right)^{-1} \tag{4.35}$$

where ϵ is a small number to prevent the coarseness coefficient becoming infinite and p_i is the estimated probability of the occurrence of the intensity level i.

$$p_i = N_i / n \tag{4.36}$$

with N_i denoting the number of pixels that have the level i, and $n = (N-K)(M-K)$.

$$Contrast = \left[\frac{1}{N_t(N_t-1)} \sum_{i=0}^{G-1} \sum_{j=0}^{G-1} p_i \, p_j (i-j)^2 \right] \left[\frac{1}{n} \sum_{i=0}^{G} s(i) \right] \tag{4.37}$$

$$Buyness = \frac{\sum_{i=0}^{G} p_i s(i)}{\sum_{i=0}^{G-1} \sum_{j=0}^{G-1} |ip_i - jp_j|}, p_i \neq 0, p_j \neq 0 \tag{4.38}$$

$$Complexity = \sum_{i=0}^{G-1} \sum_{j=0}^{G-1} \frac{|i-j|}{n(p_i+p_j)} \left[p_i s(i) + p_j s(j) \right], p_i \neq 0, p_j \neq 0 \tag{4.39}$$

$$Strength = \frac{\sum_{i=0}^{G-1} \sum_{j=0}^{G-1} (p_i+p_j)(i-j)^2}{\epsilon + \sum_{i=0}^{G-1} s_i} \tag{4.40}$$

4.4.5 Statistical Feature Matrix (SFM)

In SFM, the statistical features were used for the analysis where properties of pixel pairs were measured at several distances within an image [120]. Based on the SFM, the texture features namely contrast, coarseness, roughness and periodicity were computed. For the maximum inter-sample spacing distance, the numeric value of constants L_r, L_c were set to 4.

4.4.6 Laws Textures Energy Measure (Laws TEM)

Laws developed a technique based on texture-energy that measure the amount of variation within a fixed size window. The vectors of length seven ($l = 7$) were used for the extraction of the laws TEM [121]. In this work, local averaging L = (1, 6, 15, 20, 15, 6, 1), edge detector E = (-1, -4, -5, 0, 5, 4, 1) and spot detector S = (-1, -2, 1, 4, 1, -2, -1) were used. The vectors are convoluted with each other or themselves. The features calculated from Laws texture energy measures are: 1) LL-texture energy from LL kernel; 2) EE-texture energy from EE kernel; 3) SS-texture energy from SS kernel; 4) LE-average texture energy from LE and EL kernels; 5) ES-average texture energy from ES and SE kernels, and 6) LS-average texture energy from LS and SL kernels.

4.4.7 Fractal Dimension Texture Analysis (FDTA)

The fractional Brownian motion model was introduced by Mandelbrot [215] in order to describe the roughness of natural surfaces. The Hurst coefficient H(k) was computed for image resolutions k = 1, 2, 3, 4. A large value of H is considered as a smooth surface, whereas a small value of H indicates rough surface.

4.4.8 Fourier Power Spectrum (FPS)

The radial sum and the angular sum of the discrete Fourier transform [118] were computed in order to describe the texture.

4.5 Feature Selection

Feature selection is essential in pattern recognition applications in order to improve the accuracy and efficiency of classification [216]. The aim of feature selection is to find the optimal subset consisting of m features chosen from the total n features. The feature selection technique facilitates in reducing the effect of the curse of dimensionality, giving a better insight of data, and improving the performance of classifier by using a subset of features as input [159, 217]. These techniques are categorized into the filter, wrapper and embedded methods in the context of classification [218]. Here, minimum redundancy maximum relevance (mRMR) technique has been used which reduces the number of features by ranking and then selecting the top-ranked features by wrapper based approaches [219].

4.6 Classification

The objective of classification is to develop a computationally efficient way of learning good separating hyperplanes in a high dimensional feature space. In this work the SVM with three kernel functions namely linear, polynomial, RBF [220, 221] and random forest (RF) classifier [222] have been used for the classification of the severity of MR. The feature sets described in Section 4.4 has been used as input to a classifier.

4.6.1 Support Vector Machine (SVM)

The SVM is an efficient and supervised classifier which is widely applied to several pattern recognition problems in signal and image processing due to their precise accuracy, the ability to deal with high-dimensional and large datasets [173, 223–225]. Initially it was proposed as binary classifier [220, 226]. Linear classifier works directly on the given data vector and is considered to be efficient in terms of faster training and testing procedure [227,228]. In many applications, a nonlinear classifier provides better accuracy, whereas linear classifier has the advantage of having simple training algorithms [229]. The binary class SVM has extended for multiclass classification using approaches such as, "one against one", "one against all", and "directed acyclic graph" [230]. Further, a multiclass SVM classifier is proposed by Crammer and Singer [231] by solving the single optimization problem.

In linear classifier, the training dataset consist of a set of *l* samples $\{x_i,\, y_i\}_{i=1}^{l}\ \ where\ x_i \in R^n,\, y_i \in \{-1,\, 1\}$. Given a training set of instance-label pairs the SVM requires the solution of the following optimization problem:

$$\min_{w,\,b,\,\xi}\ \frac{1}{2}w^T w \,+\, C\sum_{i=1}^{l}\xi_i, \tag{4.41}$$

subject to $y_i(w^T x_i \,+\, b)\ \geq\ 1\,-\,\xi_i,\xi_i\geq 0$. where ξ is a loss function and *C* (non-negative) is a penalty parameter (cost factor). A linear classifier is based on a linear discriminant function of the form the discriminant function *f(x)* assigns a "score" for the input x, and is used to decide how to classify it. The vector w is known as the weight vector, and the scalar *b* is called the bias. However, for the complex dataset, researchers introduced nonlinear function in equation 4.41.

$$\min_{w,\,b,\,\xi} \frac{1}{2} w^T w \,+\, C \sum_{i\,=\,1}^{l} \xi_i \tag{4.42}$$

subject to $y_i(w^T \phi(x_i) \;\geq\; 1 -\; \xi_i$,$\xi_i$≥0. The training vectors x_i are mapped into a higher

Table 4.2: Kernel functions

Kernel	Function
Linear	$K(x_i, x_j) \,=\, x_i^T x_j$
Polynomial	$K(x_i, x_j) \,=\, (\gamma x_i^T x_j \,+\, r)^d,\, \gamma \,>\, 0$
Radial basis function (RBF)	$K(x_i, x_j) \,=\, \exp(-\gamma \left\Vert x_i \,-\, x_j \right\Vert^2 \,\gamma \,>\, 0$

where γ, r and d are kernel parameters

dimensional space by using the kernel function (ϕ). The SVM finds a linear separating hyper plane with the maximum margin in this higher dimensional space. $(x_i, x_j) \;=\; \phi(x_i)^T \phi(x_j)$ is called the kernel function [221]. In this experimental work three kernels have been used which are listed in Table 4.2. For median-sized problems, the grid search approach has been used to find the best value of regularization parameter (penalty parameter *C* and kernel parameter γ [221]. The optimum value of *C* and γ has been obtained by using grid search method in the range (2^{-4} , 2^{3}. . . .2^{15}), and (2^{-12} , 2^{-11}. . . .2^{4}) respectively, using 10-fold cross validation approach for training data.

4.6.2 Random Forest (RF)

The RF classifier [222] consists of many individual classification trees, where each tree is a classifier by itself that is given a certain weight for its classification output. The classification outputs from all trees is used to determine the overall classification output which is done by choosing the mode (the output with most votes) of all trees classification output. This classifier has been used for various medical image classification problems [232, 233]. To generate the prediction model in RF classifier, the number of trees (*nTree*) and a number of arbitrarily chosen features (*mTry*) has to optimize. Typically, 500-2,000 trees are developed and the outcomes are accumulated by averaging [234]. In this work, the *nTree* values have been varied in the range of 100 to 1000 and it was found that expansion of a number of trees beyond 450-500 was not having a significant change in the classification accuracy for our dataset [234]. The *nTree* = 500 [235–237] and $mTry = floor(\sqrt{numberoffeatures})$ [237, 238] have been chosen all through for the diagnostic work.

4.6.3 Cross Validation

Cross-validation is a technique to evaluate predictive models by partitioning the original sample into a training set to train the model, and a test set to evaluate it. An N-fold cross validation technique was used for experiments to ensure the un-biases in the results. The N-fold cross-validation technique divides the whole dataset into N uniform folds. Out of which, $N - 1$ folds were used for training and the remaining 1 fold was used for the purpose of testing. In 10-fold cross-validation technique [239], the whole feature dataset is divided into ten uniform folds. The main purpose of doing 10-fold cross validation is to make sure that results remain unbiased. Out of ten folds, nine are used as training data and rest as testing data. This process is repeated ten times so that every sampled data is trained and tested. The average of the all 10 results is the final classification accuracy of the classification. The leave-one-out cross-validation (LOO-CV) approach is used wherever a number of instances for a category are small [240].

4.6.4 Diagnostic Test Evaluation

Many clinical tests are used to confirm the presence of a disease or further the diagnostic process. Ideally, such tests correctly identify all patients with the disease, and similarly correctly identify all patients who are disease free. The following terms are fundamental to understanding the utility of clinical tests:

- True positive: the patient has the disease and the test is positive.
- False positive: the patient does not have the disease but the test is positive.
- True negative: the patient does not have the disease and the test is negative
- False negative: the patient has the disease but the test is negative.

To assess the performance of the classifier we need to calculate sensitivity and specificity [241]. These terms are defined as follows:

1. Sensitivity: It is a measure of the ability of a prediction model to select instances of a certain class from a data set. It is the ratio of true positive decisions to the number of actually positive cases.

$$Sensitivity = \frac{TP}{TP + FN} \tag{4.43}$$

   where, TP: True positive, FN: False negative.

2. Specificity: It is a measure that commonly used in two class problems where one is more interested in a particular class. It is the ratio of true negative decisions to the number of actually negative cases.

$$Specificity = \frac{TN}{FP + TN} \tag{4.44}$$

   where, TN: True negative, FP: False positive.

4.7 Experimental Results and Discussions

The experimental work presented in this section investigates the effectiveness of the texture feature extraction techniques in four color spaces for the classification of severity of MR images in three classes with the help of classifier. The extracted features have been used for the training and testing purpose for SVM classifier with three kernel, i.e. linear, polynomial and radial basis function (RBF) along with RF classifier.

4.7.1 Performance Evaluation of Texture Feature Extraction Techniques

The performance of the texture features has been computed using SVM classifier on the basis of their general performance for pattern recognition and classification task. The classification accuracy has been computed under two categories viz., full feature vector data and mRMR feature selection based reduced feature vector data. To compute the performance of feature extraction techniques two approaches viz., N-fold cross-validation and leave-one-out cross-validation has been adapted.

In the present study total of 1035 (345 $\times$ 3) ultrasound images of MR patients in three views i.e., A2C, A4C, and PLAX were analyzed. Eight different texture feature sets were extracted from the regurgitant area of the ultrasound images as explained in Section 4.4. A total of 56 texture features were extracted from 1035 (345 × 3) echocardiographic images. The MATLAB implementation of LIBSVM has been used for the classification task [221]. The statistical analysis for the 15 best textures in A2C, A4C, and PLAX view corresponding to the highest classification accuracy is shown in Tables 4.3 - 4.5.

For each feature, the value of mean and SD has been computed. The p value of the statistical data set has been determined as 3.42×10^{-9}, which is less than 0.05. This indicates that the features are statistically different from each other [242]. Table 4.6 provides the classification accuracies with spread (SD) obtained by the texture feature extraction techniques using the individual features and the combination of all features, for MR severity. Here, the highest accuracy scores in the RBF kernel SVM are indicated by boldface.

Table 4.3: Statistical analysis of the 15 best texture features in A2C view

Rank	Texture Feature	Mean (μ)	SD (σ)	FO
1	H1 (FDTA)	0.3648	0.0258	51
2	Difference variance (SGLDM mean)	393.5013	63.6242	15
3	Difference variance (SGLDM range)	283.2213	59.8823	28
4	Variance (SGLDM range)	9.2708	5.5133	22
5	Standard deviation (FOS)	60.305	13.6740	3
6	H2 (FDTA)	0.3232	0.0265	52
7	Complexity (SFM)	228056.8	34233.89	39
8	Inverse difference moment (SGLDM range)	0.1126	0.0152	23
9	Sum average (SGLDM range)	0.2736	0.1255	24
10	LS - average texture energy from LS and SL kernels	5624.533	783.1418	50
11	H4 (FDTA)	0.3377	0.0355	54
12	Roughness (SFM)	2.4045	0.0415	44
13	Entropy (SGLDM range)	0.6031	0.0834	27
14	H3 (FDTA)	0.3268	0.0289	53
15	LE - average texture energy from LE and EL kernels	16016.24	2963.57	48

SD: Standard Deviation (σ), FO: Feature Order

Table 4.4: Statistical analysis of the 15 best texture features in A4C view

Rank	Texture Feature	Mean (μ)	SD (σ)	FO
1	Difference variance GLDS	259.6625	69.8727	28
2	FDTA H4	0.3356	0.0340	54
3	H1	0.3621	0.0253	51
4	Inverse difference moment GLDS	0.1039	0.0148	23
5	Sum of squares: variance GLDS	7.4275	4.0996	22
6	Sum entropy GLDS	0.0667	0.0305	26
7	LS - average texture energy from LS and SL kernels	5322.5975	740.4434	50
8	Sum average	0.2036	0.1059	24
9	H2	0.3246	0.0231	52
10	Difference variance	401.9450	63.0305	15
11	Information measures of Corellation 1 SGLDM	-0.2798	0.0223	17
12	Correlation GLDS	0.0742	0.0183	21
13	EE - texture energy from EE kernel	2407.4479	449.0571	46
14	Periodicity	0.6411	0.0232	43
15	H3	0.3251	0.0263	53

SD: Standard Deviation (σ), FO: Feature Order

In A2C view, the achieved classification accuracies for the severity of the MR are 89.89 ± 1.86 and 90.43 ± 1.58 using 10-fold and leave-one-out cross-validation, respectively, based on SGLDM texture feature, while the use of FPS texture feature produced the least classification accuracy i.e., 57.69 ± 2.55 and 56.81 ± 2.67 among all texture features using the RBF kernel. The combination of all the classes of texture features produced higher accuracy instead of using one class of texture features alone and they are 95.08 ± 1.43 and 95.65 ± 1.09 using 10-fold and leave-one-out cross-validation, respectively. The achieved classification accuracy using RF classifier is 92.49 ± 1.65 and 93.33 ± 1.34 with 10-fold and leave-one-out cross-validation, respectively. The performance of the individual features with RF classifier is good compared to the SVM classifier, however, the overall performance of the combination of the features is better in SVM as compared to than RF classifier.

In A4C view, the achieved classification accuracies for the severity of the MR are 90.41 ±

Table 4.5: Statistical analysis of the 15 best texture features in PLAX view

Rank	Texture Feature	Mean (μ)	SD (σ)	FO
1	Sum variance GLDS	434.7543	107.2111	25
2	Sum of squares: variance GLDS	8.5981	4.2737	22
3	H2 FDTA	0.3285	0.0249	52
4	Sum entropy GLDS	0.0568	0.0322	26
5	Periodicity SFM	0.6915	0.0276	43
6	H4	0.3436	0.0375	54
7	Difference variance	272.3842	60.4850	28
8	Information measures	0.1361	0.0083	30
9	H1	0.3691	0.0258	51
10	Information measures of Corellation 1 SGLDM	-0.2866	0.0189	17
11	Correlation SGLDM	0.9242	0.0401	8
12	Inverse difference moment GLDS	0.1178	0.0136	23
13	Difference variance SGLDM	383.1504	65.9721	15
14	EE - texture energy from EE kernel	2356.0515	369.3956	46
15	Sum average	0.2380	0.1277	24

SD: Standard Deviation (σ), FO: Feature Order

1.63 and 91.01 ± 1.54 using 10-fold and leave-one-out cross-validation respectively, based on SGLDM texture feature while the use of FPS texture feature produced the least classification accuracy, i.e., 50.54 ± 1.95 and 51.59 ± 2.69 among all texture features using the RBF kernel. The combination of all texture features produced higher accuracy than that obtained using the individual class features and they are 94.49 ± 1.46 and 95.65 ± 1.09 using 10-fold and leave-one-out cross-validation, respectively. Here, the achieved classification accuracy using RF classifier is 86.67 ± 1.62 and 89.27 ± 1.66 with 10-fold and leave-one-out cross-validation, respectively. The individual performance of features is also same like in A2C view.

In PLAX view, the achieved classification accuracies for the severity of the MR are 90.70 ± 1.28 and 91.01 ± 1.54 using 10-fold and leave-one-out cross-validation, respectively, based on SGLDM texture feature while the use of FPS texture feature produced the least classifica-

Table 4.6: Comparison of classification accuracy achieved by texture feature extraction techniques in A2C, A4C, PLAX view.

		10-Fold CV				LOO-CV			
		Linear	Polynomial	RBF	RF	Linear	Polynomial	RBF	RF
	NoFa	% CA ± SD	% CA ± SD	% CA ± SD	% CA ± SD	% CA ± SD	% CA ± SD	% CA ± SD	% CA ± SD
		A2C View							
ALL	56	84.67±1.80	90.13±1.51	95.08±1.43	92.49±1.65	83.47±1.99	91.01±1.54	95.65±1.09	93.33±1.34
FOS	5	53.91±3.13	54.51±2.77	67.57±1.84	70.19±2.13	54.20±2.68	54.78±2.68	66.37±2.54	70.43±2.46
SGLDM	26	71.90±1.90	88.42±1.60	89.89±1.86	91.62±1.31	73.04±2.39	88.69±1.70	90.43±1.58	91.30±1.51
GLDS	4	52.54±2.75	53.11±1.99	66.98±2.23	68.68±2.78	51.88±2.69	52.17±2.69	65.79±2.55	71.01±2.44
NGTDM	5	55.08±2.22	68.16±2.50	72.76±2.81	82.29±1.29	54.20±2.68	68.69±2.50	74.20±2.35	82.31±2.05
SFM	4	58.60±3.16	69.05±2.27	77.99±2.62	77.10±2.41	57.68±2.66	68.69±2.50	78.55±2.21	77.68±2.24
Laws TEM	6	66.36±2.35	69.61±3.83	80.28±2.13	79.46±1.59	66.08±2.55	69.85±2.47	75.65±2.31	78.84±2.20
FDTA	4	59.48±3.52	61.25±3.32	69.61±2.82	75.11±2.91	56.23±2.67	62.31±2.61	69.27±2.48	72.46±2.40
FPS	2	42.61±2.21	44.95±1.86	57.69±2.55	62.03±2.59	42.31±2.66	45.50±2.68	56.81±2.67	60.28±2.63
		A4C View							
ALL	56	80.78±2.76	85.50±1.79	94.49±1.46	86.67±1.62	78.55±2.20	87.24±1.79	95.65±1.09	89.27±1.66
FOS	5	53.99±2.06	57.10±1.66	67.23±2.27	60.71±2.62	54.78±2.68	55.94±2.67	68.98±2.49	63.76±2.59
SGLDM	26	71.84±2.39	83.12±2.49	90.41±1.63	85.50±1.62	70.72±2.45	85.21±1.91	91.01±1.54	86.66±1.66
GLDS	4	55.67±1.91	59.38±1.99	64.38±3.00	57.15±2.50	56.23±2.67	60.00±2.64	63.18±2.60	55.97±2.66
NGTDM	5	54.75±1.85	60.02±1.68	76.54±2.19	66.49±2.52	53.33±2.68	60.57±2.63	66.66±2.54	66.08±2.55
SFM	4	58.28±2.01	64.68±2.09	71.88±2.76	72.13±2.31	57.97±2.66	64.63±2.57	73.62±2.37	73.91±2.36
Laws TEM	6	63.18±3.02	63.47±1.36	72.98±2.22	69.26±2.01	64.05±2.58	64.05±2.58	74.49±2.35	69.85±2.47
FDTA	4	57.65±1.57	59.97±1.94	66.99±2.56	62.65±2.16	56.81±2.67	57.97±2.66	65.79±2.55	64.05±2.58
FPS	2	50.44±1.70	48.71±1.58	50.54±1.95	55.64±2.51	50.14±2.69	48.69±2.69	51.59±2.69	55.07±2.68
		PLAX View							
ALL	56	81.11±2.11	90.43±1.28	95.63±1.00	87.85±1.16	80.86±2.12	90.43±1.58	95.36±1.13	87.82±1.76
FOS	5	58.83±1.21	59.97±1.56	68.19±2.46	67.58±2.48	60.28±2.63	60.86±2.63	68.11±2.51	70.43±2.46
SGLDM	26	77.64±1.95	84.63±1.68	90.70±1.28	84.64±1.41	76.52±2.28	85.21±1.01	91.01±1.54	85.21±1.91
GLDS	4	50.47±3.11	55.34±1.56	67.84±1.66	71.31±1.20	49.56±2.69	53.91±2.68	68.11±2.51	71.59±2.43
NGTDM	5	50.71±1.23	69.26±2.41	74.19±2.07	76.54±1.67	48.69±2.69	71.01±2.44	73.91±2.36	77.97±2.23
SFM	4	61.76±2.61	61.44±1.45	74.19±1.66	75.33±1.87	59.42±2.64	60.86±2.63	73.33±2.38	74.78±2.34
Laws TEM	6	63.47±2.30	65.78±1.56	76.22±1.49	70.69±1.93	61.44±2.62	66.95±2.53	78.26±2.22	72.17±2.41
FDTA	4	55.96±1.51	59.99±1.28	63.75±2.41	64.07±1.75	55.65±2.67	60.00±2.64	66.37±2.54	64.34±2.58
FPS	2	44.91±0.26	47.80±1.04	51.30±2.49	55.67±2.32	44.92±2.68	47.82±2.69	54.20±2.68	53.04±2.69

NoF: Number of features, CA: Classification accuracy, SD: Standard deviation, RF: Random forest

tion accuracy, i.e., 51.30 ± 2.49 and 54.20 ± 2.68 among all texture features using the RBF kernel. Here again, the combination of all texture features produced higher efficiency than the one obtained by employing SGLDM only, and the values are 95.63 ± 1.00 and 95.36 ± 1.13 in 10-fold and leave-one-out cross-validation, respectively. The achieved classification accuracy using RF classifier is 87.85 ± 1.16 and 87.82 ± 1.76 with 10-fold and leave-one-out cross-validation, respectively.

The RBF kernel SVM classifier gave better performance compared to RF classifier as observed in A2C and A4C views. The results indicate that the FPS texture feature gives the least classification accuracy while SGLDM (mean + range values) feature used in the experiments are a powerful feature for the assessment of the severity of regurgitation in all the three views. Among all the views, the highest percent accuracy of 95.65 with the SD of 1.09 is achieved in A2C and PLAX view. A feature selection technique based on minimum redundancy maximum relevance (mRMR) has been used for feature selection and ranking. Fig. 4.2 shows the classification accuracy for the severity in all three views, 96.82 ± 2.85, 95.08 ± 3.01 and 95.63 ± 3.73 in A2C, A4C, and PLAX view, respectively can be achieved by using top 30 features. It reduced the computation time for the classification.

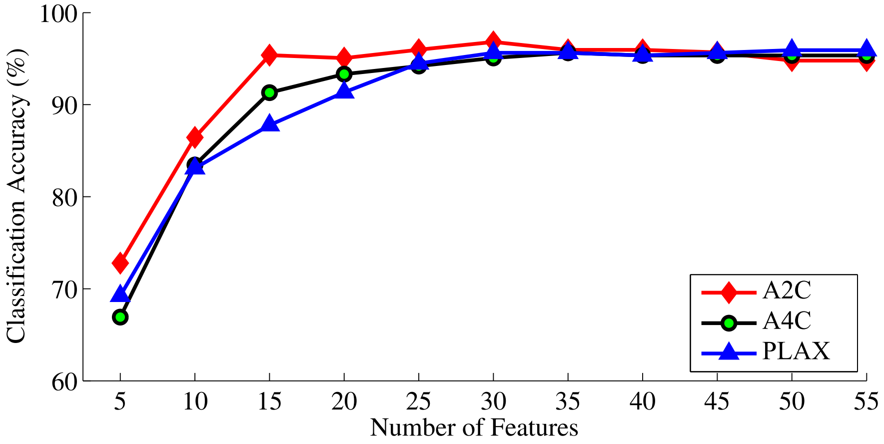

Fig. 4.2: Classification accuracy for the severity of MR after the mRMR feature selection method

4.7.2 Performance Evaluation of Color Spaces

The classification accuracy of the different color components and the combination of all three with individual color space is shown in Table 4.7. The highest accuracy of 97.10 ± 1.06 using *YCbCr* color space in A2C view, 96.21 ± 0.88 and 96.87 ± 0.91 using *RGB* color space has been achieved in A4C and PLAX view, respectively. The comparison of the classifica-

Table 4.7: Performance comparison of color spaces in three view

	Views		
Color Spaces	A2C	A4C	PLAX
R	94.79 ± 1.26	94.49 ± 1.46	95.63 ± 1.00
G	94.79 ± 1.26	96.51 ± 0.73	95.33 ± 1.25
B	95.37 ± 1.06	96.52 ± 0.71	93.89 ± 1.12
RGB	95.66 ± 1.58	96.21 ± 0.88	96.87 ± 0.91
L	96.51 ± 1.28	96.50 ± 0.73	95.63 ± 0.79
A	85.23 ± 2.13	72.15 ± 1.28	74.22 ± 1.86
B	83.73 ± 1.06	75.05 ± 2.25	69.00 ± 2.95
LAB	96.51 ± 1.28	94.13 ± 1.06	92.17 ± 1.29
Y	97.11 ± 1.06	96.85 ± 1.14	94.75 ± 0.86
Cb	82.27 ± 1.86	72.47 ± 1.98	69.00 ± 2.45
Cr	82.34 ± 1.92	69.26 ± 3.20	72.47 ± 2.05
YCbCr	97.10 ± 1.06	93.93 ± 1.23	92.73 ± 1.08
C	94.80 ± 0.82	95.62 ± 1.40	91.61 ± 1.44
Y	92.46 ± 1.43	95.07 ± 0.85	94.18 ± 0.98
M	94.78 ± 1.11	97.09 ± 0.75	93.60 ± 1.63
CYM	94.80 ± 0.82	95.62 ± 1.40	95.94 ± 0.47
GRAY	95.65 ± 2.85	95.65 ± 3.01	95.36 ± 3.73

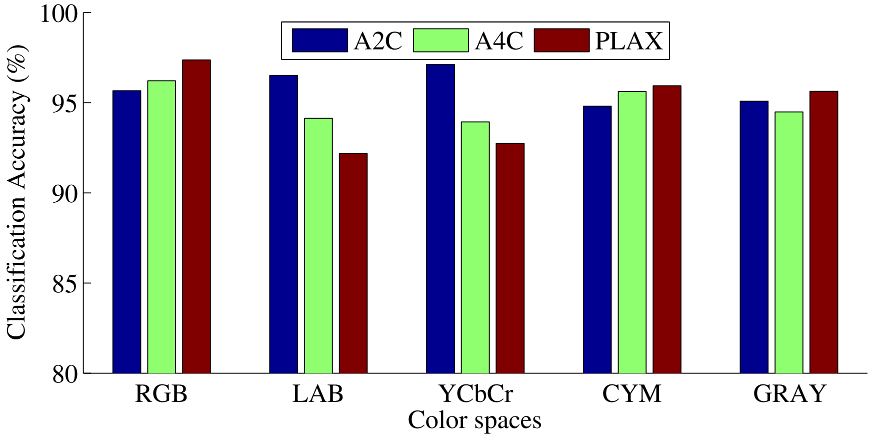

Fig. 4.3: Performance comparison of color spaces in three views

tion accuracy achieved with various color spaces and the classification accuracy obtained by converting the color images into other color spaces is shown in Fig. 4.3. The classification accuracy obtained using *RGB* color space has been found higher than the accuracy obtained by using other color spaces. However, the time required for the texture feature extraction using color spaces is triple to the time required for grayscale image data set. Hence, the further analysis of the texture feature extraction techniques has been done using grayscale images only.

4.7.3 Diagnostic Test Evaluation of Proposed CAD System

The classification performance of the proposed texture features in A2C, A4C and PLAX views are shown in Table 4.6. The performance of a CAD system is evaluated in terms of the sensitivity and specificity. Here, the CAD system is presented for the severity classification of MR images in three classes. The highest classification accuracy has been achieved using the RBF kernel SVM with LOO-CV approach. Therefore, the statistical parameters, namely, sensitivity and specificity have been calculated as discussed in Section 4.6.4. The confusion

Table 4.8: Performance of one-versus-rest SVM classifier in three views.

	Confusion matrix			Statistical parameters	
	Predicted				
Actual	Mild	Moderate	Severe	Sensitivity	Specificity
A2C View					
Mild	10	1	0	90.91	86.36
Moderate	3	13	0	81.25	94.11
Severe	0	0	6	100.00	100.00
A4C View					
Mild	14	2	0	87.50	77.77
Moderate	3	8	0	72.73	86.96
Severe	1	1	5	71.43	100.00
PLAX View					
Mild	15	0	0	100.00	94.11
Moderate	1	10	0	90.91	91.30
Severe	0	2	6	75.00	100.00

matrix of order 3 × 3 has been created because it is a 3 class classification. The performance of one-versus-rest SVM classifier for the combination of all texture features in A2C, A4C and PLAX views, respectively, have been shown in Table 4.8. The results indicate that in A2C view, the highest sensitivity (100 %) for severe class and specificity (100 %) for the mild and moderate class has been achieved. Similarly, in A4C view, the highest sensitivity (87.50 %) and specificity (100 %) has been achieved in mild and severe class, respectively. Finally, in PLAX view, the highest sensitivity (100 %) and specificity (100 %) has been achieved in mild and severe class, respectively.

4.8 Summary

A CAD system has been proposed here for the classification of the severity of MR images based on the multiple spatial domain texture features and supervised classifiers SVM with different kernel functions and RF classifier. The obtained results revealed that there was no single texture feature which could accurately determine the severity of MR. However, the combination of the different texture features improves the classification accuracy. A total 56 texture features were extracted directly from the color Doppler ultrasound images of MR patients, in four color spaces and fed as input to classifiers. It was observed that the classification performance of the CAD system was slightly above when images have been used in RGB color space compared to the gray level color space at the cost of much more computational time. Hence , the further processing and analysis have been done using the grayscale space images. The proposed CAD tool is robust as it has been developed using k-fold cross-validation and LOO-CV technique. The performance of the proposed CAD system is approximately same in both the cross-validation techniques. The LOO-CV method gives slightly higher classification accuracy as compared to 10-fold cross-validation technique, however, the computation time is relatively high in this case. It has been observed that RBF kernel SVM perform better than the RF classifier. So the performance parameters have been calculated for SVM classifier. The 100 % sensitivity and specificity have been achieved in mild and severe class, in PLAX view. The experimental results after using the mRMR feature reduction method exhibited that the top 30 texture features are sufficient to classify the three classes of MR images with the reduced computation time. The obtained results show that the proposed classification method may effectively assist the radiologist in diagnosing patients suffering from MR with better emphasis while reducing the inter-observer variability.

CHAPTER 5

GAUSSIAN PYRAMID BASED TEXTURE ANALYSIS OF MITRAL REGURGITATION

This chapter examines the effectiveness of Gaussian Pyramid (GP) based texture feature extraction techniques for the severity analysis of mitral regurgitation. This chapter presents the description of the GP, and the proposed texture feature extraction techniques and their effectiveness using different classifiers.

5.1 Gaussian Pyramid

The computer vision, image processing, and signal processing communities developed a multi-scale signal representation popularly known as pyramid representation in which a signal or an image is subjected to repeat smoothing and subsampling. The multiresolution analysis of images using pyramid data structures has become a very popular tool in numerous areas of image processing and has been used for texture analysis [142]. Image pyramid is useful for illustrating images at several resolution [146, 148] and has been used for texture analysis [243] due to local averages at various scales [244]. Gaussian Pyramid (GP) [144, 145] and Laplacian image pyramid [146, 147] have been widely used as multiresolution schemes for texture analysis of images.

Here, the most known hierarchical structure Gaussian Pyramid (GP) model has been chosen out of several multiresolution techniques as it is computationally economical. The decomposed image at each and every level has a considerable amount of information about the original image. It consists of the sequence of various images of different resolutions which change in regular steps [148]. In a Gaussian pyramid, subsequent images are weighted down using a Gaussian average (Gaussian blur) and scaled down. Each pixel containing a local average that corresponds to a pixel neighborhood on a lower level of the pyramid. This technique is used especially in texture synthesis. The resolution is high at the bottom of the pyramid while it is low at the top. In image pyramid, the succeeding level image ($G1$), is achieved by sub-sampling the resultant of the convolution of the original image ($G0$) and

Gaussian kernel function (low pass filter). Similarly, the next level image is generating by sub-sampling of the convolution of the output image of the previous level with the Gaussian kernel. The GP for an image $f(x, y)$ is given by:

$$G_0(x, y) = f(x, y) \tag{5.1}$$

$$G_0(x, y) = \sum_{m=-2}^{2} \sum_{n=-2}^{2} w(m, n) \; G_{l-1} \; (2x + m, 2y + n), \quad 0 \leq 1 \leq N \tag{5.2}$$

where, $w(m, n)$ represents the weighting function which remains same at all levels called as generating kernel and approximates the Gaussian function [245]. An example of is the 5-tap filter $\frac{1}{16}\,[1\ 4\ 6\ 4\ 1]$. The decomposed images are shown at $G0$ to $G6$ levels as shown in Fig. 5.1 for a test image. In Eq. 5.1, $G_0(x, y)$ is the first level image (viz., base image) produced

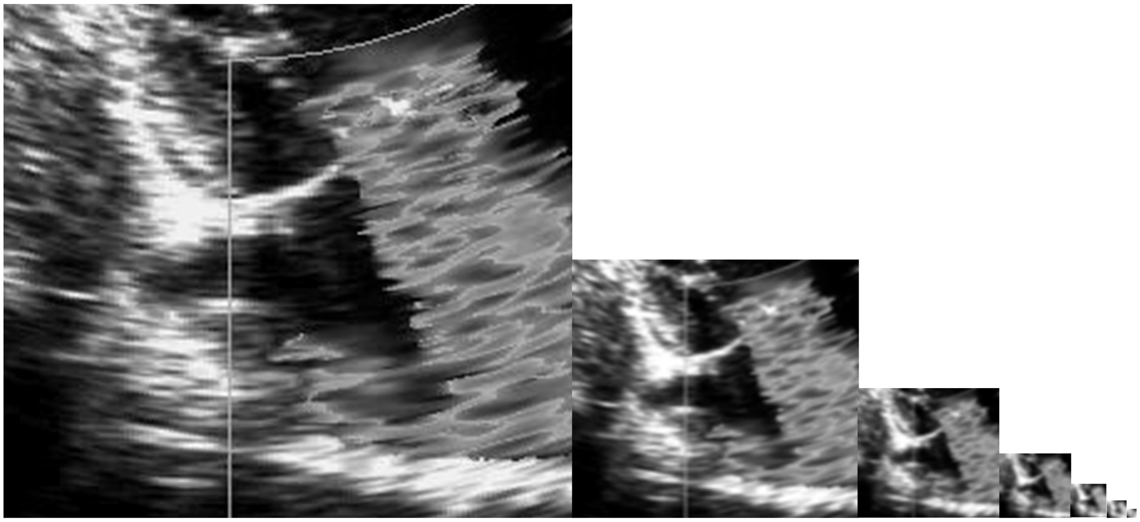

Fig. 5.1: Gaussian pyramid, $G0$ to $G6$ levels presented from left to right.

by Gaussian Pyramid. In Eq. 5.2 $G_l(x, y)$ is the l^{th} level image produced by GP, and $w(m, n)$ is a weighting function (generating kernels). The generating kernel $w(m, n)$ approximates a Gaussian function. These kernels are identical at all levels, symmetric and separable. GP are used for multi-scale edge estimation, efficient to compute coarse scale images. Only 5-tap 1D filter kernels are used, highly redundant, coarse scales provide much of the information in the finer scales.

Table 5.1: Summary of the various studies for classification of heart diseases

Researchers, Year	Classification technique	Diagnosis
Obayya et al., 2008 [164]	Multi-layer FF-NN	CHF and MI diseases
Hanbay et al., 2009 [22]	LS-SVM	Heart valve disease (DHS)
Maglogiannis et al., 2009 [165]	SVM	Heart valve disease (DHS)
Sun et al., 2014 [175]	SVM	VSD
Hedeshi et al., 2014 [24]	Fuzzy-PSO	Coronary artery disease
Gharehbaghi et al., 2015 [176]	HMM-SVM	Cyclic time series
Moghaddasi et al., 2016 [177]	SVM	Mitral regurgitation
Balodi et al., 2016 [178]	SVM	Mitral regurgitation

FF-NN: Feed forward neural network, LS-SVM: Least square support vector machine, SVM: Support vector machine, fuzzy-PSO: Fuzzy-particle swarm optimization, GTSVM: Growing time support vector machine, HMM-SVM: Hybrid hidden Markov model and support vector machine CHF: Congestive heart failure, MI: Myocardial infarction, DHS: Doppler heart sounds, VSD: Ventricular septal defect.

Table 5.1 summarizes the various proposed CAD systems given by several researchers for the characterization and classification of different heart diseases based on statistical texture features. These CAD systems have shown their ability with reasonable accuracy based on the texture features extracted from the images of various medical image data sets in combination with different classifiers.

5.2 Methodology for Gaussian Pyramid based Texture Analysis of MR

The procedural steps involved in present work used for the severity classification of echocardiographic images of MR is represented in the form of block schematic and is shown in Fig. 5.2. The complete classification process is explained as follow:

Step 1: In pre-processing, microscopic images are converted to grayscale model from RGB model using Eq. 4.5.

Step 2: In the second stage, these images are transformed to multiresolution images by means of GP. The GP model at G0 to G6 levels has been achieved by convolving grayscale

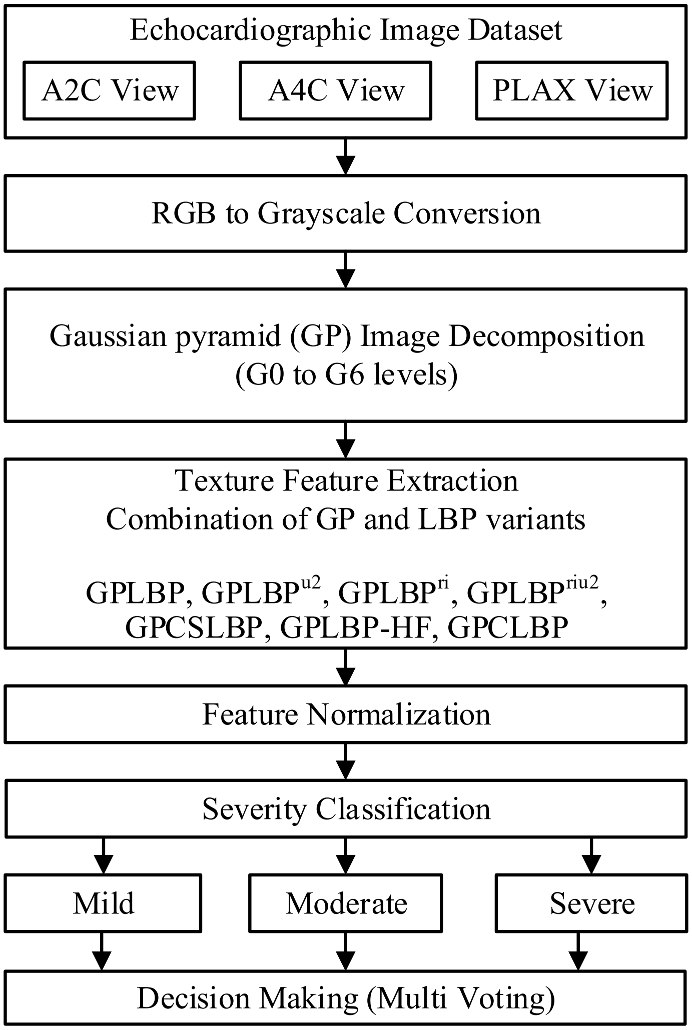

Fig. 5.2: Schematic for classification of MR using Gaussian image pyramid based texture feature extraction techniques.

images with the Gaussian kernel (low pass filter). From each GP decomposed images, texture features are extracted using different texture descriptors like LBP. The texture features produced by these feature extraction techniques produces a wide range of numerical values.

Step 3: A normalization process is thus considered necessary to make the feature vector data suitable for directly applying it to the classifier. The feature vector data has been normalized in the range of 0 to 1 using Eq. 4.6.

Step 4: Each and every level of the multiresolution image has significantly distinctive information about the original image. The normalized texture feature vectors are combined cumulatively to form level 1 to level 7 feature vectors as given by Eq. 5.3.

$$F_L = \sum_{l=1}^{l=L} G_l \tag{5.3}$$

Step 5: In the final step, classifiers have been employed to classify the MR images into three categories using GP based texture feature vector data. Consequently, the best combination of texture feature technique with a classifier is obtained to classify the MR decided on the basis of the best classification accuracy. Thus, on the basis of a combination of GP with different variants of texture feature descriptors, following texture feature extraction techniques are proposed here, and they are listed as below with their notations and variations in Table 5.2.

Table 5.2: Proposed texture features and their notations

Notation	Texture feature full name
GPLBP	Gaussian pyramid based local binary pattern
GPLBP^{u2}	Gaussian pyramid based uniform local binary pattern
GPLBP^{ri}	Gaussian pyramid based rotation invariant local binary pattern
GPLBP^{riu2}	Gaussian pyramid based rotation invariant uniform local binary pattern
GPCSLBP	Gaussian pyramid based center-symmetric local binary pattern
GPLBP-HF	Gaussian pyramid based local binary pattern histogram Fourier features
GPCLBP	Gaussian pyramid based completed local binary pattern

5.3 Texture Feature Extraction

In the following section, texture feature descriptors as discussed above are briefly explained:

5.3.1 Local Binary Pattern (LBP)

Ojala et al. [126] have proposed a first-order circular derivative of patterns that are generated by concatenating the binary gradient directions. This texture operator labels every pixel by the relative gray levels of its neighboring pixels. The LBP has shown its potential in the areas such as face recognition, object identification, image classification, etc. It is computational efficient [246–248]. A circular neighborhood of variable size was proposed by Ojala et al., [249] to overcome the inadequacy of original LBP operator of 3×3 neighborhood size that cannot capture the dominant texture features in large-scale structures. A center pixel coordinate $(x,\ y)$ of an image is represented as LBP label given by Eq. 5.4.

$$LBP_{P,R}\,(x,\,y) = \sum_{p=0}^{p-1} s(g_p - g_c)2^p \tag{5.4}$$

$$s(x)\ = \begin{cases} 1, & x \geq 0 \\ 0, & otherwise \end{cases}$$

where, g_c corresponds to the gray level of the central pixel and g_p corresponds to the gray levels of the pth neighborhood of the central pixel. In LBP$_{P,R}$ operator, P represents the number of pixels in the neighborhood, and R is the radius. The histogram of these binary numbers is then used to describe the texture of the image.

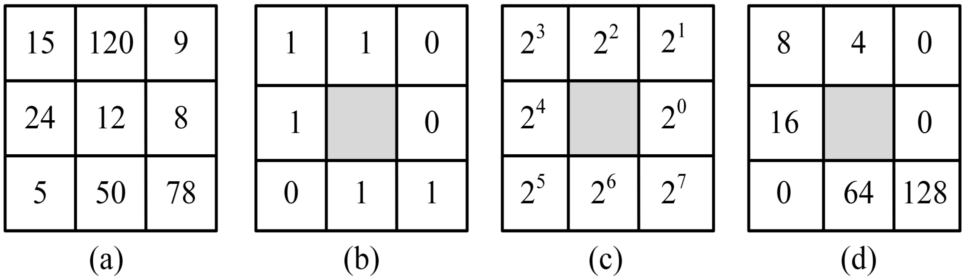

15	120	9
24	12	8
5	50	78

(a)

1	1	0
1		0
0	1	1

(b)

2^3	2^2	2^1
2^4		2^0
2^5	2^6	2^7

(c)

8	4	0
16		0
0	64	128

(d)

Fig. 5.3: The LBP computation process (a) 3×3 local window image, (b) thresholding, (c) weight and (d) new center pixel value $= 0 + 0 + 4 + 8 + 16 + 0 + 64 + 128 = 218$

5.3.2 Uniform Local Binary Pattern (LBP^{u2})

The LBP patterns are said to be uniform if at most 2-bitwise transition are reported (1 to 0 or 0 to 1) is reported in the circular binary pattern of LBP [126]. The LBP^{u2} histogram comprises separate bin for uniform patterns and the only single bin is assigned to all the non-uniform patterns. For a given pattern of P bits, $P(P-1)+3$ outputs bin are produced. The reduction in non-uniform patterns is due to the fact that in natural images the LBP patterns are mostly uniform. Further, uniform patterns of texture images account for about 90 % of the entire pattern with (8, 1) neighborhood and close to 70 % for (16, 2) neighborhood [127, 250]. The LBP^{u2} produces 59-dimensional texture descriptors.

5.3.3 Rotation Invariant Local Binary Pattern (LBP^{ri})

The rotation of an image results into diverse LBP codes. To address the issue of the image rotation effect, LBP^{ri} has been proposed in [126, 127, 251]. Thus, to make all the versions of binary codes the same, the LBP codes are rotated back to reference pixel position to nullify the consequence of translation of a pixel location. The LBP$^{ri}_{P,R}$ is generated by circularly rotating the basic LBP code and considering the pattern which has a minimum value as given by [126, 127, 251]:

$$LBP^{ri}_{P,R} = min\{ROR(LBP_{P,R}, i)|i = 0, 1, ..., p - 1\} \tag{5.5}$$

where, the superscript ri stands for "roration invariant". The function $ROR(x, i)$ circularly shifts the P bit binary number x, i times to the right ($|i| < P$). The LBP$^{ri}_{P,R}$ descriptor produces overall 36-bin histograms for each image due to 36 diverse, 8 bit rotation invariant codes [127, 251].

5.3.4 Rotation Invariant Uniform Local Binary Pattern (LBP^{riu2})

To overcome the disadvantages associated with $LBP^{riu2}_{P,R}$ (poor performance because of crude quantization of angular space at 45°) $LBP^{riu2}_{P,R}$ was proposed in [127]. If a pattern has uniformity value $U \leq 2$, it is known as "uniform" pattern, $U(x)$, which is as given by Eq. 5.6.

$$U(x) = \sum_{p=0}^{P-1} F_b(x \oplus ROR(x, 1), p) \tag{5.6}$$

where, b stands for binary numbers. Given a binary number x, the circularly consecutive binary bits b are obtained by [127]:

$$F_b(x, i) = ROR(x, i) \cdot (2^b - 1) \tag{5.7}$$

The bitwise logical operators "XOR" and "AND" are denoted by '$\oplus$' and $\cdot$ (dot) operator, respectively and for a given bit sequence, i signifies the index of least significant bit (LSB). The rotation of uniform codes towards their minimum value generates $(P + 1)$ patterns. Merely counting the number of one's in the "uniform" patterns, binary number generates LBP$^{riu2}_{P,R}$ pattern code. The other patterns are marked "miscellaneous" and grouped into a single value as given by:

$$LBP_{P,R}^{riu2} = \begin{cases} \sum_{p=0}^{P-1} s(g_p - g_c), U(G_p) \leq 2 \\ P + 1, otherwise \end{cases} \tag{5.8}$$

The $\mathrm{LBP}_{P,R}^{riu2}$ produces 10-bin histograms.

5.3.5 Center-symmetric Local Binary Pattern (CSLBP)

Heikkilä et al. [252] have proposed a texture feature CSLBP, it combines the strength of LBP and scale-invariant feature transform (SIFT). Here, center-symmetric pairs of pixels are compared instead of comparing each pixel with the center pixel. This halves the number of comparison for the same number of neighbors. The new center pixel value in CSLBP (encompassing the advantageous characteristics of texture and gradient-based features [253]) is produced by comparing center symmetric pixels, contrary to comparing each of the neighborhood pixels with center pixels in LBP. The schematic representation for CSLBP descriptor is given in Fig. 5.4. For 8 neighborhood total 2^4 (16) binary pattern is produced by CSLBP whereas LBP produces 2^8 (256) binary patterns.

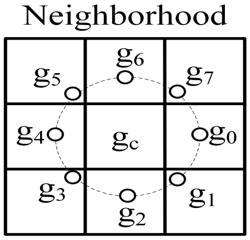

Fig. 5.4: CSLBP features (considering neighbohood size of 8 pixels)

$$CSLBP_{8,1} = \left[s(|g_0 - g_4|)2^0 + s(|g_1 - g_5|)2^1 + s(|g_2 - g_6|)2^2 + s(|g_3 - g_7|)2^3\right] \tag{5.9}$$

Mathematically, CSLBP is expressed as [252]:

$$CSLBP_{R,N,T}(x, y) = \sum_{p=0}^{N/2-1} s(g_p - g_{p+(N/2)})2^p \tag{5.10}$$

$$s(x) = \begin{cases} 1, & x > T \\ 0, & otherwise \end{cases}$$

where, n_i and $n_{i+(N/2)}$are the gray values of center-symmetric pairs of pixels of *N* equally spaced pixels in a circle of radius *R* and $s(x)$ represents the thresholding function. For N neighborhood CSLBP resulting in $2^{N/2}$ different pattern. For 8 neighborhood CSLBP produces 16 different binary patterns.

5.3.6 Local Binary Pattern Histogram Fourier Features (LBP-HF)

Ahonen et al. [254] have proposed a rotation invariant image descriptor computed from discrete Fourier transforms (DFT) of LBP histograms. LBP-HF features hold the extremely discriminative nature of LBP histograms. To get the LBP-HF descriptor first to calculate a non-invariant LBP histogram over the whole region then constructing rotationally invariant features from the histogram. In this, the rotation invariance is earned globally, and therefore the features are invariant to rotations [255]. To construct the features the DFT is given by:

$$H(n,u) = \sum_{r=0}^{P-1} h_l(U_P(n,r))\ e^{-j\pi ur/P} \tag{5.11}$$

where, $H(n,u)$ corresponds to DFT of the n^{th} row of LBP^{u2} histogram $h_l(U_P(n,r))$. It produces 38-bin histogram for a given image.

5.3.7 Completed Local Binary Pattern (CLBP)

Guo et al. [256] have proposed CLBP so as to enhance the texture feature ability of LBP. A neighborhood region is represented by its center pixel and a local difference sign-magnitude transform (LDSMT). The structure of CLBP is depicted in Fig. 5.5. Fig. 5.6 shows 3×3 blocks of an image having center pixel value 28. The local difference, sign component, and magnitude components are illustrated in Fig. 5.6.

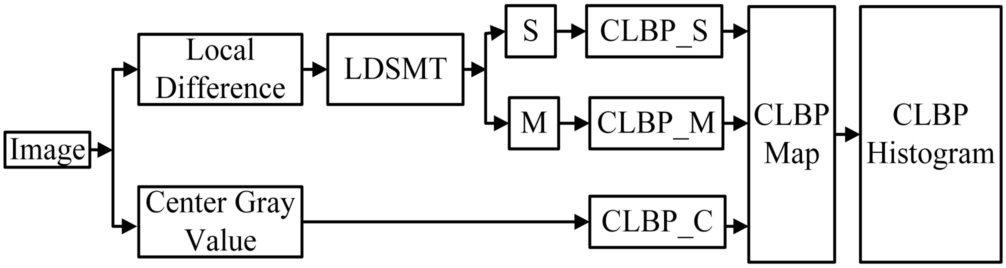

Fig. 5.5: CLBP structure

15	134	25
82	28	47
58	12	19

(a)

-13	106	-3
54		19
30	-16	-9

(b)

-1	1	-1
1		1
1	-1	-1

(c)

13	106	3
54		19
30	16	9

(d)

Fig. 5.6: The CLBP computation process (a) 3×3 local window image, (b) local difference $(g_p - g_c)$, (c) sign component, and (d) magnitude component

The LDSMT is given as [256]:

$$d_p = g_p - g_c = s_p * m_p, \quad and \begin{cases} s_p & = sign(d_p) \\ m_p & = |d_p| \end{cases} \tag{5.12}$$

$$s_p = \begin{cases} 1, & d_p \geq 0 \\ -1, & d_p < 0 \end{cases}$$

where, m_p and s_p represents the magnitude and sign of d_p, respectively.

The center pixels represent the image gray level and they are regenerated into a code, specifically CLBP-Center (CLBP_C), by global thresholding [130]. The LDSMT decomposes the image into two complementary components i.e. signs and magnitudes based on the image local differences, namely CLBP-Sign (CLBP_S) and CLBP-Magnitude (CLBP_M).

5.4 Classification

In the present work, the performance of the proposed CAD system using the proposed texture feature extraction techniques have been evaluated using two supervised classifiers i.e. support vector machine (SVM) [220, 221] and random forest (RF) classifier [222]. The details and tuning parameters of SVM and RF classifier have been discussed in Section 4.6.1 and 4.6.2. To maintain unbiasness 10-fold cross-validation has been used. The detail of cross-validation has been given in Section 4.6.3. The diagnostic performance of a CAD system is evaluated using sensitivity and specificity, as explained in Section 4.6.4.

5.5 Experimental Results and Discussion

The applicability of the proposed GP based texture features for the classification of the severity of MR has been evaluated here. Two supervised classifiers i.e. SVM and RF have been used for the classification task. Here, two type of the experiments have been performed using texture features based on LBP variants and GP based multiresolution with with LBP variants. The results in each case are presented below:

5.5.1 Classification Performance of LBP Variants

In the first experiment, the performance of the existing variants of LBP features such as LBP^{u2}, LBP^{ri} LBP^{riu2}, CSLBP, LBP-HF, and CLBP have been evaluated. All the texture features are extracted using *P*=8 and *R*=1, for each decomposition level. The classification accuracy of the existing LBP variants is shown in Table 5.3. The highest classification accuracies are obtained using the CLBP technique with RBF kernel SVM classifier and values are 90.17 ± 1.84, 88.72 ± 1.89 and 87.24 ± 2.00 in A2C, A4C, and PLAX view, respectively. The second best classification accuracies of 84.37 ± 1.75, 80.63 ± 2.61 and 83.50 ± 2.09 in A2C, A4C, and PLAX view, respectively have been achieved for LBP^{u2}. RF classifier did not perform well as compared to SVM classifier. The highest classification accuracy achieved using RF classifier are 86.43 ± 2.15, 80.00 ± 2.04, and 78.57 ± 1.46 in A2C, A4C, and PLAX views respectively. The results in Table 5.3 portray that the RBF kernel performs better than RF classifier.

Table 5.3: Classification performance of existing texture feature extraction techniques

Feature extraction technique	No. of feature	SVM Classifier			RF Classifier		
		A2C	A4C	PLAX	A2C	A4C	PLAX
LBP	256	76.84±5.30	78.85±2.59	71.89±2.11	75.37±2.63	68.94±3.10	74.47±1.49
LBPu2	59	84.37±1.75	80.63±2.61	83.50±2.09	80.62±2.65	71.01±1.86	74.49±2.12
LBPri	36	62.79±2.93	67.53±2.87	60.53±2.38	71.64±2.44	68.97±1.80	71.88±1.96
LBPriu2	10	74.51±2.03	69.59±2.14	71.60±2.23	76.26±2.86	72.46±1.63	69.00±1.90
CSLBP	16	83.50±2.62	79.97±2.12	76.20±2.40	78.54±1.86	77.09±2.06	76.26±1.43
LBP-HF	76	78.56±1.61	71.26±2.42	75.50±2.44	80.03±3.57	77.34±2.30	74.17±1.63
CLBP	118	90.17±1.84	88.72±1.89	87.24±2.00	86.43±2.15	80.00±2.04	78.57±1.46

5.5.2 Classification Performance of GP Based LBP Variants

In the second experiment, the multiresolution analysis with LBP variants has been evaluated. Here, the images are decomposed to six levels using GP structure as explained in the Section 5.1. The image size is reduced to each level of decomposition therefore after sixth level image decomposition, feature extraction is not possible. Further, the texture features of these decomposed images have been extracted by employing LBP variants as explained in Section 5.3 at different levels. For all the variants of LBP, the value of P=8 and R=1 is fixed for each level of image decomposition. These features are then concatenated to generate feature vector used for the training and testing of the classifier.

Tables 5.4, 5.5, and 5.6 show the classification performance of the proposed hybrid texture feature increases with the extent of image decomposition level in all three views. The progressive variation might vary for proposed features within the varied level of the image decomposition. The highest classification accuracies are achieved using the proposed feature GPCLBP at the sixth level in all three views. The achieved classification accuracies are 95.66 ± 0.98, 94.47 ± 1.91 and 94.21 ± 1.31 followed by the GPLBP^{u2} for which the classification accuracies have been 91.89 ± 1.11, 95.92 ± 1.24 and 92.46 ± 0.87 at the fifth level of decomposition of A2C and A4C view and at the sixth level of PLAX view, respectively using the RBF kernel based SVM classifier. The classification performance of the existing LBP variants have been improved significantly and this can be verified by the experimental results.

The performance of the RF classifier is also reported in Tables 5.4, 5.5, and 5.6. It is observed that the highest classification accuracy achieved using RF classifier are 86.73 ± 2.47, 82.03 ± 1.82, and 78.59 ± 1.55. The response of the extracted features has been reported better in RBF kernel based SVM classifier compared to other two kernel of SVM i.e., linear, polynomial and the RF classifier.

The proposed GPCLBP feature performed the best among all followed by GPLBP^{u2}, whereas GPLBP^{ri} has shown the lowest performance in all three views. It also confirmed that the proposed features have improved the ability of the LBP variants for the severity classification of MR significantly in all three views. Fig. 5.7 gives the performance comparison of the three kernel of SVM classifier using GPCLBP texture feature.

Table 5.4: Classification accuracy of GP based texture features in A2C view

Fearure	IDL	NoF	SVM Classifier			RF Classifier
			Linear	Poly	RBF	
GPLBP	Level 1	512	65.52±2.79	67.82±2.43	80.32±3.29	78.30±3.37
	Level 2	768	63.49±3.04	67.82±2.55	75.10±2.88	78.00±3.29
	Level 3	1024	62.08±2.60	64.61±1.45	71.32±1.78	79.48±3.54
	Level 4	1280	79.78±2.21	67.23±2.20	80.32±1.71	91.33±1.80
	Level 5	1536	79.77±2.23	67.80±2.84	80.93±2.77	80.62±3.15
	Level 6	1792	80.05±2.27	68.36±2.62	80.92±2.49	79.74±2.34
GPLBP^{u2}	Level 1	118	62.92±2.29	82.41±3.08	87.60±2.35	82.05±2.91
	Level 2	177	60.62±2.73	84.97±3.48	88.45±1.75	81.47±2.84
	Level 3	236	65.26±3.00	86.69±2.75	89.86±1.56	81.47±3.23
	Level 4	295	72.50±1.48	87.85±1.91	91.29±1.94	83.51±2.51
	Level 5	354	74.80±1.34	87.83±1.48	91.90±1.11	80.09±2.47
	Level 6	413	74.81±1.63	86.96±1.79	91.61±1.00	84.09±2.33
GPLBP^{ri}	Level 1	72	58.55±2.54	62.67±3.26	68.11±2.76	72.78±2.64
	Level 2	108	56.24±2.71	59.76±2.78	65.83±1.86	70.75±3.23
	Level 3	144	58.53±2.89	60.59±2.08	67.21±2.89	70.78±3.17
	Level 4	180	60.89±1.61	61.76±2.59	69.84±2.06	71.34±3.14
	Level 5	216	62.65±2.36	67.29±1.86	75.39±1.86	72.79±2.70
	Level 6	252	66.11±1.50	69.31±1.83	75.95±2.06	73.63±3.14
GPLBP^{riu2}	Level 1	20	53.95±2.58	66.10±2.14	80.03±1.28	78.05±2.68
	Level 2	30	53.95±2.78	66.68±2.10	77.43±2.56	77.17±2.21
	Level 3	40	54.27±4.34	66.40±3.21	75.98±2.31	78.03±2.53
	Level 4	50	53.12±3.49	65.82±1.72	72.48±2.63	76.29±2.23
	Level 5	60	56.87±3.85	67.55±2.19	76.24±1.90	75.71±2.65
	Level 6	70	59.13±2.75	71.03±2.85	80.00±2.19	75.68±1.99
GPCSLBP	Level 1	32	57.12±2.31	79.69±1.69	86.11±2.33	83.47±1.57
	Level 2	48	60.31±2.29	84.64±2.69	86.08±1.77	84.63±1.63
	Level 3	64	60.00±1.93	84.62±2.55	90.18±1.59	84.95±1.51
	Level 4	80	65.83±1.51	84.03±2.14	88.71±1.44	85.51±1.43
	Level 5	96	65.83±2.53	84.61±2.64	91.03±1.07	87.26±2.06
	Level 6	112	72.80±1.72	84.07±2.92	90.76±1.57	89.86±2.08
GPLBP-HF	Level 1	152	67.00±2.91	75.38±2.04	82.36±1.81	82.63±2.21
	Level 2	228	64.67±1.90	76.82±2.66	83.20±1.65	84.07±2.13
	Level 3	304	63.27±2.45	83.78±2.46	84.36±1.65	82.60±2.51
	Level 4	380	67.02±2.68	84.97±2.19	87.24±1.09	80.27±2.20
	Level 5	456	67.55±1.78	82.05±2.08	85.81±2.13	80.29±2.26
	Level 6	532	70.13±2.97	84.92±2.02	86.08±1.54	79.42±2.12
GPCLBP	Level 1	236	76.58±1.66	87.55±1.62	91.32±1.43	85.27±2.30
	Level 2	354	71.05±1.77	88.73±2.23	92.50±1.35	85.84±2.56
	Level 3	472	71.35±2.29	89.00±1.58	91.63±1.22	86.44±2.43
	Level 4	590	82.34±1.78	88.41±1.49	94.22±0.86	86.73±2.47
	Level 5	708	82.34±1.78	88.41±1.49	94.22±0.86	85.00±2.76
	Level 6	826	88.47±1.88	86.10±1.48	95.66±0.99	86.43±2.15

Table 5.5: Classification accuracy of GP based texture features in A4C view

Fearure	IDL	NoF	SVM Classifier			RF Classifier
			Linear	Poly	RBF	
GPLBP	Level 1	512	66.67±2.57	60.56±1.62	76.79±2.44	71.56±2.92
	Level 2	768	68.70±2.94	57.96±1.89	74.47±2.33	71.55±2.36
	Level 3	1024	75.65±2.15	55.34±1.94	75.08±2.37	72.74±2.28
	Level 4	1280	79.71±1.86	51.60±1.34	75.95±2.15	71.26±2.49
	Level 5	1536	82.90±2.06	50.75±1.46	79.44±1.79	74.75±2.19
	Level 6	1792	83.19±2.21	49.87±0.93	80.28±2.09	72.43±1.87
GPLBP^{u2}	Level 1	118	58.23±2.06	84.34±2.30	92.16±1.61	79.15±2.88
	Level 2	177	69.32±1.46	86.40±1.47	90.47±2.66	77.13±2.69
	Level 3	236	75.93±2.74	86.38±1.49	91.87±1.54	77.41±2.35
	Level 4	295	75.67±3.12	86.07±1.15	94.17±1.58	78.57±2.03
	Level 5	354	78.82±1.80	85.76±1.72	95.92±1.24	80.59±1.93
	Level 6	413	82.64±1.68	86.92±1.48	94.49±0.92	79.13±2.25
GPLBP^{ri}	Level 1	72	56.79±2.91	58.25±2.87	66.13±2.63	70.40±1.67
	Level 2	108	54.79±2.33	55.91±2.62	67.53±2.53	70.44±2.23
	Level 3	144	57.37±2.72	56.21±2.71	71.54±2.56	66.68±1.64
	Level 4	180	56.21±2.60	56.24±2.09	70.72±2.09	68.66±1.28
	Level 5	216	62.29±2.39	57.08±2.28	70.43±2.82	68.96±1.60
	Level 6	252	65.23±2.36	56.53±2.47	73.07±2.59	68.69±1.77
GPLBP^{riu2}	Level 1	20	60.05±2.46	65.32±3.33	74.49±1.53	74.77±2.09
	Level 2	30	62.65±2.14	61.24±3.08	71.87±3.07	73.92±1.68
	Level 3	40	63.79±1.64	64.98±2.13	71.92±1.59	70.72±2.03
	Level 4	50	66.71±2.92	65.28±2.77	77.73±2.55	70.72±1.85
	Level 5	60	61.76±1.45	75.07±1.81	80.60±1.48	72.17±1.50
	Level 6	70	66.70±2.47	78.03±2.63	81.20±1.94	72.47±1.65
GPCSLBP	Level 1	32	60.87±2.37	79.98±1.34	85.51±2.39	75.66±3.13
	Level 2	48	55.65±2.83	78.82±2.31	84.65±2.13	77.67±2.77
	Level 3	64	59.41±2.55	82.29±1.99	86.13±1.89	77.97±2.62
	Level 4	80	63.17±3.07	85.76±1.79	87.55±1.36	80.83±2.14
	Level 5	96	62.31±2.04	85.23±1.64	87.27±1.62	82.57±2.23
	Level 6	112	66.37±1.32	86.70±1.88	88.71±1.64	83.16±1.94
GPLBP-HF	Level 1	152	56.84±1.48	68.92±2.74	77.08±2.03	76.15±2.47
	Level 2	228	66.11±1.90	71.29±2.36	79.41±1.65	74.72±2.14
	Level 3	304	61.46±2.21	70.69±2.75	77.39±2.89	72.41±2.01
	Level 4	380	63.45±2.90	71.54±2.14	79.70±2.80	73.59±1.68
	Level 5	456	67.58±3.34	71.85±1.99	82.60±2.45	74.16±1.51
	Level 6	532	70.47±2.79	75.34±2.07	82.63±2.68	72.43±2.43
GPCLBP	Level 1	236	68.43±2.85	86.66±2.15	91.31±2.04	82.02±2.67
	Level 2	354	73.40±2.78	85.76±1.93	91.29±2.13	80.58±2.38
	Level 3	472	77.97±2.81	83.74±1.59	90.43±1.84	81.44±2.24
	Level 4	590	81.45±2.04	82.28±2.04	91.85±1.85	80.29±2.10
	Level 5	708	82.58±2.66	77.66±2.25	93.59±1.94	82.03±1.82
	Level 6	826	84.63±2.18	74.17±2.44	94.48±1.91	80.00±2.04

Table 5.6: Classification accuracy of GP based texture features in PLAX view

Fearure	IDL	NoF	SVM Classifier			RF Classifier
			Linear	Poly	RBF	
GPLBP	Level 1	512	60.60±2.87	57.71±1.84	71.92±1.36	72.74±1.94
	Level 2	768	64.09±1.97	53.32±1.13	70.15±1.71	71.89±1.34
	Level 3	1024	68.97±2.05	52.46±1.05	72.18±1.41	70.45±1.61
	Level 4	1280	76.51±1.54	52.75±0.87	75.08±1.71	73.05±1.53
	Level 5	1536	80.32±1.98	52.75±0.87	78.55±0.96	72.51±1.85
	Level 6	1792	81.17±1.44	52.46±0.96	81.16±1.38	71.31±1.06
GPLBP^{u2}	Level 1	118	58.56±2.01	79.76±1.36	83.8±2.53	78.26±1.87
	Level 2	177	56.56±2.17	82.96±1.89	80.61±2.01	78.55±0.97
	Level 3	236	62.90±1.74	84.42±2.39	84.92±0.94	78.86±1.32
	Level 4	295	74.51±1.37	86.71±1.47	89.57±0.87	79.12±1.35
	Level 5	354	75.07±1.56	89.87±0.86	91.63±1.61	79.41±1.46
	Level 6	413	79.45±1.86	91.90±1.46	92.46±0.88	79.44±1.59
GPLBP^{ri}	Level 1	72	53.06±2.55	55.12±3.54	65.78±2.58	68.68±2.00
	Level 2	108	54.17±2.74	54.48±2.24	58.25±1.54	69.55±2.17
	Level 3	144	53.08±3.60	53.06±1.42	60.58±2.83	67.49±2.10
	Level 4	180	53.90±3.49	55.34±1.61	61.16±2.89	69.55±2.25
	Level 5	216	57.13±2.77	54.47±1.43	65.77±3.69	69.87±1.68
	Level 6	252	56.24±2.62	56.20±1.81	68.65±2.59	69.55±1.62
GPLBP^{riu2}	Level 1	20	60.00±1.98	65.57±2.52	78.56±1.86	73.61±1.94
	Level 2	30	57.99±2.44	65.03±3.45	76.87±2.89	72.77±2.02
	Level 3	40	59.17±2.58	63.61±3.61	77.11±2.69	73.06±1.97
	Level 4	50	58.04±2.55	68.73±1.95	77.12±3.01	76.52±1.69
	Level 5	60	59.18±2.10	73.39±2.38	82.00±2.52	72.78±2.01
	Level 6	70	60.62±3.04	78.85±1.83	82.85±2.52	74.52±1.54
GPCSLBP	Level 1	32	59.78±3.31	74.57±2.86	80.00±1.68	79.40±1.77
	Level 2	48	57.72±2.16	78.32±2.06	82.09±2.25	78.84±1.67
	Level 3	64	61.48±2.45	82.95±2.01	86.99±1.33	78.28±1.13
	Level 4	80	62.02±2.16	86.96±0.89	87.55±1.22	77.42±1.51
	Level 5	96	65.82±3.06	88.97±1.21	89.85±0.66	76.60±1.74
	Level 6	112	72.52±3.06	92.44±1.39	92.15±1.08	78.65±2.15
GPLBP-HF	Level 1	152	56.81±2.41	68.71±3.00	73.34±1.28	75.37±1.53
	Level 2	228	60.30±2.61	70.16±2.49	75.09±1.71	74.19±1.35
	Level 3	304	65.27±2.98	74.21±2.15	76.34±1.91	72.73±1.73
	Level 4	380	63.45±1.67	77.69±2.20	81.45±1.67	75.08±1.83
	Level 5	456	66.40±1.89	77.13±1.77	83.78±1.92	71.85±1.42
	Level 6	532	68.41±2.26	77.11±1.43	84.34±1.38	73.60±2.14
GPCLBP	Level 1	236	68.10±3.01	85.23±1.56	89.86±1.17	77.97±0.87
	Level 2	354	69.86±1.62	83.80±1.96	89.55±1.24	77.40±1.33
	Level 3	472	75.70±2.51	80.29±1.36	90.15±1.31	78.29±1.58
	Level 4	590	82.04±2.04	79.71±1.58	91.33±1.60	78.59±1.55
	Level 5	708	85.23±2.08	77.42±1.95	91.61±0.90	78.57±1.46
	Level 6	826	88.71±2.32	75.39±2.06	94.21±1.14	78.57±1.46

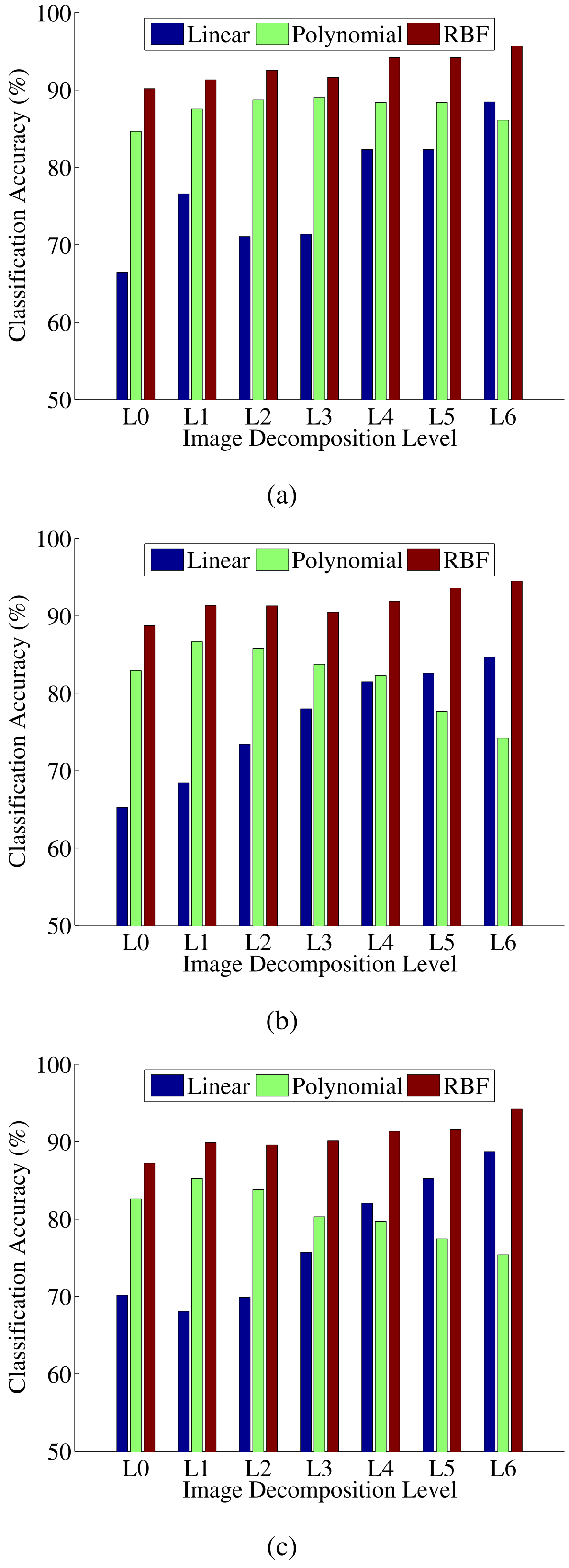

Fig. 5.7: Comparison of three kernel of SVM classifier in three views (a) A2C view (b) A4C view (c) PLAX view

Table 5.7: Performance of one-versus-rest SVM classifier in three views.

	Confusion matrix			Statistical parameters	
	Predicted			Sensitivity	Specificity
Actual	Mild	Moderate	Severe		
A2C View					
Mild	133	7	0	95.00	99.02
Moderate	2	137	1	97.85	94.14
Severe	0	5	60	92.30	99.64
A4C View					
Mild	158	2	0	98.75	92.43
Moderate	13	101	1	87.82	98.26
Severe	1	2	67	95.71	99.63
PLAX View					
Mild	153	2	0	98.70	92.63
Moderate	9	94	2	89.52	98.33
Severe	5	2	78	91.76	99.23

5.5.3 Diagnostic Test Evaluation of Proposed CAD System

The performance of a classification tool or CAD system can be analyzed by two statistical parameters, i.e., sensitivity and specificity. Here, the severity of MR has been classified within the stages i.e. mild, moderate and severe. Hence, the confusion matrix of the order of 3×3 has been obtained. The GPCLBP texture features outperformed in all three views. Therefore the statistical parameters of one-versus-all have been calculated and shown in Table 5.7. It has been observed from Table 5.7 that in the A2C view, seven three and five misclassification cases were reported in mild, moderate and severe class. Further, in A4C view, two, fourteen and three cases were misclassified. Subsequently, in PLAX view, two cases in mild, eleven cases in moderate, and seven cases in the severe class were reported in the wrong class. The highest sensitivity of 97.85 $\%$, 98.75 $\%$, and 98.70 $\%$ similarly, the highest specificity 99.64 $\%$, 99.63 $\%$, and 99.23 $\%$ have been achieved for A2C, A4C and PLAX views, respectively for the different class.

5.6 Summary

In this chapter, a CAD system (for the severity analysis of MR) using the hybrid texture features based on GP and LBP variants has been presented. The proposed methodology consists of three basic steps. In the first step, the images are converted to a grayscale image and a region of interest is selected through an arbitrary method. In the second step, the GP structure is used as a multiresolution scheme to decompose images up to six different levels, and then the texture features are extracted using LBP variants. The extracted features obtained from the decomposed images have distinct information of the echocardiographic image. The length of significant feature vector increases with the level of decomposition. The cumulative texture features of different levels were normalized before employing them for training and testing of the classifier. In the final step, classification task has been performed using SVM and RF classifier and the performance of the CAD system is evaluated in terms of the sensitivity and specificity. The proposed CAD system is expected to assist the radiologist in improving their diagnostic performance for patients suffering from MR.

CHAPTER 6

DISCRETE WAVELET TRANSFORM BASED TEXTURE ANALYSIS OF MITRAL REGURGITATION

This chapter explores the effectiveness of discrete wavelet transform (DWT) based statistical texture features extraction techniques for the severity analysis of MR. The chapter sequentially present the concise description of the DWT, proposed DWT based texture feature extraction techniques for characterization of MR and subsequently assesses the discriminatory capability of Daubechies wavelet-based texture modeling using different classifiers.

6.1 The Discrete Wavelet Transform

The Fourier transform is an important tool to identify the frequency components of the signals by decomposing them into sine and cosine components. It can only provide spectral information about stationary signals i.e., signals whose frequency contents do not change with time. In many real-world applications, the signals are non-stationary. For non-stationary signals, the time-frequency techniques such as short-time Fourier transform (STFT), wavelet transform (WT) etc., are mostly utilized for extracting transient features of the signals. STFT utilizes a sliding window to discover spectrogram, which gives the information of both time and frequency. In STFT the length of the window limits the resolution in frequency. The wavelet transform is the solution to this issue since it depends on little wavelets with constrained length. The STFT gives a constant resolution at all frequencies, the wavelet transform uses the multi-resolution technique by which different frequencies are analyzed with different resolutions.

Transformation of signals helps in identifying distinct information which might otherwise be hidden in the original signal. Depending upon the application, the transformation technique is chosen, and each technique has its unique advantages and disadvantages. The output of the transformation represents the image in the Fourier or frequency domain, while the input image is the spatial domain equivalent. In the Fourier domain image, each point represents a particular frequency contained in the spatial domain image. Several studies focused on transform domain feature extraction techniques. The discrete cosine transform (DCT) [138], discrete wavelet transform (DWT) [139], Gabor transform [140, 141] are utilized in the classification framework. The DWT has been used here due to its multiresolution capability for analyzing images at different frequencies for several levels of resolutions [139].

The most standard wavelet decomposition utilized for image filtering is the discrete wavelet change (DWT) introduced by Mallat [139]. Wavelets are mathematical functions that decompose a signal into various frequency components, and after that concentrate on every part with a resolution coordinated to its scale. It is equivalent to bandpass filtering with a bank of constant-Q filters. The DWT has been efficiently utilized in various application of image processing tasks such as object recognition, denoising, segmentation, compression, feature extraction and image indexing [257–270].

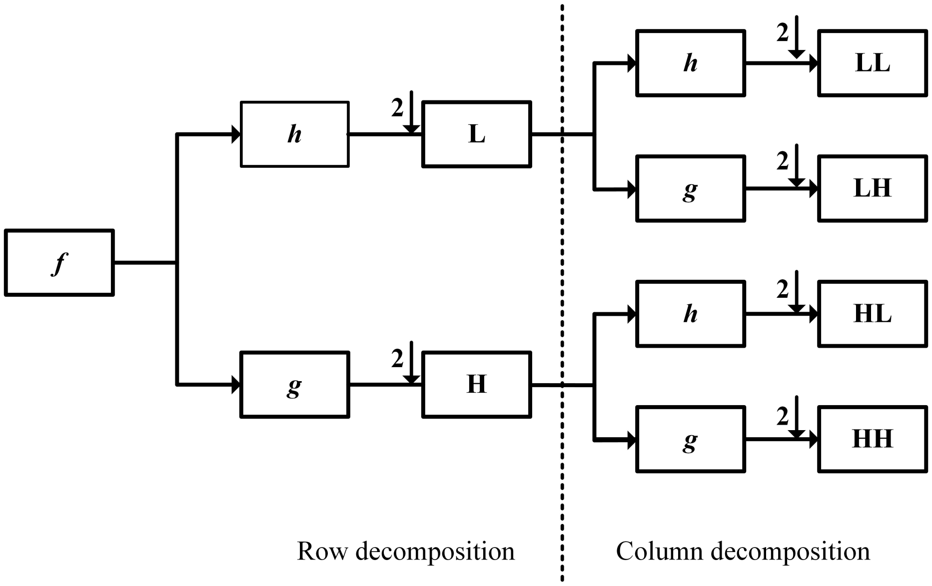

Fig. 6.1: 2D representation of the wavelet decomposition.

To perform a 2D DWT, first, a one-level, 1-D DWT is applied along the rows of the image. Second, a one-level, 1-D DWT is applied along the columns of the transformed image from the first step. The result of these two sets of operations is a transformed image with four distinct bands: (i) LL, (ii) LH, (iii) HL and (iv) HH. Here, L stands for low-pass filtering, and H stands for high-pass filtering. The LL band corresponds roughly to a down-sampled (by a factor of two) version of the original image. The LH band tends to preserve localized horizontal features, while the HL band tends to preserve localized vertical features in the original image. Finally, the HH band tends to isolate localized high-frequency point features in the image. Additional levels of decomposition can extract lower frequency features in the image; these additional levels are applied only to the LL band of the transformed image at the previous level. A one-level, 2D-DWT decomposition is depicted in Fig. 6.1.

The 2D-DWT represents an image in terms of a set of shifted and dilated wavelet functions, Ψ^{LH}, Ψ^{HL}, Ψ^{HH} and scaling functions Φ^{LL}. A *P*-scale DWT of an image $f(x, y)$ of size $N \times N$ is decomposed as:

$$f(x,y) = \sum_{q,r=0}^{N_p-1} u_{P,q,r}\phi^{LL}_{P,q,r}(x,y) + \sum_{B\in \text{ß}}\sum_{p=1}^{P}\sum_{p=1}^{N_p-1} w^{B}_{p,q,r}\psi^{B}_{p,q,r}(x,y) \tag{6.1}$$

where, $\phi^{LL}_{P,q,r}(x,y) \equiv 2^{-p}\phi(2^{-p}x - q, 2^{-p}y - r)$, $\psi^{B}_{P,q,r}(x,y) \equiv 2^{-p}\phi(2^{-p}x - q, 2^{-p}y - r)$, $B \in \text{ß}$, $\text{ß} = \{LH, HL, HH\}$, and $N_p = N/2^p$. *LH*,*HL*, and *HH* are called DWT subbands. $u_{P,q,r} = \int\int f(x,y)\phi_{p_0,q,r}dxdy$ is scaling coefficient, and $w_{p,q,r} = \int\int f(x,y)\psi^{B}_{p,q,r}dxdy$ denotes the $(q,r)^{th}$ wavelet coefficient in scale *p* and subband *B* [271]. The set of wavelet coefficients $w = \left\{w^{B}_{p,q,r} \mid p = 1, ..., P; B \in \text{ß}; q, r = 0, ..., N_p - 1\right\}$ is usually considered to contain the most important features of an image.

A compactly supported orthogonal wavelet having a pre-assigned degree of smoothness was proposed by Ingrid Daubechies [272]. It has been utilized in several image processing applications [273–276]. Psychovisual studies indicate that the human visual system processes images in a multiscale way [277]. This multiscale processing, which humans obviously apply successfully to texture perception, is a strong motivation for texture analysis methods to start from the same ideas [277–279]. Multiresolution techniques intend to transform images into a representation in which both spatial and frequency information is present. To accomplish this, a lot of related techniques were developed, including Gabor, Haar, Walsh-Hadamard expansions, Gaussian and Laplacian pyramids, subband filtering, scale space.

The multiresolution analysis capability of DWT is helpful in detecting features at a unique resolution. Daubechies wavelet family is characterized by time invariance, produces real number coefficients, and has a sharp filter transition band that is useful in minimizing the edge effects between the frequency bands. The fractal like self-symmetry property facilitates fast wavelet transform in computation, also for a given support it offers the highest number of vanishing moments [280]. Fig. 6.2 shows the Daubechies wavelet family members .

A visual illustration of the test images in A2C, A4C and PLAX views are shown in Fig. 6.3, 6.4 and 6.5.

6.2 Methodology for MR Classification using DWT based Texture Features

The procedural steps involved in present work used for the severity classification of echocardiographic images of MR is represented in the form of block schematic and is shown in Fig. 6.6. The complete classification process is explained as follow:

Step 1: In the initial step, as in the previous approach the acquired color (RGB) images are converted to grayscale image utilizing Eq. 4.5. A subjective rectangular window is then chosen which incorporates the regurgitant jet area of each picture for picking the region of interest.

Step 2: Further, the grayscale images have been decomposed to four levels (L1 to L4) utilizing the Daubechies wavelet family (db2, db4, db6, db8, and db10) as decomposition filters in the second step. The transformation of images gets significant features at a different resolution. In the present work seven texture descriptors namely first-order statistics (FOS), spatial gray level difference matrix (SGLDM), gray level difference statistics (GLDS), neighborhood gray tone difference matrix (NGTDM), statistical feature matrix (SFM), Laws textures energy measure (LTEM), and Fourier power spectrum (FPS) are used to extract the texture feature. Table 6.1 lists the proposed texture features by combining DWT with these descriptors:

Table 6.1: Proposed texture features and their notation

DWT-FOS	Discrete wavelet transform-first order statistics
DWT-SGLDM	Discrete wavelet transform spatial gray level difference matrix
DWT-GLDS	Discrete wavelet transform-gray level difference statistics
DWT-NGTDM	Discrete wavelet transform-neighborhood gray tone difference matrix
DWT-SFM	Discrete wavelet transform-statistical feature matrix
DWT-LTEM	Discrete wavelet transform-Laws textures energy measure
DWT-FPS	Discrete wavelet transform-Fourier power spectrum

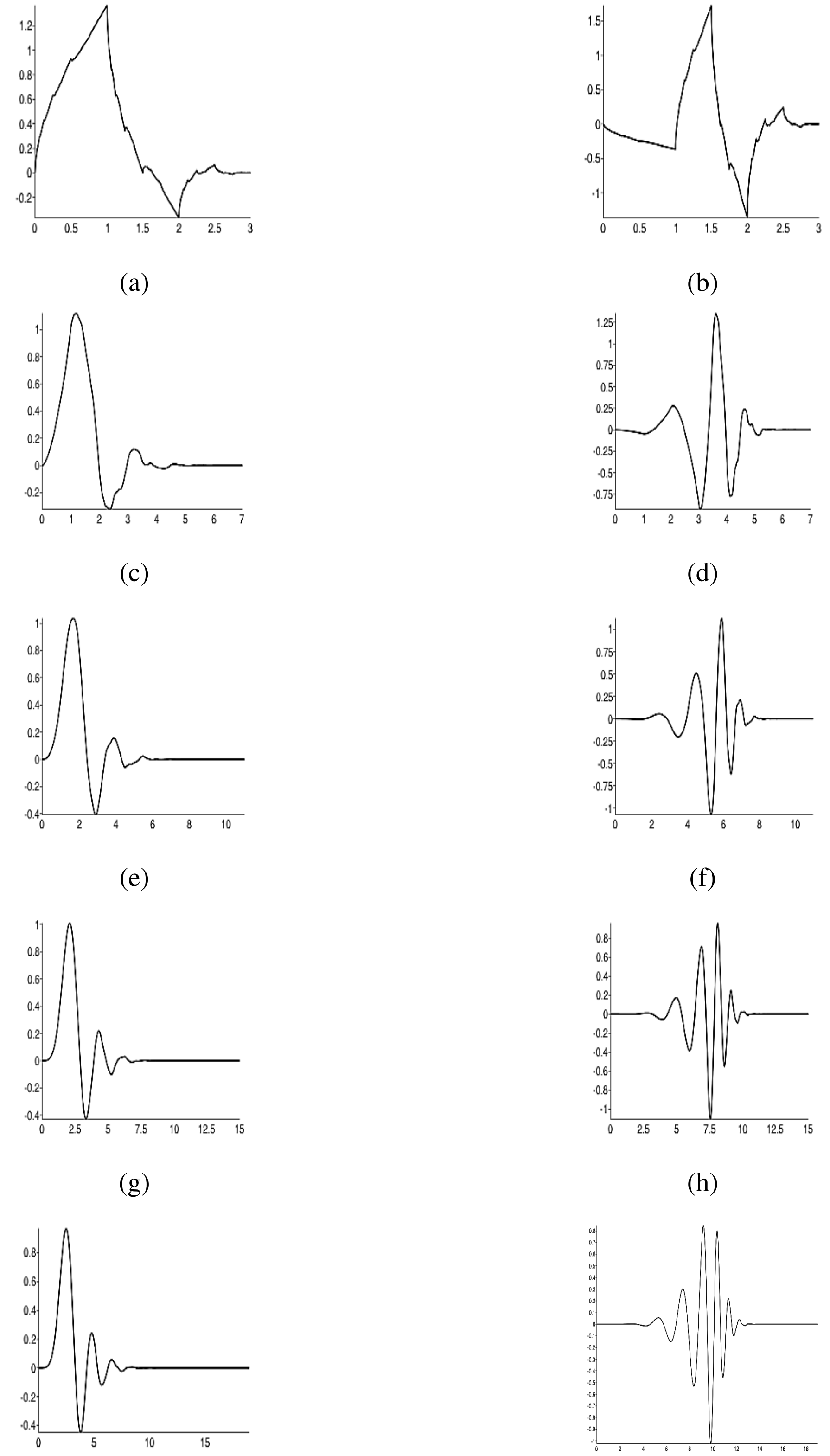

(a) (b)

(c) (d)

(e) (f)

(g) (h)

(i) (j)

Fig. 6.2: Scaling and wavelet function of Daubechies wavelet family: db2, db4, db6, db8, and db10

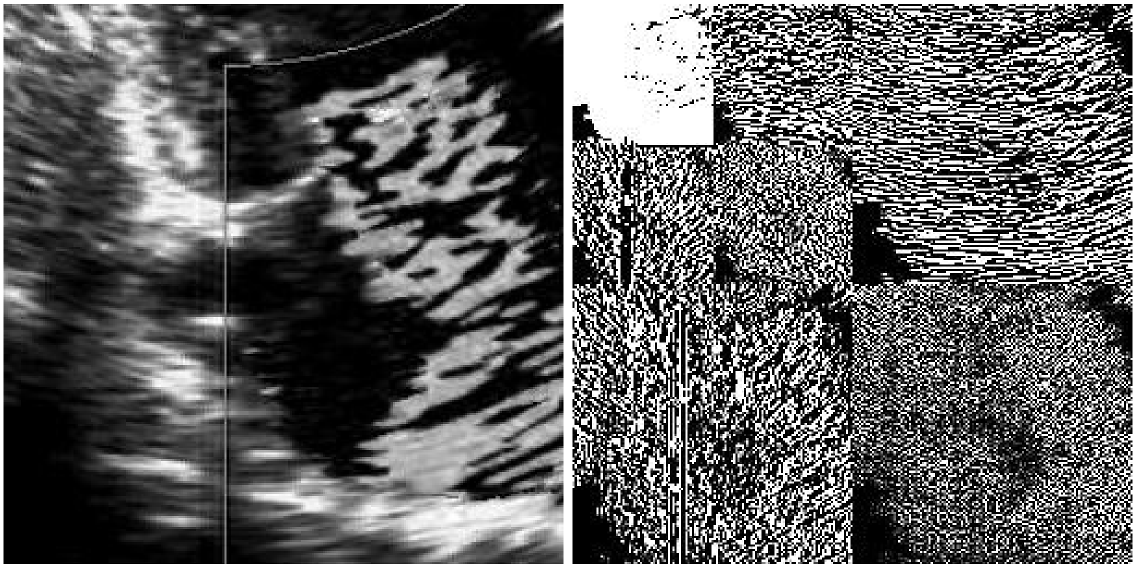
(a) (b)

Fig. 6.3: (a) The test image in A2C view (b) 2nd level of image decomposition

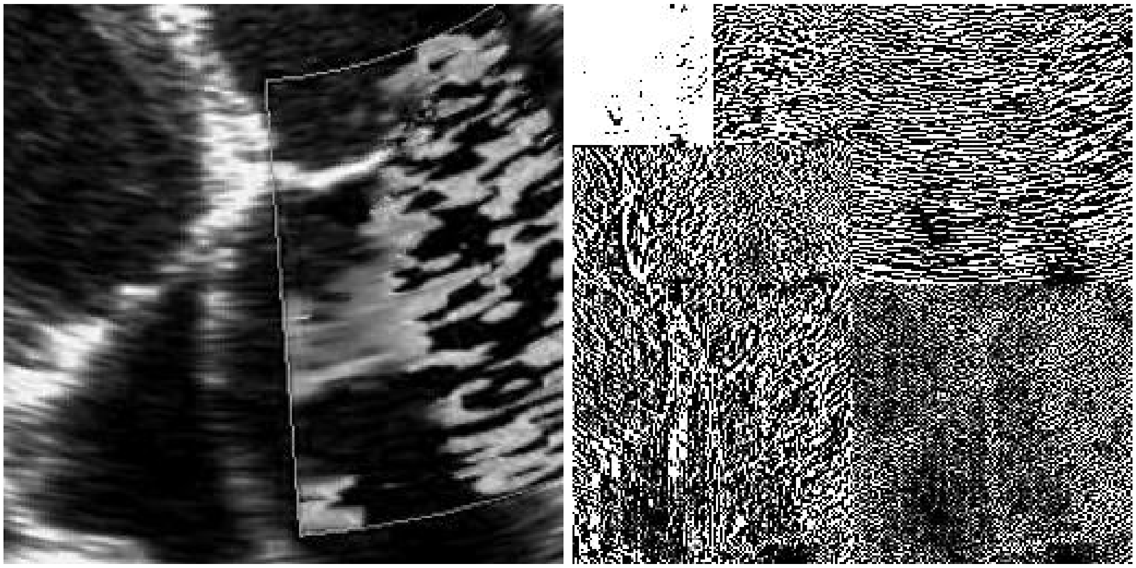
(a) (b)

Fig. 6.4: (a) The test image in A4C view (b) 2nd level of image decomposition

Step 3: As in the previous approach, here also the extracted features contain the different range of numeral values which are normalized similarly in the range of 0 to 1 before applying

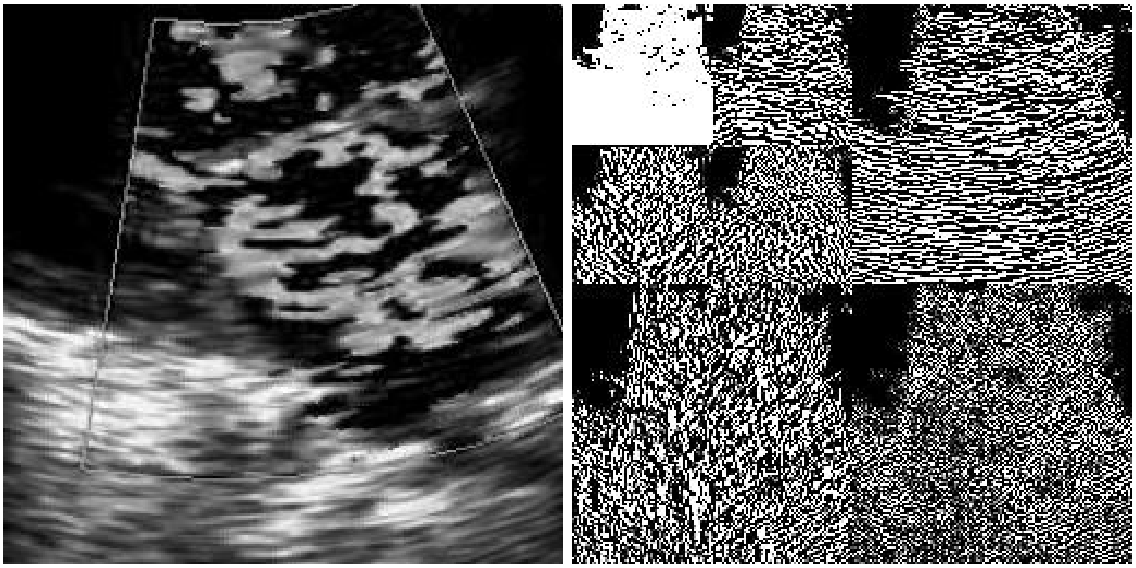
(a) (b)

Fig. 6.5: (a) The test image in PLAX view (b) 2nd level of image decomposition

to classifier utilizing Eq. 6.2.

$$n(x_i) = \frac{(x_i - m_i)}{\sigma_i} \tag{6.2}$$

where m_i and σ_i represent the mean and standard deviation of the feature *i*.

Step 4: In step 4, the extracted features are utilized for training and testing of the classifier. Here, again the RBF kernel based, SVM classifier has been utilized with 10-fold cross-validation scheme. The classification performance of the approach has been evaluated in the same manner by its classification accuracy, sensitivity, and specificity.

Step 5: The PCA and mRMR techniques are employed to reduce the dimensions of feature vector data.

Step 6: Finally, the severity classification has been done in three views, further the multi-voting examination is performed to get an ultimate choice.

6.3 DWT based Texture Feature Extraction

The texture is laid out as local neighborhood properties of the gray levels of an image. Multiresolution methods expect to rebuild images into a representation where spatial and frequency information is available at the same time. In the present work seven texture feature descriptors, named as, FOS, SGLDM, GLDS, NGTDM, SFM, TEM, and FPS have been uti-

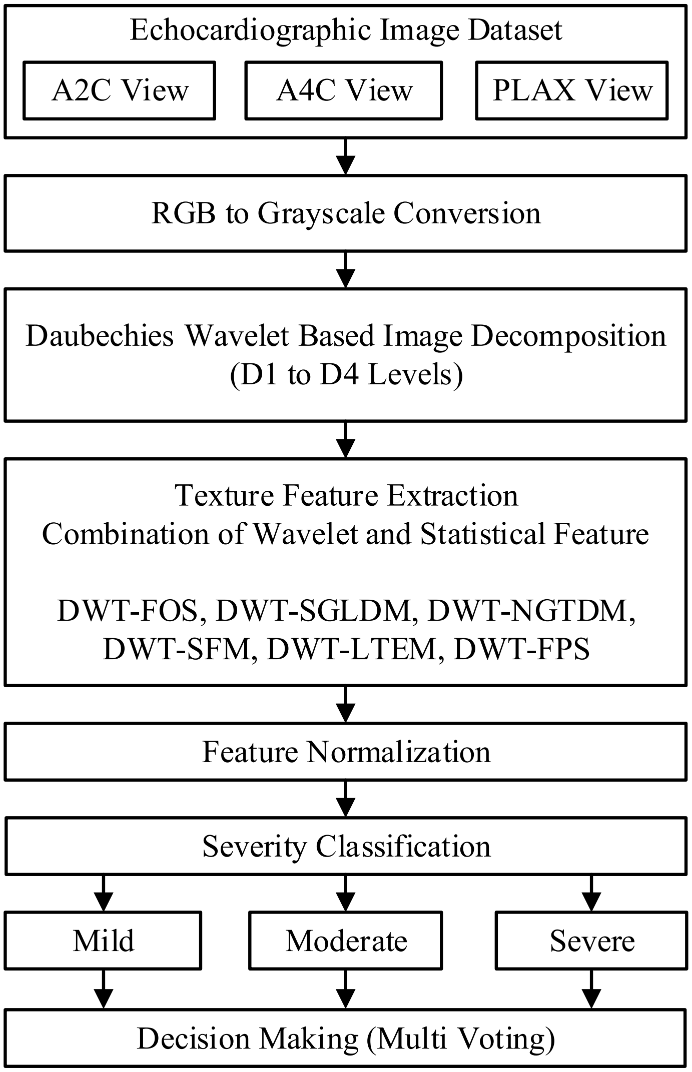

Fig. 6.6: Schematic representation of proposed CAD system

lized after the decomposition of the image up to various levels. The detail of these texture feature extraction techniques are already given in Section 4.4. The computational requirement of the classifier increases with the dimension of the features and the classification accuracy may not be improved due to high dimension features. The purpose of feature reduction is to retain the best subset of all features. Two methods have been compared here for the reduction of feature vector dimension, one is principal component analysis (PCA) [151] and second, is minimal redundancy maximum relevance (mRMR) [159].

6.4 Classification

In the present work, the performance of the proposed CAD system using the proposed texture feature extraction techniques have been evaluated using a supervised classifiers i.e. support vector machine (SVM) [220, 221]. The details and tuning parameters of SVM classifier have been discussed in Section 4.6.1. To maintain unbiasness 10-fold cross-validation has been used. The detail of cross-validation has been given in Section 4.6.3. The diagnostic performance of a CAD system is evaluated using sensitivity and specificity, as explained in Section 4.6.4.

6.5 Experimental Results and Discussions

This experimentation was performed with an objective to investigate the performance of DWT based statistical texture features, (for example, FOS, SGLDM, GLDS, NGTDM, SFM, TEM, and FPS) for the severity analysis of MR in three views i.e. A2C, A4C, and PLAX. In this work, Daubechies family members to be specific, db2, db4, db6, db8, db10 have been employed to decompose the MR images up to four level. The RBF kernel SVM classifiers have been examined by using MATLAB implementation of LIBSVM [221]. A few trials have been directed for feature efficacy analysis on MR image dataset. The 10-fold cross-validation approach has been utilized to diminish the biasness. To complete the above-mentioned task, all the experiments are performed on the computer having Intel (R) Core (TM), i7-2600 CPU@3.40 GHz processor and 16 GB RAM. The percentage classification accuracy computed by these features are presented in Tables 6.2, 6.3, and 6.4 for A2C, A4C, and PLAX views, respectively.

6.5.1 Performance Evaluation of DWT based Texture Features in A2C Views

The classification accuracies computed by DWT based texture features on MR images in A2C views are shown in Table 6.2. Among all, the DWT-SGLDM provides the highest accuracy of 96.98±0.84 at the second level of image decomposition using db8 with texture feature vector dimension of 208. In addition, the second best classification accuracy of 96.82±1.10 (32 features) has been achieved at the second level of image decomposition using db6 for DWT-SFM features, while features computed from DWT-FPS provides least classification accuracy of 84.96± 1.08 (16 features) at the second level of image decomposition using db10. In order

Table 6.2: The classification accuracies obtained using DWT based texture features in A2C view with RBF kernel SVM classifier

Features	IDL	NoF	db2	db4	db6	db8	db10
DWT-FOS	1	20	90.41 ± 1.17	95.08 ± 0.86	93.36 ± 1.28	95.66 ± 1.16	92.20 ± 1.13
	2	40	94.22 ± 1.28	93.06 ± 0.76	91.06 ± 1.72	96.24 ± 1.05	94.52 ± 1.16
	3	60	89.60 ± 1.82	90.46 ± 1.03	90.19 ± 2.61	93.35 ± 1.04	94.79 ± 1.34
	4	80	86.43 ± 1.68	88.42 ± 1.55	88.14 ± 1.22	91.02 ± 1.25	93.04 ± 1.07
DWT-SGLDM	1	104	95.97 ± 1.37	95.96 ± 1.62	95.69 ± 1.66	95.96 ± 1.06	96.25 ± 1.13
	2	208	95.94 ± 0.98	96.26 ± 1.05	95.67 ± 1.30	96.98 ± 0.84	96.25 ± 0.75
	3	312	94.80 ± 1.41	95.66 ± 0.65	94.81 ± 1.35	97.68 ± 0.85	95.66 ± 1.30
	4	416	92.48 ± 1.88	93.07 ± 0.86	93.65 ± 1.18	97.11 ± 0.74	94.24 ± 1.47
DWT-GLDS	1	16	82.31 ± 1.86	87.26 ± 1.31	87.29 ± 1.95	89.28 ± 1.13	83.20 ± 1.41
	2	32	89.00 ± 0.92	92.45 ± 1.17	87.23 ± 1.91	90.44 ± 1.23	90.72 ± 1.13
	3	48	86.13 ± 2.16	89.87 ± 1.99	82.61 ± 2.02	86.67 ± 1.99	87.57 ± 1.94
	4	64	82.12 ± 2.44	86.42 ± 1.93	84.41 ± 2.81	83.80 ± 1.42	87.25 ± 1.67
DWT-NGTDM	1	20	91.59 ± 1.33	92.78 ± 1.31	91.28 ± 1.57	92.47 ± 1.38	87.88 ± 2.29
	2	40	93.06 ± 0.76	94.51 ± 0.79	93.65 ± 1.53	96.52 ± 0.84	93.65 ± 0.93
	3	60	93.91 ± 0.92	93.36 ± 1.20	91.06 ± 2.07	94.49 ± 1.11	94.53 ± 1.56
	4	100	89.29 ± 1.81	91.92 ± 1.64	91.91 ± 1.39	94.52 ± 0.78	93.65 ± 1.11
DWT-SFM	1	16	90.50 ± 2.62	93.36 ± 1.59	93.05 ± 1.31	94.81 ± 1.02	91.91 ± 1.11
	2	32	94.23 ± 1.05	96.82 ± 0.81	96.82 ± 1.10	95.95 ± 0.88	96.80 ± 0.82
	3	48	91.92 ± 1.26	93.92 ± 1.31	91.33 ± 1.04	95.65 ± 0.49	94.81 ± 0.82
	4	64	93.08 ± 1.62	93.66 ± 0.92	92.21 ± 1.53	94.20 ± 0.75	95.09 ± 0.95
DWT-TEM	1	24	92.21 ± 1.70	95.66 ± 0.98	93.64 ± 0.82	93.92 ± 1.81	94.23 ± 1.28
	2	48	95.65 ± 1.17	94.80 ± 0.71	93.64 ± 0.71	94.78 ± 1.14	93.33 ± 1.38
	3	72	92.77 ± 1.51	92.48 ± 1.07	91.92 ± 1.75	88.12 ± 1.24	92.74 ± 1.45
	4	96	92.21 ± 1.67	89.87 ± 1.57	91.05 ± 1.15	91.06 ± 1.49	90.74 ± 1.53
DWT-FPS	1	8	74.50 ± 2.43	74.50 ± 2.84	74.53 ± 1.82	70.75 ± 1.26	73.39 ± 2.09
	2	16	84.64 ± 1.83	79.42 ± 1.99	77.72 ± 1.49	79.75 ± 2.39	84.96 ± 1.08
	3	24	81.44 ± 2.09	77.93 ± 2.37	79.45 ± 1.70	83.51 ± 2.14	81.15 ± 1.01
	4	32	77.68 ± 1.05	74.17 ± 2.97	76.30 ± 1.92	78.85 ± 2.43	79.99 ± 1.42
ALL	1	208	98.84 ± 0.47	98.55 ± 0.48	96.54 ± 2.71	97.98 ± 0.74	97.13 ± 0.95
	2	416	99.12 ± 0.44	97.41 ± 0.66	97.69 ± 0.83	97.96 ± 0.87	97.99 ± 0.61
	3	624	95.94 ± 1.32	97.40 ± 0.51	96.54 ± 0.93	97.97 ± 0.75	97.11 ± 0.95
	4	832	95.37 ± 0.97	96.55 ± 1.19	95.10 ± 1.13	97.98 ± 0.61	96.84 ± 1.08

IDL: Image decomposition level, NoF: Number of features

Table 6.3: The classification accuracies obtained using DWT based texture features in A4C view with RBF kernel SVM classifier

Features	IDL	NoF	db2	db4	db6	db8	db10
DWT-FOS	1	20	91.29 ± 1.72	91.87 ± 1.37	87.25 ± 1.62	92.75 ± 1.16	87.55 ± 1.91
	2	40	95.66 ± 0.98	95.66 ± 1.16	94.20 ± 0.98	95.63 ± 1.46	94.82 ± 1.19
	3	60	91.61 ± 1.58	93.08 ± 1.21	90.16 ± 2.02	87.24 ± 2.14	89.61 ± 1.66
	4	80	86.95 ± 1.84	91.05 ± 1.15	87.85 ± 2.29	84.66 ± 2.08	88.73 ± 1.22
DWT-SGLDM	1	104	97.37 ± 0.69	94.50 ± 1.01	94.50 ± 1.01	97.10 ± 0.75	92.18 ± 1.45
	2	208	98.86 ± 0.63	98.56 ± 0.77	95.66 ± 1.31	98.00 ± 1.21	98.28 ± 0.63
	3	312	97.98 ± 0.75	96.55 ± 0.94	94.82 ± 1.33	94.81 ± 1.20	95.36 ± 1.00
	4	416	95.94 ± 1.36	94.22 ± 1.74	91.89 ± 1.13	91.90 ± 1.20	95.37 ± 0.78
DWT-GLDS	1	16	88.42 ± 2.34	86.98 ± 1.42	87.53 ± 1.75	88.10 ± 2.12	83.45 ± 1.27
	2	32	94.17 ± 1.31	92.18 ± 1.35	89.88 ± 1.56	91.91 ± 1.85	91.61 ± 1.59
	3	48	88.40 ± 1.43	87.85 ± 2.43	86.99 ± 2.45	90.16 ± 1.58	84.94 ± 1.72
	4	64	82.07 ± 1.36	87.27 ± 1.68	83.50 ± 1.85	84.91 ± 2.26	82.61 ± 1.63
DWT-NGTDM	1	20	91.01 ± 1.26	88.10 ± 1.61	90.15 ± 2.04	90.99 ± 1.73	84.06 ± 1.52
	2	40	95.64 ± 1.25	94.48 ± 1.33	92.74 ± 1.58	96.22 ± 1.24	94.49 ± 1.26
	3	60	92.43 ± 1.71	93.07 ± 1.48	91.34 ± 1.76	91.29 ± 2.02	91.87 ± 1.51
	4	100	89.87 ± 1.30	90.16 ± 1.62	91.92 ± 1.90	88.70 ± 1.84	92.18 ± 1.58
DWT-SFM	1	16	92.45 ± 1.32	91.55 ± 1.67	90.97 ± 2.04	92.70 ± 1.88	88.97 ± 2.56
	2	32	94.22 ± 2.02	94.78 ± 1.42	93.06 ± 2.45	96.82 ± 1.01	95.65 ± 1.17
	3	48	91.30 ± 1.69	90.75 ± 0.92	93.34 ± 1.50	95.11 ± 1.05	94.47 ± 1.48
	4	64	88.70 ± 2.05	93.66 ± 1.34	94.25 ± 1.70	92.20 ± 1.28	93.61 ± 1.36
DWT-TEM	1	24	90.73 ± 1.35	89.61 ± 2.45	88.40 ± 1.49	91.60 ± 1.10	90.72 ± 1.49
	2	48	93.90 ± 1.02	91.31 ± 1.54	92.48 ± 2.51	95.68 ± 1.29	93.08 ± 2.14
	3	72	89.58 ± 1.29	88.16 ± 2.06	89.30 ± 1.41	91.31 ± 1.68	91.33 ± 1.88
	4	96	88.15 ± 2.20	84.39 ± 2.42	88.13 ± 2.07	88.12 ± 1.53	90.72 ± 2.16
DWT-FPS	1	8	79.71 ± 1.30	70.76 ± 1.57	69.85 ± 2.17	71.91 ± 2.55	71.92 ± 2.54
	2	16	88.15 ± 1.82	89.89 ± 2.13	83.78 ± 2.82	82.91 ± 1.67	82.34 ± 1.88
	3	24	87.85 ± 1.58	86.95 ± 1.39	82.31 ± 2.45	77.41 ± 2.44	79.41 ± 1.19
	4	32	81.71 ± 2.40	83.45 ± 2.15	81.13 ± 2.92	77.70 ± 2.54	79.74 ± 1.68
ALL	1	208	98.26 ± 0.63	98.25 ± 0.47	98.84 ± 0.47	99.41 ± 0.39	98.84 ± 0.63
	2	416	99.13 ± 0.44	99.70 ± 0.29	98.84 ± 0.63	99.70 ± 0.29	99.42 ± 0.38
	3	624	97.96 ± 0.97	98.55 ± 0.77	98.84 ± 0.64	98.84 ± 0.63	97.68 ± 1.12
	4	832	95.93 ± 1.32	97.98 ± 0.61	96.24 ± 0.95	96.51 ± 0.95	97.68 ± 1.12

IDL: Image decomposition level, NoF: Number of features

Table 6.4: The classification accuracies obtained using DWT based texture features in PLAX view with RBF kernel SVM classifier

Features	IDL	NoF	db2	db4	db6	db8	db10
DWT-FOS	1	20	81.45 ± 1.79	86.97 ± 1.45	80.56 ± 1.46	82.90 ± 1.76	80.88 ± 2.11
	2	40	86.97 ± 1.93	86.10 ± 1.64	84.92 ± 1.88	87.55 ± 1.60	87.28 ± 2.10
	3	60	82.61 ± 2.54	83.80 ± 1.40	85.83 ± 1.94	79.17 ± 1.61	86.41 ± 2.17
	4	80	80.26 ± 1.57	80.59 ± 1.6	80.04 ± 1.90	76.82 ± 2.20	82.04 ± 1.52
DWT-SGLDM	1	104	89.27 ± 1.64	94.79 ± 0.84	93.05 ± 1.64	92.17 ± 1.44	90.75 ± 1.60
	2	208	92.15 ± 0.78	93.64 ± 1.28	92.78 ± 0.97	90.48 ± 2.43	92.75 ± 1.32
	3	312	86.96 ± 1.49	87.82 ± 1.43	88.41 ± 1.56	87.58 ± 2.29	89.27 ± 0.99
	4	416	85.76 ± 1.49	84.37 ± 1.88	88.08 ± 1.29	89.03 ± 2.12	92.44 ± 1.18
DWT-GLDS	1	16	82.88 ± 2.21	87.86 ± 1.52	86.38 ± 1.62	86.65 ± 1.40	83.76 ± 1.51
	2	32	82.29 ± 2.3	85.27 ± 1.95	83.76 ± 1.51	83.51 ± 1.90	83.17 ± 2.00
	3	48	77.35 ± 2.33	84.64 ± 1.50	79.14 ± 1.41	80.03 ± 2.59	81.15 ± 1.60
	4	64	74.41 ± 2.79	79.43 ± 1.84	76.50 ± 1.61	77.37 ± 2.04	82.31 ± 1.01
DWT-NGTDM	1	20	87.83 ± 2.00	91.29 ± 0.88	86.68 ± 1.30	83.51 ± 2.11	80.34 ± 1.85
	2	40	89.24 ± 1.76	90.71 ± 1.98	88.13 ± 1.24	88.13 ± 1.94	86.67 ± 1.69
	3	60	84.94 ± 1.85	86.96 ± 2.71	84.08 ± 1.94	87.56 ± 1.86	86.39 ± 1.20
	4	100	85.22 ± 2.23	83.74 ± 2.97	82.59 ± 1.58	86.42 ± 1.79	86.13 ± 1.62
DWT-SFM	1	16	90.48 ± 2.04	87.54 ± 2.16	88.12 ± 2.52	89.85 ± 0.99	89.86 ± 1.24
	2	32	88.39 ± 1.07	93.64 ± 1.41	91.02 ± 1.45	92.19 ± 2.06	94.24 ± 1.27
	3	48	86.66 ± 1.68	92.76 ± 1.30	89.27 ± 1.94	91.03 ± 1.52	92.48 ± 1.49
	4	64	86.32 ± 2.12	91.60 ± 1.46	90.16 ± 1.13	90.72 ± 1.93	92.78 ± 1.43
DWT-TEM	1	24	88.11 ± 1.02	89.85 ± 1.32	90.43 ± 0.87	89.24 ± 1.52	88.42 ± 2.41
	2	48	91.89 ± 1.12	89.26 ± 1.16	89.84 ± 1.52	90.41 ± 1.63	88.39 ± 1.85
	3	72	86.41 ± 1.46	84.90 ± 1.38	86.64 ± 1.27	87.77 ± 1.53	85.25 ± 2.09
	4	96	83.74 ± 1.89	80.28 ± 1.45	85.52 ± 1.35	85.18 ± 1.82	85.55 ± 1.89
DWT-FPS	1	8	70.68 ± 2.15	68.14 ± 1.82	64.12 ± 1.65	71.29 ± 2.97	68.39 ± 1.19
	2	16	74.16 ± 2.52	71.59 ± 2.4	69.04 ± 2.05	71.34 ± 2.48	73.66 ± 1.62
	3	24	71.83 ± 2.58	71.97 ± 2.77	67.83 ± 2.94	69.30 ± 2.33	75.13 ± 2.02
	4	32	70.65 ± 3.09	68.40 ± 1.59	70.50 ± 2.99	68.16 ± 2.87	71.91 ± 2.04
ALL	1	208	93.59 ± 1.49	97.68 ± 1.04	96.82 ± 1.00	96.82 ± 1.24	95.35 ± 0.98
	2	416	95.36 ± 0.64	96.24 ± 0.97	95.95 ± 0.76	95.38 ± 1.77	97.10 ± 0.86
	3	624	91.29 ± 1.15	92.46 ± 1.58	92.75 ± 1.52	92.76 ± 1.55	93.89 ± 1.19
	4	832	89.23 ± 1.51	90.17 ± 1.61	92.4 3± 1.24	90.74 ± 1.68	94.21 ± 0.95

IDL: Image decomposition level, NoF: Number of features

to improve the accuracy of the classification system, combination of all features at different decomposition level has been investigated, and significant improvement in classification accuracy has been found. The classification accuracy of 99.12±0.44 has been achieved at the second level of image decomposition using db2 with a total feature vector dimension of 416.

6.5.2 Performance Evaluation of DWT based Texture Features in A4C Views

In a similar fashion, the performance of texture features in A4C views has been represented in Table 6.3. Among all, DWT-SGLDM provides the highest accuracy of 98.86±0.63 at the second level of image decomposition using db2 with a feature vector length of 208. The second best classification accuracy of 96.82±1.01 has been achieved at the second level of image decomposition using db8 (32 features) for DWT-SFM features, while features computed from DWT-FPS provides least classification accuracy of 89.89±2.13 at the second level of image decomposition using db4 (16 features). Further, to improve the accuracy of system individual features are combined and considered for analysis. Hence, it is found that all texture feature have produced the noticeable improvement in classification accuracy of 99.70±0.29 using a feature vector length of 416 at the second level of image decomposition using db4 and db8 instead of using texture features of one class individually.

6.5.3 Performance Evaluation of DWT based Texture Features in PLAX Views

In this section, the classification accuracies for PLAX view has been investigated by texture features as mentioned in Section 6.3. The percentage of classification accuracy obtained using texture features in PLAX views are presented in Table 6.4. In this case, also texture feature computed from DWT-SGLDM produced the best accuracy having a value of 94.79±0.84 at first level of image decomposition using db4 with feature vector length of 104, and least classification accuracy was computed from DWT-FPS features having the value of 75.13±2.02 at the third level of image decomposition using db10 with 24 features. In a similar manner, the analysis is continued and all texture features are concatenated to investigate the classification accuracy of the system. In this case, also all texture features achieved the remarkable classification accuracy having a value of 97.68±1.04 at first level of image decomposition using db4 with a feature vector length of 204 compared to using texture features of one class individually.

6.5.4 Performance Evaluation of CAD System after Feature Reduction and Selection

In order to improve the performance of the CAD system the PCA has been used for feature reduction and mRMR scheme has been utilized for feature selection. From the Tables 6.2 - 6.4, it has been found that highest classification accuracy of 99.12±0.44 has been achieved at the second level of image decomposition using db2 in the A2C view using a total of 416 features. In A4C view, the highest classification accuracy of 99.70±0.29 has been achieved at the second level of image decomposition using db4 and db8 using a total of 416 features while the classification accuracy having a value of 97.68±1.04 at the first level of image decomposition using db4 has been achieved in PLAX view using 208 features. The classification performance with reduced features is given in Table 6.5.

Table 6.5: Classification accuracy using feature reduction and selection

	A2C		A4C		PLAX	
NoF	PCA	mRMR	PCA	mRMR	PCA	mRMR
10	82.30±1.91	85.82±1.97	74.45±1.28	90.11±1.59	84.92±1.82	80.93±2.92
20	84.33±1.73	92.76±1.22	78.83±1.31	96.52±1.03	90.71±1.49	91.01±1.00
50	95.36±1.15	96.25±1.21	94.75±1.50	97.39±0.51	95.65±1.07	95.64±1.34
75	97.10±0.74	97.38±0.81	99.12±0.62	98.55±0.48	97.39±0.91	96.53±1.26
100	98.26±0.63	97.39±0.67	99.70±0.29	98.84±0.47	97.68±0.72	96.52±1.20
125	98.84±0.47	99.12±0.44	99.70±0.29	98.56±0.64	97.97±0.75	96.80±1.33
150	98.84±0.47	98.84±0.47	99.42±0.38	98.56±0.64	97.97±0.75	97.39±1.00
175	98.84±0.47	98.84±0.47	99.42±0.38	98.56±0.64	97.68±0.83	97.96±0.75
200	98.84±0.47	98.84±0.47	99.42±0.38	98.56±0.64	97.68±1.04	97.68±1.04

The mRMR technique gives the highest classification accuracy of 99.12±0.44 by using 125 best features compared to PCA reduction technique which gave this accuracy at 225 features in A2C view. After this as the number of features increases the variation in the classification accuracy didn't improve significantly. In A4C view, the PCA reduced feature vector data has attained the highest accuracy of 99.70±0.29 using 100 best features compared to mRMR feature reduction and selection method where the classification accuracy having value 98.84±0.47. Similarly, in PLAX view 97.97±0.75 accuracies has been achieved using PCA reduced feature vector of length 125 while mRMR feature selection method gave 97.96±0.75 with 175 best features. It is seen that the mRMR technique gives better results for feature dimensionality reduction compared to PCA technique.

Table 6.6: Performance of one-versus-rest SVMs classifier in three views.

	Confusion matrix			Statistical parameters	
	Predicted			Sensitivity	Specificity
Actual	Mild	Moderate	Severe		
A2C View					
Mild	139	1	0	99.28	99.02
Moderate	1	139	0	99.28	99.51
Severe	1	0	64	98.46	100.00
A4C View					
Mild	158	1	1	98.75	100.00
Moderate	0	115	0	100.00	99.13
Severe	0	1	69	98.57	99.63
PLAX View					
Mild	152	3	0	98.60	97.89
Moderate	2	102	1	97.14	98.75
Severe	2	0	83	97.75	99.61

6.5.5 Diagnostic Test Evaluation of Proposed CAD System

The diagnostic ability of classification system is evaluated in terms of sensitivity and specificity. The confusion matrix of the order of 3×3 is created and the performance parameter sensitivity and specificity has been calculated in all three views. Table 6.6 shows the classification performance of the CAD system. In A2C view, the confusion matrix shows that there is only one misclassification in all three classes. The highest sensitivity calculated is 99.28 % in the mild and moderate class and highest specificity is 100 % for severe class. In A4C view, two misclassifications are reported in mild and one in severe class while for a moderate class there was no misclassification. The sensitivity and specificity of 100 % calculated in moderate and mild class respectively. Similarly, in PLAX view, three misclassifications were reported in mild and moderate class and two in severe class. The highest sensitivity achieved has 98.6 % in mild and specificity of 99.61 % has been achieved in the severe category.

6.6 Summary

In this chapter, a CAD system has been presented for the severity classification of MR using the DWT based statistical texture features. Here, Daubechies wavelet family has been utilized for the image decomposition. The texture features have been extracted up to four level image decomposition. The resultant DWT sub-images coefficients obtained using proposed approach are distinct at each level and contain valuable information. Extracting the features from all levels (L1-L4) have increased the number of significant features. Combining these extracted features generate significant feature vector useful in severity analysis of MR. Seven statistical features have been extracted from DWT subbands and these features are used for the training and testing of the SVM classifiers.

The analysis of the results obtained with 10-fold cross-validation approach revealed that the proposed approach generates the most discriminative texture features. The best classification accuracy of 99.12 ± 0.44, 99.70 ± 0.29 and 97.68 ± 1.04 has been achieved in A2C, A4C, and PLAX views respectively. The db2 and db4 wavelet performed well among all the family members. Furthermore, incorporating the feature reduction method, PCA, and feature selection method, mRMR, it has been seen that the reduced feature vector set provides the equivalent classification accuracy at reduced feature vector size. This reduces the computational cost of the proposed scheme. The experimental results indicate that the proposed texture methods can successfully classify the three classes of MR, namely, mild, moderate and severe. The proposed approach for the severity classification of MR has been validated with the accuracy, sensitivity, and the specificity of the CAD system.

CHAPTER 7

CONCLUSIONS AND FUTURE SCOPE

7.1 Conclusions

This research work has been carried out to analyze mitral regurgitation (MR) using echocardiographic images. The emphasis has been given to the design and development of some suitable texture feature extraction techniques for the classification of MR images into three categories. The effectiveness of the proposed techniques has been investigated on the MR image database collected from the Department of Cardiology, Swami Rama Himalayan University, Dehradun, India. This database has 1035 ultrasound images in three views i.e. A2C, A4C, and PLAX.

A comparative study of despeckling filters of five categories such as local adaptive, synthetic aperture radar (SAR), anisotropic diffusion, non-local mean, and fuzzy filters have been performed on test images and TTE images. A novel speckle reduction technique based on the linear combination of homomorphic fuzzy (HF) filter with NLM filter has been proposed and analyzed for TTE images of MR.

To accomplish the classification task efficiently, various texture feature extraction techniques have been employed to build the simple and computationally efficient texture features. Furthermore, these feature vector data has been normalized in the range 0 to 1, to give equal weight to all the features, before applying them as input to the classifiers.

The feature extraction techniques have produced a large number of complex features that affect the classification accuracy and computational time. To overcome this limitation, a feature selection technique minimum redundancy maximum relevance (mRMR) and feature dimensionality reduction technique i.e., principal component analysis (PCA) have been employed to reduce the feature vector data dimension. Further, to enhance the classification accuracy, two widely used classification algorithms SVM with three kernels (linear, polynomial, and RBF), and RF classifiers have been employed. In order to remove biasing in the classification, 10-fold and leave-one-out cross-validation technique have been adopted. The best combination of the multiresolution feature extraction technique and classification algorithm has been selected based upon the maximum classification accuracy achieved by them.

Based upon the experimental outcomes, based on the above work background distinct conclusions have been drawn from the present work, which are summarized in the following subsections:

7.1.1 Performance of Hybrid Fuzzy Filter for Speckle Noise Reduction

A comparative study of despeckling filters of five categories such as local adaptive, synthetic aperture radar (SAR), anisotropic diffusion, non-local mean, and fuzzy filters have been implemented on test images and TTE images. The despeckling capabilities of these filters have been evaluated in terms of traditional image quality metrics as well as blind image quality metrics such as peak signal to noise ratio (PSNR), mean square error (MSE), speckle suppression and mean preservation index (SMPI), structural content (SC), normalized error summation (Err3, Err4), Laplacian mean square error (LMSE), normalized correlation coefficient (NCC), figure of merit (FoM), beta metric (β), speckle suppression index (SSI), image quality index (IQI), structural similarity index (SSIM), and signal to noise ratio (SNR). It is observed that the performance of nonlocal mean filter (NLM) filter is superior in terms of edge preservation compared to speckle reduction anisotropic diffusion (SRAD) filter, while the fuzzy filters have a better FoM in comparison to anisotropic diffusion filters. Hence, a hybrid fuzzy filter (HFF), combining the advantages of NLM and fuzzy filters, has been proposed in the presented work. The denoising performance parameters of the hybrid fuzzy filter have been compared with despeckling techniques in the homomorphic and non-homomorphic domain. The proposed hybrid fuzzy filter performed better in terms of edge preservation compared to other fuzzy filters.

7.1.2 Performance of Spatial Domain Texture Feature Extraction Techniques

A CAD system has been proposed for the classification of the severity of MR images based on the texture features of the regurgitant area and two classifiers SVM with different kernel functions and RF. A comparative study has been done to evaluate the effect of the color space in the classification system. The *RGB* space color Doppler images are converted to different color spaces such as *YCbCr* (Luminance-Chrominance), *CMY* (Cyan Magenta Yellow), *L*A*B**, Grayscale. A total of 56 texture features have been extracted from the ultrasound images of MR patients and fed as input to the classifiers. The individual classification accuracy of each component of color spaces have been compared and it has been observed that the classification accuracy obtained using *RGB* color space has been found higher than the accuracy obtained by using grayscale images. The average deviation calculated is less than 0.5 between two classification accuracies using *RGB* color and grayscale images. However, the time required for the texture feature extraction using color spaces is triple to the time required for grayscale image data set. Hence, in order to reduce the computation time further analysis of the CAD system is done utilizing grayscale images throughout in this work. The RBF kernel-based SVM classifier performed best with all the extracted texture features compared to others.

Further, to improve the performance of CAD system the features have been ranked by their correlation to the target vector. The mRMR feature reduction method exhibited that the top 30 texture features are sufficient to classify the three classes of MR images. The classification accuracies of 95.65 %, 95.65 %, and 95.36 % has been achieved in A2C, A4C and PLAX views, respectively utilizing all features. The 100 % sensitivity and specificity have been achieved in mild and severe class, in PLAX view.

7.1.3 Performance of GP Based Texture Feature Extraction Techniques

Here the multiresolution capability of Gaussian pyramid structure has been used. The proposed methodology consists of three basic steps. In the first step, the images are converted to a grayscale image and a region of interest is selected through an arbitrary method. In the second step, the GP structure is used as a multiresolution scheme to decompose images up to six different levels, and then the texture features are extracted using LBP variants. The proposed texture features are named as GPLBP^{u2}, GPLBP^{ri}, GPLBP^{riu2}, GPCSLBP, GPLBP-HF, and GPCLBP . The extracted features obtained from the decomposed images have distinct information affiliated to the original image. The length of significant feature vector increases with the level of decomposition. The cumulative texture features of different levels have then been normalized before applying them for training and testing the classifier. In the final step, classification task has been performed using SVM and RF classifier and the performance of the CAD system has been evaluated in terms of the sensitivity and specificity.

The highest classification accuracies have been achieved using the proposed GPCLBP feature at the sixth level in all three views. The achieved classification accuracies are 95.66 ± 0.98, 94.47 ± 1.91 and 94.21 ± 1.31 at the fifth level of decomposition of A2C and A4C view and at the sixth level of PLAX view, respectively using the RBF kernel SVM classifier. Here also the performance of RBF kernel was better than other two. It has been verified by the experimental results that the classification performance of the existing LBP variants has been improved significantly by the proposed scheme.

7.1.4 Performance of DWT Based Texture Feature Extraction Techniques

Here, the effectiveness of DWT based statistical texture feature extraction techniques have been evaluated for the severity analysis of MR and subsequently the discriminatory capability of Daubechies wavelet-based texture modeling using different classifiers have been assessed. This has been accomplished using DWT based statistical features extracted from MR image dataset in three views with SVM classifiers. The proposed features are named as DWT-FOS, DWT-SGLDM, DWT-GLDS, DWT-NGTDM, DWT-SFM, DWT-TEM, DWT-FPS. Combining many features is a preferred technique usually utilized for improving the classification performance of a CAD system. Thus, the combination of all extracted features has been used as the final feature vector. Furthermore, it has been observed that incorporating the feature reduction method, PCA, and feature selection method, mRMR, provide the equivalent classification accuracy at a reduced number of features. These two approaches reduce the computational cost of the proposed scheme.

The best classification accuracy of 99.12±0.44, 99.70±0.29 and 97.68±1.04 has been achieved in A2C, A4C, and PLAX views, respectively, using the DWT based texture features. The db2 and db4 wavelet performed better among all the family members. From the results, it can be concluded that the proposed approach generates the most discriminative texture features. The proposed approach for the severity classification of MR has been evaluated with the accuracy, sensitivity and the specificity of the system.

7.2 Scope for Future Work

Even though comprehensive experimental work has been done here, to improve the classification accuracy of CAD system, the following are some of the suggestions for implementation in future research work in this field:

1. The limitation of this work is that the data used for this work has been taken from the single source, therefore, a future step is to evaluate the proposed methods using MR data from several other sources to remove the chance of biasness ib image data.
2. The multiscale despeckling algorithms were not studied in this work. A work can be extended for the improvement of multiscale despeckling algorithms.
3. Further, to get the multiresolution images, the GP and DWT have been employed. Several other multiresolution techniques, namely, fractional wavelet transform (FRWT) and dual-tree complex wavelet transform (DTCWT) may be investigated to produce significant texture features.
4. The proposed approach has used Daubechies wavelets to decompose the images by DWT. Several other mother wavelets may be investigated to see their effect on the feature extraction and classification of MR images.
5. In this study, the PCA (dimensionality reduction) and mRMR (features selection) techniques have been used to reduce the dimension of feature vector data. Some other techniques such as Kernel PCA (dimensionality reduction), genetic algorithm, and correlation-based feature selection may be investigated to reduce the feature vector data.
6. After compiling the ideas proposed in the present work, an expert system can also be designed and developed to assist the cardiologist in characterizing the MR images.

PUBLICATIONS FROM THE RESEARCH WORK

JOURNALS

1. **Balodi, Arun**, M. L. Dewal, R. S. Anand and Anurag Rawat, "Texture based classification of the severity of mitral regurgitation," Computers in biology and medicine 73 (2016): 157-164. (**SCI Indexed, Impact Factor: 1.953**)

2. **Balodi, Arun**, M. L. Dewal, R. S. Anand and Anurag Rawat, "Categorization of the mitral regurgitation using multiresolution local binary pattern," Neural Computing and Applications, Springer (Under review).

3. **Balodi, Arun**, M. L. Dewal, R. S. Anand and Anurag Rawat, "Computer-aided diagnosis system for severity analysis of mitral regurgitation using discrete wavelet transform," IETE Image Processing (Under review).

4. **Balodi, Arun**, M. L. Dewal, R. S. Anand and Anurag Rawat, "Despeckling in echocardiographic images using hybrid fuzzy filter," communicated to Optik - International Journal for Light and Electron Optics.

CONFERENCES

1. **Balodi, Arun**, M. L. Dewal, and Anurag Rawat, "Comparison of despeckle filters for ultrasound images," in IEEE 2^{nd} International Conference on Computing for Sustainable Global Development (INDIACom), 2015.

2. **Balodi, Arun**, R. S. Anand, M. L. Dewal, and Anurag Rawat, "Comparison of color spaces for the severity analysis of mitral regurgitation," in IEEE 4^{th} International Conference on Computing for Sustainable Global Development (INDIACom), 2017.

BIBLIOGRAPHY

[1] P. A. Grayburn, N. J. Weissman, and J. L. Zamorano, “Quantitation of mitral regurgitation,” *Circulation*, vol. 126, no. 16, pp. 2005–2017, 2012.

[2] P. Suetens, *Fundamentals of Medical Imaging*. Cambridge University Press, 2009.

[3] S. Kaddoura, *Echo Made Easy*. Elsevier Health Sciences, 2012.

[4] C. M. Otto, *Textbook of Clinical Echocardiography*. Elsevier Health Sciences, 2013.

[5] R. Acharya, R. Wasserman, J. Stevens, and C. Hinojosa, “Biomedical imaging modalities: A tutorial,” *Computerized Medical Imaging and Graphics*, vol. 19, no. 1, pp. 3–25, 1995.

[6] J. T. Bushberg and J. M. Boone, *The Essential Physics of Medical Imaging*. Lippincott Williams & Wilkins, 2011.

[7] Y. Yu and S. T. Acton, “Speckle reducing anisotropic diffusion,” *IEEE Transactions on Image Processing*, vol. 11, no. 11, pp. 1260–1270, 2002.

[8] S. Finn, M. Glavin, and E. Jones, “Echocardiographic speckle reduction comparison,” *IEEE Transactions on Ultrasonics, Ferroelectrics, and Frequency Control*, vol. 58, no. 1, pp. 82–101, 2011.

[9] A. Hammoude, “Endocardial border identification in two-dimensional echocardiographic images: Review of methods,” *Computerized Medical Imaging and Graphics*, vol. 22, no. 3, pp. 181–193, 1998.

[10] M. Mulet-Parada and J. A. Noble, “2d+ t acoustic boundary detection in echocardiography,” *Medical Image Analysis*, vol. 4, no. 1, pp. 21–30, 2000.

[11] S. B. Mehta, S. Chaudhury, A. Bhattacharyya, and L. Mathew, “Soft computing techniques for medical image analysis,” *IETE Technical Review*, vol. 20, no. 1, pp. 47–56, 2003.

[12] T. Shiota, “Automated cardiac flow measurement by digital colour Doppler echocardiography,” 2002.

[13] J. Yan and T. Zhuang, “Applying improved fast marching method to endocardial boundary detection in echocardiographic images,” *Pattern Recognition Letters*, vol. 24, no. 15, pp. 2777–2784, 2003.

[14] A. Fernández-Caballero and J. M. Vega-Riesco, “Determining heart parameters through left ventricular automatic segmentation for heart disease diagnosis,” *Expert Systems with Applications*, vol. 36, no. 2, pp. 2234–2249, 2009.

[15] R. S. Sengar, A. Upadhyay, P. G. Patwardhan, M. Singh, and V. M. Gadre, “Approaches based on non-separable filter banks in 2D gel electrophoresis image analysis,” in *International Conference on Asia Pacific Signal and Information Processing Association (APSIPA)*, 2010, pp. 387–392.

[16] J. Weese, J. Peters, C. Meyer, I. Wächter, R. Kneser, H. Lehmann, O. Ecabert, H. Barschdorf, R. Hanna, F. M. Weber *et al.*, “The generation of patient-specific heart models for diagnosis and interventions,” in *International Workshop on Statistical Atlases and Computational Models of the Heart*. Springer, 2010, pp. 25–35.

[17] S. D. Cataldo and E. Ficarra, “Mining textural knowledge in biological images: Applications, methods and trends,” *Computational and Structural Biotechnology Journal*, vol. 15, pp. 56 – 67, 2017.

[18] A. O. de Carvalho Filho, A. C. Silva, A. C. de Paiva, R. A. Nunes, and M. Gattass, “Computer-aided diagnosis system for lung nodules based on computed tomography using shape analysis, a genetic algorithm, and SVM,” *Medical & Biological Engineering & Computing*, pp. 1–18, 2016.

[19] C. I. Christodoulou, C. S. Pattichis, M. Pantziaris, and A. Nicolaides, “Texture-based classification of atherosclerotic carotid plaques,” *IEEE Transactions on Medical Imaging*, vol. 22, no. 7, pp. 902–912, 2003.

[20] D.-R. Chen, R.-F. Chang, C.-J. Chen, M.-F. Ho, S.-J. Kuo, S.-T. Chen, S.-J. Hung, and W. K. Moon, “Classification of breast ultrasound images using fractal feature,” *Clinical Imaging*, vol. 29, no. 4, pp. 235–245, 2005.

[21] O. Dössel, D. Farina, M. B. Mohr, M. Reumann, G. Seemann, and D. L. Weiss, “Computer-assisted planning of cardiac interventions and heart surgery.” in *GI Jahrestagung*. Citeseer, 2006, pp. 499–506.

[22] D. Hanbay, “An expert system based on least square support vector machines for diagnosis of the valvular heart disease,” *Expert Systems with Applications*, vol. 36, no. 3, pp. 4232–4238, 2009.

[23] S. Gao, Y. Peng, H. Guo, W. Liu, T. Gao, Y. Xu, and X. Tang, “Texture analysis and classification of ultrasound liver images.” *Biomedical Materials and Engineering*, vol. 24, no. 1, pp. 1209–1216, 2013.

[24] N. G. Hedeshi and M. S. Abadeh, “Coronary artery disease detection using a fuzzy-boosting PSO approach,” *Computational Intelligence and Neuroscience*, vol. 2014, p. 6, 2014.

[25] F. Ciompi, S. Balocco, J. Rigla, X. Carrillo, J. Mauri, and P. Radeva, “Computer-aided detection of intracoronary stent in intravascular ultrasound sequences,” *Medical Physics*, vol. 43, no. 10, pp. 5616–5625, 2016.

[26] P. A. Grayburn, W. Fehske, H. Omran, M. E. Brickner, and B. Lüderitz, “Multiplane transesophageal echocardiographic assessment of mitral regurgitation by Doppler color flow mapping of the vena contracta,” *The American Journal of Cardiology*, vol. 74, no. 9, pp. 912–917, 1994.

[27] H. Tek and B. B. Kimia, “Volumetric segmentation of medical images by three-dimensional bubbles,” *Computer Vision and Image Understanding*, vol. 65, no. 2, pp. 246 – 258, 1997.

[28] X. Zhou, M. Jones, T. Shiota, I. Yamada, D. Teien, and D. J. Sahn, “Vena contracta imaged by Doppler color flow mapping predicts the severity of eccentric mitral regurgitation better than color jet area: A chronic animal study,” *Journal of the American College of Cardiology*, vol. 30, no. 5, pp. 1393–1398, 1997.

[29] K. Miyatake, S. Izumi, M. Okamoto, N. Kinoshita, H. Asonuma, H. Nakagawa, K. Yamamoto, M. Takamiya, H. Sakakibara, and Y. Nimura, “Semiquantitative grading of severity of mitral regurgitation by real-time two-dimensional Doppler flow imaging technique,” *Journal of the American College of Cardiology*, vol. 7, no. 1, pp. 82–88, 1986.

[30] F. Helmcke, N. Nanda, M. Hsiung, B. Soto, C. Adey, R. Goyal, and R. Gatewood, “Color Doppler assessment of mitral regurgitation with orthogonal planes,” *Circulation*, vol. 75, no. 1, pp. 175–183, 1987.

[31] H. Baumgartner, H. Kratzer, G. Helmreich, and P. Kühn, “Quantitation of aortic regurgitation by colour coded cross-sectional Doppler echocardiography,” *European Heart Journal*, vol. 9, no. 4, pp. 380–387, 1988.

[32] H. Baumgartner, H. Schima, and P. Kühn, “Value and limitations of proximal jet dimensions for the quantitation of valvular regurgitation: An in vitro study using Doppler flow imaging,” *Journal of the American Society of Echocardiography*, vol. 4, no. 1, pp. 57–66, 1991.

[33] C. Tribouilloy, W. F. Shen, J.-P. Quéré, J.-L. Rey, D. Choquet, H. Dufosse, and J.-P. Lesbre, “Assessment of severity of mitral regurgitation by measuring regurgitant jet width at its origin with transesophageal Doppler color flow imaging,” *Circulation*, vol. 85, no. 4, pp. 1248–1253, 1992.

[34] W. Fehske, H. Omran, M. Manz, J. Köhler, A. Hagendorff, and B. Lüderitz, “Color-coded Doppler imaging of the vena contracta as a basis for quantification of pure mitral regurgitation,” *The American Journal of Cardiology*, vol. 73, no. 4, pp. 268–274, 1994.

[35] M. Enriquez-Sarano, L. J. Sinak, A. J. Tajik, K. R. Bailey, and J. B. Seward, “Changes in effective regurgitant orifice throughout systole in patients with mitral valve prolapse,” *Circulation*, vol. 92, no. 10, pp. 2951–2958, 1995.

[36] S. A. Hall, M. E. Brickner, D. L. Willett, W. N. Irani, I. Afridi, and P. A. Grayburn, “Assessment of mitral regurgitation severity by Doppler color flow mapping of the vena contracta,” *Circulation*, vol. 95, no. 3, pp. 636–642, 1997.

[37] S. K. Heinle, S. A. Hall, M. E. Brickner, D. L. Willett, and P. A. Grayburn, “Comparison of vena contracta width by multiplane transesophageal echocardiography with quantitative doppler assessment of mitral regurgitation,” *The American Journal of Cardiology*, vol. 81, no. 2, pp. 175–179, 1998.

[38] A. M. Kizilbash, D. L. Willett, M. E. Brickner, S. K. Heinle, and P. A. Grayburn, “Effects of afterload reduction on vena contracta width in mitral regurgitation,” *Journal of the American College of Cardiology*, vol. 32, no. 2, pp. 427–431, 1998.

[39] J. P. Quéré, C. Tribouilloy, and M. Enriquez-Sarano, "Vena contracta width measurement: Theoretic basis and usefulness in the assessment of valvular regurgitation severity," *Current Cardiology Reports*, vol. 5, no. 2, pp. 110–115, 2003.

[40] S. F. Yiu, M. Enriquez-Sarano, C. Tribouilloy, J. B. Seward, and A. J. Tajik, "Determinants of the degree of functional mitral regurgitation in patients with systolic left ventricular dysfunction," *Circulation*, vol. 102, no. 12, pp. 1400–1406, 2000.

[41] W. A. Zoghbi, M. Enriquez-Sarano, E. Foster, P. A. Grayburn, C. D. Kraft, R. A. Levine, P. Nihoyannopoulos, C. M. Otto, M. A. Quinones, H. Rakowski *et al.*, "Recommendations for evaluation of the severity of native valvular regurgitation with two-dimensional and Doppler echocardiography," *Journal of the American Society of Echocardiography*, vol. 16, no. 7, pp. 777–802, 2003.

[42] T. Utsunomiya, T. Ogawa, R. Doshi, D. Patel, M. Quan, W. L. Henry, and J. M. Gardin, "Doppler color flow proximal isovelocity surface area method for estimating volume flow rate: Effects of orifice shape and machine factors," *Journal of the American College of Cardiology*, vol. 17, no. 5, pp. 1103–1111, 1991, 10.1016/0735-1097(91)90839-2.

[43] P. A. Grayburn and R. M. Peshock, "Noninvasive quantification of valvular regurgitation," *Circulation*, vol. 94, no. 2, pp. 119–121, 1996.

[44] M. Oppizzi, M. Pisani, A. Meris, F. Maisano, A. Margonato *et al.*, "Ischemic mitral regurgitation: mechanisms and echocardiographic classification," *European Heart Journal Cardiovascular Imaging*, vol. 9, no. 2, pp. 207–221, 2008.

[45] M. Pu, P. M. Vandervoort, B. P. Griffin, D. Y. Leung, W. J. Stewart, D. M. Cosgrove, and J. D. Thomas, "Quantification of mitral regurgitation by the proximal convergence method using transesophageal echocardiography," *Circulation*, vol. 92, no. 8, pp. 2169–2177, 1995.

[46] B. Mutlu, A. Bitigen, M. Türkmen, and Y. Başaran, "Evaluation of the proximal isovelocity surface area method and vena contracta width in mitral regurgitation with the transthoracic and transesophageal echocardiography," *Turkish Society of Cardiology*, vol. 31, no. 7, pp. 361–370, 2003.

[47] S. Bhachu, “A new method to quantify mitral regurgitation,” *Imaging (MRI)*, vol. 11, p. 12, 2004.

[48] O. Başpinar, S. Karaaslan, and B. Oran, “PISA method for assessment of mitral regurgitation in children.” *The Anatolian Journal of Cardiology*, vol. 5, no. 3, pp. 167–171, 2005.

[49] S. H. Little, B. Pirat, R. Kumar, S. R. Igo, M. McCulloch, C. J. Hartley, J. Xu, and W. A. Zoghbi, “Three-dimensional color Doppler echocardiography for direct measurement of vena contracta area in mitral regurgitation,” *JACC: Cardiovascular Imaging*, vol. 1, no. 6, pp. 695–704, 2008.

[50] N. A. Marsan, J. J. Westenberg, C. Ypenburg, V. Delgado, R. J. van Bommel, S. D. Roes, G. Nucifora, R. J. van der Geest, A. de Roos, J. C. Reiber *et al.*, “Quantification of functional mitral regurgitation by real-time 3D echocardiography,” *JACC: Cardiovascular Imaging*, vol. 2, no. 11, pp. 1245–1252, 2009.

[51] S. Biner, A. Rafique, F. Rafii, K. Tolstrup, O. Noorani, T. Shiota, S. Gurudevan, and R. J. Siegel, “Reproducibility of proximal isovelocity surface area, vena contracta, and regurgitant jet area for assessment of mitral regurgitation severity,” *JACC: Cardiovascular Imaging*, vol. 3, no. 3, pp. 235–243, 2010.

[52] N. Quader and V. H. Rigolin, “Two and three dimensional echocardiography for pre-operative assessment of mitral valve regurgitation,” *Cardiovascular Ultrasound*, vol. 12, no. 1, p. 42, 2014.

[53] M.-M. Lee, A. Salahuddin, M. J. Garcia, and D. M. Spevack, “Left ventricular early inflow–outflow index: A novel echocardiographic indicator of mitral regurgitation severity,” *Journal of the American Heart Association*, vol. 4, no. 6, p. e000781, 2015.

[54] I. Simpson and D. Sahn, “Quantification of valvular regurgitation by Doppler echocardiography,” *Circulation*, vol. 84, no. 3 Suppl, pp. I188–92, 1991.

[55] E. Schwammenthal, C. Chen, M. Giesler, A. Sagie, J. L. Guerrero, J. A. V. de Prada, V. Hombach, A. E. Weyman, and R. A. Levine, “New method for accurate calculation of regurgitant flow rate based on analysis of Doppler color flow maps of the proximal flow field validation in a canine model of mitral regurgitation with initial application in

patients," *Journal of the American College of Cardiology*, vol. 27, no. 1, pp. 161–172, 1996.

[56] S. Chandra, L. Weinert, L. Sugeng, I. Salgo, S. Settlemierer, J. Shen, V. Mor-Avi, and R. Lang, "Volumetric measurement of the anatomic regurgitant orifice area in mitral regurgitation: Comparison with two-dimensional flow convergence analysis," in *IEEE Conference on Computers in Cardiology*, 2009, pp. 769–772.

[57] P. A. Grayburn and P. Bhella, "Grading severity of mitral regurgitation by echocardiography: Science or art?" *JACC: Cardiovascular Imaging*, vol. 3, no. 3, pp. 244–246, 2010.

[58] J. Ge, D. Zhou, W. Pan, C. Pan, and H. Luo, "Initial experience of treating patients with severe mitral regurgitation with transcatheter mitral valve edge-to-edge repair in china," *Chinese Journal of Cardiovascular Diseases*, vol. 41, no. 2, pp. 99–102, 2013.

[59] H. Kaneko, S. Suzuki, T. Uejima, H. Kano, S. Matsuno, H. Takai, Y. Oikawa, J. Yajima, T. Aizawa, and T. Yamashita, "Functional mitral regurgitation and left ventricular systolic dysfunction in the recent era of cardiovascular clinical practice, an observational cohort study," *Hypertension Research*, vol. 37, no. 12, pp. 1082–1087, 2014.

[60] I. L. Kron, J. Hung, J. R. Overbey, D. Bouchard, A. C. Gelijns, A. J. Moskowitz, P. Voisine, P. T. O'Gara, M. Argenziano, R. E. Michler *et al.*, "Predicting recurrent mitral regurgitation after mitral valve repair for severe ischemic mitral regurgitation," *The Journal of Thoracic and Cardiovascular Surgery*, vol. 149, no. 3, pp. 752–761, 2015.

[61] W. P. Santamore, F. N. DiMeo, and P. R. Lynch, "A comparative study of various single-plane cineangiocardiographic methods to measure left-ventricular volume," *IEEE Transactions on Biomedical Engineering*, vol. BME-20, no. 6, pp. 417–421, 1973.

[62] J. Bartunek, P. J. Vantrimpont, and B. De Bruyne, "Left atrial volume determination by echocardiography," *The International Journal of Cardiac Imaging*, vol. 10, no. 4, pp. 263–268, 1994.

[63] H.-H. Chang and D. J. Valentino, “An electrostatic deformable model for medical image segmentation,” *Computerized Medical Imaging and Graphics*, vol. 32, no. 1, pp. 22–35, 2008.

[64] N. Kachenoura, A. Delouche, A. Herment, F. Frouin, and B. Diebold, “Automatic detection of end systole within a sequence of left ventricular echocardiographic images using autocorrelation and mitral valve motion detection,” in *29th IEEE Annual International Conference on Engineering in Medicine and Biology Society, (EMBS)*, 2007, pp. 4504–4507.

[65] P. Watton, X. Luo, M. Yin, G. Bernacca, and D. Wheatley, “Effect of ventricle motion on the dynamic behaviour of chorded mitral valves,” *Journal of Fluids and Structures*, vol. 24, no. 1, pp. 58–74, 2008.

[66] W. Ohyama, T. Wakabayashi, F. Kimura, S. Tsuruoka, and K. Sekioka, “Automatic left ventricular endocardium detection in echocardiograms based on ternary thresholding method,” in *15th IEEE International Conference on Pattern Recognition*, vol. 4, 2000, pp. 320–323.

[67] J. Hansegard, E. Steen, S. I. Rabben, A. H. Torp, H. Torp, S. Frigstad, and B. Olstad, “Knowledge based extraction of the left ventricular endocardial boundary from 2D echocardiograms,” in *IEEE Symposium on Ultrasonics*, vol. 3, 2004, pp. 2121–2124.

[68] M. Kass, A. Witkin, and D. Terzopoulos, “Snakes: Active contour models,” *International Journal of Computer Vision*, vol. 1, no. 4, pp. 321–331, 1988.

[69] F. L. Valverde, N. Guil, and J. Muñoz, “Segmentation of vessels from mammograms using a deformable model,” *Computer Methods and Programs in Biomedicine*, vol. 73, no. 3, pp. 233–247, 2004.

[70] W. J. Niessen, B. M. T. H. Romeny, and M. A. Viergever, “Geodesic deformable models for medical image analysis,” *IEEE Transactions on Medical Imaging*, vol. 17, no. 4, pp. 634–641, 1998.

[71] D. J. Williams and M. Shah, “A fast algorithm for active contours and curvature estimation,” *CVGIP: Image Understanding*, vol. 55, no. 1, pp. 14–26, 1992.

[72] X. Liao and D. C. Liu, "Numerical analysis of a deformable model for ultrasound border detection," in *7th Asian-Pacific Conference on Medical and Biological Engineering*, 2008, pp. 537–541.

[73] C. B. Burckhardt, "Speckle in ultrasound B-mode scans," *IEEE Transactions on Sonics and Ultrasonics*, vol. 25, no. 1, pp. 1–6, 1978.

[74] R. F. Wagner, S. W. Smith, J. M. Sandrik, and H. Lopez, "Statistics of speckle in ultrasound B-scans," *IEEE Transactions on Sonics and Ultrasonics*, vol. 30, no. 3, pp. 156–163, 1983.

[75] R. Massay, R. Logan-Sinclair, J. Bamber, and D. Gibson, "Quantitative effects of speckle reduction on cross sectional echocardiographic images." *British Heart Journal*, vol. 62, no. 4, pp. 298–304, 1989.

[76] A. Achim, A. Bezerianos, and P. Tsakalides, "Novel bayesian multiscale method for speckle removal in medical ultrasound images," *IEEE Transactions on Medical Imaging*, vol. 20, no. 8, pp. 772–783, 2001.

[77] J. W. Goodman, "Some fundamental properties of speckle," *Journal of the Optical Society of America*, vol. 66, no. 11, pp. 1145–1150, 1976.

[78] P. Atkinson and M. Berry, "Random noise in ultrasonic echoes diffracted by blood," *Journal of Physics A: Mathematical, Nuclear and General*, vol. 7, no. 11, p. 1293, 1974.

[79] J. Dainty, "I the statistics of speckle patterns," *Progress in Optics*, vol. 14, pp. 1–46, 1977.

[80] Z. Shi and K. B. Fung, "A comparison of digital speckle filters," in *IEEE International Symposium on Geoscience and Remote Sensing Symposium, (IGARSS), Surface and Atmospheric Remote Sensing: Technologies, Data Analysis and Interpretation*, vol. 4, 1994, pp. 2129–2133.

[81] J.-S. Lee, "Digital image enhancement and noise filtering by use of local statistics," *IEEE Transactions on Pattern Analysis and Machine Intelligence*, no. 2, pp. 165–168, 1980.

[82] ——, “Refined filtering of image noise using local statistics,” *Computer Graphics and Image Processing*, vol. 15, no. 4, pp. 380–389, 1981.

[83] V. Frost, J. Stiles, K. S. Shanmugam, J. Holtzman, and S. Smith, “An adaptive filter for smoothing noisy radar images,” *Proceedings of the IEEE*, vol. 69, no. 1, pp. 133–135, 1981.

[84] V. S. Frost, J. A. Stiles, K. S. Shanmugan, and J. C. Holtzman, “A model for radar images and its application to adaptive digital filtering of multiplicative noise,” *IEEE Transactions on Pattern Analysis and Machine Intelligence*, no. 2, pp. 157–166, 1982.

[85] D. T. Kuan, A. A. Sawchuk, T. C. Strand, and P. Chavel, “Adaptive noise smoothing filter for images with signal-dependent noise,” *IEEE Transactions on Pattern Analysis and Machine Intelligence*, no. 2, pp. 165–177, 1985.

[86] D. Kuan, A. Sawchuk, T. Strand, and P. Chavel, “Adaptive restoration of images with speckle,” *IEEE Transactions on Acoustics, Speech, and Signal Processing*, vol. 35, no. 3, pp. 373–383, 1987.

[87] S. Solbo and T. Eltoft, “Homomorphic wavelet-based statistical despeckling of SAR images,” *IEEE Transactions on Geoscience and Remote Sensing*, vol. 42, no. 4, pp. 711–721, 2004.

[88] J. Saniie, T. Wang, and N. M. Bilgutay, “Analysis of homomorphic processing for ultrasonic grain signal characterization,” *IEEE Transactions on Ultrasonics, Ferroelectrics, and Frequency Control*, vol. 36, no. 3, pp. 365–375, 1989.

[89] T. Loupas, W. McDicken, and P. Allan, “An adaptive weighted median filter for speckle suppression in medical ultrasonic images,” *IEEE Transactions on Circuits and Systems*, vol. 36, no. 1, pp. 129–135, 1989.

[90] T. Chen and H. R. Wu, “Adaptive impulse detection using center-weighted median filters,” *IEEE Signal Processing Letters*, vol. 8, no. 1, pp. 1–3, 2001.

[91] C. Loizou, C. Christodoulou, C. Pattichis, R. Istepanian, M. Pantziaris, and A. Nicolaides, “Speckle reduction in ultrasound images of atherosclerotic carotid plaque,” in *14th IEEE International Conference on Digital Signal Processing, (DSP)*, vol. 2, 2002, pp. 525–528.

[92] A. Ozcan, A. Bilenca, A. E. Desjardins, B. E. Bouma, and G. J. Tearney, “Speckle reduction in optical coherence tomography images using digital filtering,” *Journal of the Optical Society of America A*, vol. 24, no. 7, pp. 1901–1910, 2007.

[93] J. Tang, S. Guo, Q. Sun, Y. Deng, and D. Zhou, “Speckle reducing bilateral filter for cattle follicle segmentation,” *BMC Genomics*, vol. 11, no. 2, p. S9, 2010.

[94] Y. Guo, Y. Wang, and T. Hou, “Speckle filtering of ultrasonic images using a modified non local-based algorithm,” *Biomedical Signal Processing and Control*, vol. 6, no. 2, pp. 129–138, 2011.

[95] N. Biradar, M. L. Dewal, and M. K. Rohit, “Speckle noise reduction in b-mode echocardiographic images: A comparison,” *IETE Technical Review*, vol. 32, no. 6, pp. 435–453, 2015.

[96] P. Perona and J. Malik, “Scale-space and edge detection using anisotropic diffusion,” *IEEE Transactions on Pattern Analysis and Machine Intelligence*, vol. 12, no. 7, pp. 629–639, 1990.

[97] J. Weickert, “Coherence-enhancing diffusion filtering,” *International Journal of Computer Vision*, vol. 31, no. 2, pp. 111–127, 1999.

[98] K. Z. Abd-Elmoniem, A.-B. Youssef, and Y. M. Kadah, “Real-time speckle reduction and coherence enhancement in ultrasound imaging via nonlinear anisotropic diffusion,” *IEEE Transactions on Biomedical Engineering*, vol. 49, no. 9, pp. 997–1014, 2002.

[99] G. Gilboa, N. Sochen, and Y. Y. Zeevi, “Image enhancement and denoising by complex diffusion processes,” *IEEE transactions on Pattern Analysis and Machine Intelligence*, vol. 26, no. 8, pp. 1020–1036, 2004.

[100] D. Mittal, V. Kumar, S. C. Saxena, N. Khandelwal, and N. Kalra, “Enhancement of the ultrasound images by modified anisotropic diffusion method,” *Medical & Biological Engineering & Computing*, vol. 48, no. 12, pp. 1281–1291, 2010.

[101] S. Aja-Fernández and C. Alberola-López, “On the estimation of the coefficient of variation for anisotropic diffusion speckle filtering,” *IEEE Transactions on Image Processing*, vol. 15, no. 9, pp. 2694–2701, 2006.

[102] K. Krissian, C.-F. Westin, R. Kikinis, and K. G. Vosburgh, “Oriented speckle reducing anisotropic diffusion,” *IEEE Transactions on Image Processing*, vol. 16, no. 5, pp. 1412–1424, 2007.

[103] F. Liu and J. Liu, “Anisotropic diffusion for image denoising based on diffusion tensors,” *Journal of Visual Communication and Image Representation*, vol. 23, no. 3, pp. 516–521, 2012.

[104] K. Saini, M. Dewal, and M. Rohit, “Modified nonlinear complex diffusion filter (MNCDF),” *Journal of Echocardiography*, vol. 10, no. 2, pp. 48–55, 2012.

[105] P. Coupé, P. Hellier, C. Kervrann, and C. Barillot, “Nonlocal means-based speckle filtering for ultrasound images,” *IEEE Transactions on Image Processing*, vol. 18, no. 10, pp. 2221–2229, 2009.

[106] A. Buades, B. Coll, and J.-M. Morel, “A non-local algorithm for image denoising,” in *IEEE Conference on Computer Vision and Pattern Recognition, (CVPR)*, vol. 2. IEEE, 2005, pp. 60–65.

[107] C.-A. Deledalle, L. Denis, and F. Tupin, “Iterative weighted maximum likelihood denoising with probabilistic patch-based weights,” *IEEE Transactions on Image Processing*, vol. 18, no. 12, pp. 2661–2672, 2009.

[108] I. Elamvazuthi, M. L. B. M. Zain, and K. Begam, “Despeckling of ultrasound images of bone fracture using multiple filtering algorithms,” *Mathematical and Computer Modelling*, vol. 57, no. 1, pp. 152–168, 2013.

[109] C. P. Loizou and C. S. Pattichis, “Despeckle filtering algorithms and software for ultrasound imaging,” *Synthesis Lectures on Algorithms and Software in Engineering*, vol. 1, no. 1, pp. 1–166, 2008.

[110] C. P. Loizou, C. S. Pattichis, C. I. Christodoulou, R. S. Istepanian, M. Pantziaris, and A. Nicolaides, “Comparative evaluation of despeckle filtering in ultrasound imaging of the carotid artery,” *IEEE Transactions on Ultrasonics, Ferroelectrics, and Frequency Control*, vol. 52, no. 10, pp. 1653–1669, 2005.

[111] C. P. Loizou, C. Theofanous, M. Pantziaris, and T. Kasparis, “Despeckle filtering software toolbox for ultrasound imaging of the common carotid artery,” *Computer Methods and Programs in Biomedicine*, vol. 114, no. 1, pp. 109–124, 2014.

[112] J. L. Mateo and A. Fernández-Caballero, “Finding out general tendencies in speckle noise reduction in ultrasound images,” *Expert Systems with Applications*, vol. 36, no. 4, pp. 7786–7797, 2009.

[113] R. Srivastava, J. Gupta, and H. Parthasarthy, “Comparison of PDE based and other techniques for speckle reduction from digitally reconstructed holographic images,” *Optics and Lasers in Engineering*, vol. 48, no. 5, pp. 626–635, 2010.

[114] P. C. Tay, C. D. Garson, S. T. Acton, and J. A. Hossack, “Ultrasound despeckling for contrast enhancement,” *IEEE Transactions on Image Processing*, vol. 19, no. 7, pp. 1847–1860, 2010.

[115] J. Zhang, C. Wang, and Y. Cheng, “Comparison of despeckle filters for breast ultrasound images,” *Circuits, Systems, and Signal Processing*, vol. 34, no. 1, pp. 185–208, 2015.

[116] J. E. Wilhjelm, M.-L. Gronholdt, B. Wiebe, S. K. Jespersen, L. K. Hansen, and H. Sillesen, “Quantitative analysis of ultrasound B-mode images of carotid atherosclerotic plaque: correlation with visual classification and histological examination,” *IEEE Transactions on Medical Imaging*, vol. 17, no. 6, pp. 910–922, 1998.

[117] R. M. Haralick, K. Shanmugam, and I. H. Dinstein, “Textural features for image classification,” *IEEE Transactions on Systems, Man and Cybernetics*, no. 6, pp. 610–621, 1973.

[118] J. S. Weszka, C. R. Dyer, and A. Rosenfeld, “A comparative study of texture measures for terrain classification,” *IEEE Transactions on Systems, Man and Cybernetics*, no. 4, pp. 269–285, 1976.

[119] M. Amadasun and R. King, “Textural features corresponding to textural properties,” *IEEE Transactions on Acoustics Speech and Signal Processing*, vol. 19, no. 5, pp. 1264–1274, 1989.

[120] C.-M. Wu, Y.-C. Chen, and K.-S. Hsieh, “Texture features for classification of ultrasonic liver images,” *IEEE Transactions on Medical Imaging*, vol. 11, no. 2, pp. 141–152, 1992.

[121] K. I. Laws, “Rapid texture identification,” in *24th Annual Technical Symposium o*. International Society for Optics and Photonics, 1980, pp. 376–381.

[122] C.-Y. Chang, S.-J. Chen, and M.-F. Tsai, “Application of support-vector-machine-based method for feature selection and classification of thyroid nodules in ultrasound images,” *Pattern Recognition*, vol. 43, no. 10, pp. 3494–3506, 2010.

[123] M. Singh, S. Singh, and S. Gupta, “An information fusion based method for liver classification using texture analysis of ultrasound images,” *Information Fusion*, vol. 19, pp. 91–96, 2014.

[124] V. Sudarshan, U. R. Acharya, E. Y.-K. Ng, C. S. Meng, R. San Tan, and D. N. Ghista, “Automated identification of infarcted myocardium tissue characterization using ultrasound images: A review,” *IEEE Reviews in Biomedical Engineering*, vol. 8, pp. 86–97, 2015.

[125] D. Mukherjee, Q. J. Wu, and G. Wang, “A comparative experimental study of image feature detectors and descriptors,” *Machine Vision and Applications*, vol. 26, no. 4, pp. 443–466, 2015.

[126] T. Ojala, M. Pietikäinen, and T. Mäenpää, “Multiresolution gray-scale and rotation invariant texture classification with local binary patterns,” *IEEE Transactions on Pattern Analysis and Machine Intelligence,*, vol. 24, no. 7, pp. 971–987, 2002.

[127] M. Pietikäinen, T. Ojala, and Z. Xu, “Rotation-invariant texture classification using feature distributions,” *Pattern Recognition*, vol. 33, no. 1, pp. 43–52, 2000.

[128] T. Ahonen, A. Hadid, and M. Pietikainen, “Face description with local binary patterns: Application to face recognition,” *IEEE Transactions on Pattern Analysis and Machine Intelligence*, vol. 28, no. 12, pp. 2037–2041, 2006.

[129] M. Heikkila and M. Pietikainen, “A texture-based method for modeling the background and detecting moving objects,” *IEEE Transactions on Pattern Analysis and Machine Intelligence*, vol. 28, no. 4, pp. 657–662, 2006.

[130] G. Zhao and M. Pietikainen, “Dynamic texture recognition using local binary patterns with an application to facial expressions,” *IEEE Transactions on Pattern Analysis and Machine Intelligence*, vol. 29, no. 6, pp. 915–928, 2007.

[131] L. Nanni and A. Lumini, “Local binary patterns for a hybrid fingerprint matcher,” *Pattern Recognition*, vol. 41, no. 11, pp. 3461–3466, 2008.

[132] A. Oliver, X. Lladó, J. Freixenet, and J. Martí, “False positive reduction in mammographic mass detection using local binary patterns,” *Medical Image Computing and Computer-Assisted Intervention–MICCAI 2007*, pp. 286–293, 2007.

[133] D. Unay, A. Ekin, M. Cetin, R. Jasinschi, and A. Ercil, “Robustness of local binary patterns in brain mr image analysis,” in *29th IEEE Annual International Conference on Engineering in Medicine and Biology Society, (EMBS).* IEEE, 2007, pp. 2098–2101.

[134] D. Unay, A. Ekin, and R. Jasinschi, “Medical image search and retrieval using local binary patterns and klt feature points,” in *15th IEEE International Conference on Image Processing, (ICIP)*, 2008, pp. 997–1000.

[135] E. G. Keramidas, D. K. Iakovidis, D. Maroulis, and N. Dimitropoulos, “Thyroid texture representation via noise resistant image features,” in *21st IEEE International Symposium on Computer-Based Medical Systems, (CBMS)*, 2008, pp. 560–565.

[136] S. Murala and Q. Wu, “Local mesh patterns versus local binary patterns: biomedical image indexing and retrieval,” *IEEE Journal of Biomedical and Health Informatics,*, vol. 18, no. 3, pp. 929–938, 2014.

[137] S. Murala and Q. J. Wu, “Spherical symmetric 3D local ternary patterns for natural, texture and biomedical image indexing and retrieval,” *Neurocomputing*, vol. 149, pp. 1502–1514, 2015.

[138] C. Bai, K. Kpalma, and J. Ronsin, “An improved feature vector for content-based image retrieval in dct domain,” in *International Conference on Computer Vision Theory and Applications (VISAPP)*, 2013, p. 4.

[139] S. G. Mallat, “A theory for multiresolution signal decomposition: The wavelet representation,” *IEEE Transactions on Pattern Analysis and Machine Intelligence*, vol. 11, no. 7, pp. 674–693, 1989.

[140] D. Gabor, “Theory of communication. part 1: The analysis of information,” *Journal of the Institution of Electrical Engineers-Part III: Radio and Communication Engineering*, vol. 93, no. 26, pp. 429–441, 1946.

[141] J. G. Daugman, “Two-dimensional spectral analysis of cortical receptive field profiles,” *Vision Research*, vol. 20, no. 10, pp. 847–856, 1980.

[142] P. J. Burt and E. H. Adelson, “A multiresolution spline with application to image mosaics,” *ACM Transactions on Graphics (TOG)*, vol. 2, no. 4, pp. 217–236, 1983.

[143] H. Sharma, N. Zerbe, D. Heim, S. Wienert, H.-M. Behrens, O. Hellwich, and P. Hufnagl, “A multi-resolution approach for combining visual information using nuclei segmentation and classification in histopathological images.” in *International Conference on Computer Vision Theory and Applications*, 2015, pp. 37–46.

[144] H. Olkkonen and P. Pesola, “Gaussian pyramid wavelet transform for multiresolution analysis of images,” *Graphical Models and Image Processing*, vol. 58, no. 4, pp. 394–398, 1996.

[145] A. R. Yadav, R. Anand, M. Dewal, and S. Gupta, “Gaussian image pyramid based texture features for classification of microscopic images of hardwood species,” *Optik-International Journal for Light and Electron Optics*, vol. 126, no. 24, pp. 5570–5578, 2015.

[146] P. Burt and E. Adelson, “The Laplacian pyramid as a compact image code,” *IEEE Transactions on Communications*, vol. 31, no. 4, pp. 532–540, 1983.

[147] E. G. Llano, M. S. García-Vázquez, L. M. Zamudio-Fuentes, J. M. C. Vargas, and A. A. Ramírez-Acosta, “Analysis of the improvement on textural information in human iris recognition,” in *VII Latin American Congress on Biomedical Engineering (CLAIB)*, 2017, pp. 373–376.

[148] E. H. Adelson, C. H. Anderson, J. R. Bergen, P. J. Burt, and J. M. Ogden, “Pyramid methods in image processing,” *RCA Engineer*, vol. 29, no. 6, pp. 33–41, 1984.

[149] G. Bucci, S. Cagnoni, and R. De Dominicis, “Integrating content-based retrieval in a medical image reference database,” *Computerized Medical Imaging and Graphics*, vol. 20, no. 4, pp. 231–241, 1996.

[150] U. Sinha and H. Kangarloo, “Principal component analysis for content-based image retrieval 1,” *Radiographics*, vol. 22, no. 5, pp. 1271–1289, 2002.

[151] F. Camastra, “Data dimensionality estimation methods: A survey,” *Pattern Recognition*, vol. 36, no. 12, pp. 2945–2954, 2003.

[152] H. Müller, N. Michoux, D. Bandon, and A. Geissbuhler, "A review of content-based image retrieval systems in medical applicationsclinical benefits and future directions," *International Journal of Medical Informatics*, vol. 73, no. 1, pp. 1–23, 2004.

[153] T. Mu, A. K. Nandi, and R. M. Rangayyan, "Classification of breast masses via nonlinear transformation of features based on a kernel matrix," *Medical & Biological Engineering & Computing*, vol. 45, no. 8, pp. 769–780, 2007.

[154] L. Wiskott, N. Krüger, N. Kuiger, and C. Von Der Malsburg, "Face recognition by elastic bunch graph matching," *IEEE Transactions on Pattern Analysis and Machine Intelligence*, vol. 19, no. 7, pp. 775–779, 1997.

[155] S. Buchala, N. Davey, T. M. Gale, and R. J. Frank, "Analysis of linear and nonlinear dimensionality reduction methods for gender classification of face images," *International Journal of Systems Science*, vol. 36, no. 14, pp. 931–942, 2005.

[156] Y. Zhang and L. Wu, "An MR brain images classifier via principal component analysis and kernel support vector machine," *Progress In Electromagnetics Research*, vol. 130, pp. 369–388, 2012.

[157] J. Khan, J. S. Wei, M. Ringner, L. H. Saal, M. Ladanyi, F. Westermann, F. Berthold, M. Schwab, C. R. Antonescu, C. Peterson *et al.*, "Classification and diagnostic prediction of cancers using gene expression profiling and artificial neural networks," *Nature Medicine*, vol. 7, no. 6, pp. 673–679, 2001.

[158] H. Peng, F. Long, and C. Ding, "Feature selection based on mutual information criteria of max-dependency, max-relevance, and min-redundancy," *IEEE Transactions on Pattern Analysis and Machine Intelligence*, vol. 27, no. 8, pp. 1226–1238, 2005.

[159] G. Chandrashekar and F. Sahin, "A survey on feature selection methods," *Computers & Electrical Engineering*, vol. 40, no. 1, pp. 16–28, 2014.

[160] E. Niaf, O. Rouvière, F. Mège-Lechevallier, F. Bratan, and C. Lartizien, "Computer-aided diagnosis of prostate cancer in the peripheral zone using multiparametric MRI," *Physics in Medicine and Biology*, vol. 57, no. 12, p. 3833, 2012.

[161] J. Ding, H. Cheng, C. Ning, J. Huang, and Y. Zhang, "Quantitative measurement for thyroid cancer characterization based on elastography," *Journal of Ultrasound in Medicine*, vol. 30, no. 9, pp. 1259–1266, 2011.

[162] W. Gómez, W. Pereira, and A. F. C. Infantosi, "Analysis of co-occurrence texture statistics as a function of gray-level quantization for classifying breast ultrasound," *IEEE Transactions on Medical Imaging*, vol. 31, no. 10, pp. 1889–1899, 2012.

[163] A. K. Jain, R. P. W. Duin, and J. Mao, "Statistical pattern recognition: A review," *IEEE Transactions on Pattern Analysis and Machine Intelligence*, vol. 22, no. 1, pp. 4–37, 2000.

[164] M. Obayya and F. Abou-Chadi, "Data fusion for heart diseases classification using multi-layer feed forward neural network," in *IEEE International Conference on Computer Engineering & Systems, (ICCES)*, 2008, pp. 67–70.

[165] I. Maglogiannis, E. Loukis, E. Zafiropoulos, and A. Stasis, "Support vectors machine-based identification of heart valve diseases using heart sounds," *Computer Methods and Programs in Biomedicine*, vol. 95, no. 1, pp. 47–61, 2009.

[166] S. Ghorai, A. Mukherjee, and P. K. Dutta, "Discriminant analysis for fast multiclass data classification through regularized kernel function approximation," *IEEE Transactions on Neural Networks*, vol. 21, no. 6, pp. 1020–1029, 2010.

[167] G. Naik, D. Kumar, and J. Jayadeva, "Myo electric classification using twin SVM and blind source separation techniques," in *ISSNIP Conference on Biosignals and Biorobotics*. ISSNIP, 2010, pp. 75–79.

[168] M. Jaeger, A. Reigber, and O. Hellwich, "A non-parametric texture descriptor for polarimetric sar data with applications to supervised classification," in *10th European Conference on Synthetic Aperture Radar (EUSAR)*. VDE, 2014, pp. 1–4.

[169] K. Lekadir, A. Galimzianova, À. Betriu, M. del Mar Vila, L. Igual, D. L. Rubin, E. Fernández, P. Radeva, and S. Napel, "A convolutional neural network for automatic characterization of plaque composition in carotid ultrasound," *IEEE Journal of Biomedical and Health Informatics*, vol. 21, no. 1, pp. 48–55, 2017.

[170] D. Boukerroui, A. Baskurt, J. A. Noble, and O. Basset, "Segmentation of ultrasound images–multiresolution 2D and 3D algorithm based on global and local statistics," *Pattern Recognition Letters*, vol. 24, no. 4, pp. 779–790, 2003.

[171] J. Tang, R. M. Rangayyan, J. Xu, I. El Naqa, and Y. Yang, “Computer-aided detection and diagnosis of breast cancer with mammography: Recent advances,” *IEEE Transactions on Information Technology in Biomedicine*, vol. 13, no. 2, pp. 236–251, 2009.

[172] N. N. Tsiaparas, S. Golemati, I. Andreadis, J. S. Stoitsis, I. Valavanis, and K. S. Nikita, “Comparison of multiresolution features for texture classification of carotid atherosclerosis from b-mode ultrasound,” *IEEE Transactions on Information Technology in Biomedicine*, vol. 15, no. 1, pp. 130–137, 2011.

[173] J. Virmani, V. Kumar, N. Kalra, and N. Khandelwal, “SVM-based characterization of liver ultrasound images using wavelet packet texture descriptors,” *Journal of Digital Imaging*, vol. 26, no. 3, pp. 530–543, 2013.

[174] S. Zhou, J. Shi, J. Zhu, Y. Cai, and R. Wang, “Shearlet-based texture feature extraction for classification of breast tumor in ultrasound image,” *Biomedical Signal Processing and Control*, vol. 8, no. 6, pp. 688–696, 2013.

[175] S. Sun, H. Wang, Z. Jiang, Y. Fang, and T. Tao, “Segmentation-based heart sound feature extraction combined with classifier models for a VSD diagnosis system,” *Expert Systems with Applications*, vol. 41, no. 4, pp. 1769–1780, 2014.

[176] A. Gharehbaghi, P. Ask, and A. Babic, “A pattern recognition framework for detecting dynamic changes on cyclic time series,” *Pattern Recognition*, vol. 48, no. 3, pp. 696–708, 2015.

[177] H. Moghaddasi and S. Nourian, “Automatic assessment of mitral regurgitation severity based on extensive textural features on 2D echocardiography videos,” *Computers in Biology and Medicine*, vol. 73, pp. 47–55, 2016.

[178] A. Balodi, M. Dewal, R. Anand, and A. Rawat, “Texture based classification of the severity of mitral regurgitation,” *Computers in Biology and Medicine*, vol. 73, pp. 157–164, 2016.

[179] X. Liu, J. L. Song, S. H. Wang, J. W. Zhao, and Y. Q. Chen, “Learning to diagnose cirrhosis with liver capsule guided ultrasound image classification,” *Sensors*, vol. 17, no. 1, p. 149, 2017.

[180] K. Sharma and J. Virmani, “A decision support system for classification of normal and medical renal disease using ultrasound images: A decision support system for medical

renal diseases," *International Journal of Ambient Computing and Intelligence*, vol. 8, no. 2, pp. 52–69, 2017.

[181] M. Abdel-Nasser, J. Melendez, A. Moreno, O. A. Omer, and D. Puig, "Breast tumor classification in ultrasound images using texture analysis and super-resolution methods," *Engineering Applications of Artificial Intelligence*, vol. 59, pp. 84–92, 2017.

[182] S. D. Solomon and B. Bulwer, *Essential Echocardiography: A Practical Handbook. Contemporary Cardiology*. Humana Press, 2007.

[183] C. M. Otto, *The Practice of Clinical Echocardiography*. Elsevier Health Sciences, 2012.

[184] V. T. Nkomo, J. M. Gardin, T. N. Skelton, J. S. Gottdiener, C. G. Scott, and M. Enriquez-Sarano, "Burden of valvular heart diseases: A population-based study," *The Lancet*, vol. 368, no. 9540, pp. 1005–1011, 2006.

[185] M. Enriquez-Sarano, C. W. Akins, and A. Vahanian, "Mitral regurgitation," *The Lancet*, vol. 373, no. 9672, pp. 1382–1394, 2009.

[186] R. A. Nishimura, C. M. Otto, R. O. Bonow, B. A. Carabello, J. P. Erwin, R. A. Guyton, P. T. O'Gara, C. E. Ruiz, N. J. Skubas, P. Sorajja *et al.*, "2014 AHA/ACC guideline for the management of patients with valvular heart disease: executive summary: A report of the american college of cardiology/american heart association task force on practice guidelines," *Journal of the American College of Cardiology*, vol. 63, no. 22, pp. 2438–2488, 2014.

[187] P. Lancellotti, C. Tribouilloy, A. Hagendorff, B. A. Popescu, T. Edvardsen, L. A. Pierard, L. Badano, J. L. Zamorano *et al.*, "Recommendations for the echocardiographic assessment of native valvular regurgitation: An executive summary from the european association of cardiovascular imaging," *European Heart Journal - Cardiovascular Imaging*, pp. 1–34, 2013.

[188] M. Halliwell, "A tutorial on ultrasonic physics and imaging techniques," *Proceedings of the Institution of Mechanical Engineers, Part H: Journal of Engineering in Medicine*, vol. 224, no. 2, pp. 127–142, 2010.

[189] S. H. C. Ortiz, T. Chiu, and M. D. Fox, "Ultrasound image enhancement: A review," *Biomedical Signal Processing and Control*, vol. 7, no. 5, pp. 419–428, 2012.

[190] E. Parvizi and Q. J. Wu, "Multiple object tracking based on adaptive depth segmentation," in *IEEE Canadian Conference on Computer and Robot Vision, (CRV'08)*, 2008, pp. 273–277.

[191] A. Schmidt, F. Almeida, C. Oswaldo, F. Pazin, J. A. Marin-Neto, B. C. Maciel *et al.*, "Valvular regurgitation by color Doppler echocardiography," *Arquivos Brasileiros de Cardiologia*, vol. 74, no. 3, pp. 273–281, 2000.

[192] R. F. Wagner, M. F. Insana, and S. W. Smith, "Fundamental correlation lengths of coherent speckle in medical ultrasonic images," *IEEE Transactions on Ultrasonics, Ferroelectrics, and Frequency Control*, vol. 35, no. 1, pp. 34–44, 1988.

[193] L. Y. Mo and R. Cobbold, "Speckle" in continuous wave doppler ultrasound spectra: A simulation study," *IEEE Transactions on Ultrasonics, Ferroelectrics, and Frequency Control*, vol. 33, no. 6, pp. 747–753, 1986.

[194] X. Zong, A. F. Laine, and E. A. Geiser, "Speckle reduction and contrast enhancement of echocardiograms via multiscale nonlinear processing," *IEEE Transactions on Medical Imaging*, vol. 17, no. 4, pp. 532–540, 1998.

[195] M. Szkulmowski, I. Gorczynska, D. Szlag, M. Sylwestrzak, A. Kowalczyk, and M. Wojtkowski, "Efficient reduction of speckle noise in optical coherence tomography," *Optics Express*, vol. 20, no. 2, pp. 1337–1359, 2012.

[196] E. Caiani, R. Lang, C. Korcarz, J. DeCara, L. Weinert, K. Collins, K. Spencer, S. Cerutti, and V. Mor-Avi, "Echocardiographic evaluation of left ventricular wall motion using still-frame parametric imaging," in *Computers in Cardiology 2001*. IEEE, 2001, pp. 89–92.

[197] D. Tenbrinck, A. Sawatzky, X. Jiang, M. Burger, W. Haffner, P. Willems, M. Paul, and J. Stypmann, "Impact of physical noise modeling on image segmentation in echocardiography." in *Eurographics Workshop on Visual Computing for Biology and Medicine*, 2012, pp. 33–40.

[198] G. Bhutada, R. Anand, and S. Saxena, "Edge preserved image enhancement using adaptive fusion of images denoised by wavelet and curvelet transform," *Digital Signal Processing*, vol. 21, no. 1, pp. 118–130, 2011.

[199] Y. Sheng and Z.-G. Xia, "A comprehensive evaluation of filters for radar speckle suppression," in *IEEE International Symposium on Geoscience and Remote Sensing (IGARSS),'Remote Sensing for a Sustainable Future'*, vol. 3, 1996, pp. 1559–1561.

[200] A. Balodi, M. Dewal, and A. Rawat, "Comparison of despeckle filters for ultrasound images," in *2nd IEEE International Conference on Computing for Sustainable Global Development (INDIACom)*, 2015, pp. 1919–1924.

[201] M. Kuwahara, K. Hachimura, S. Eiho, and M. Kinoshita, "Processing of RI-angiocardiographic images," in *Digital Processing of Biomedical Images*. Springer, 1976, pp. 187–202.

[202] T. R. Crimmins, "Geometric filter for speckle reduction," *Applied Optics*, vol. 24, no. 10, pp. 1438–1443, 1985.

[203] R. Vignesh, B. T. Oh, and C.-C. J. Kuo, "Fast non-local means (NLM) computation with probabilistic early termination," *IEEE Signal Processing Letters*, vol. 17, no. 3, pp. 277–280, 2010.

[204] H. Kwan and Y. Cai, "Fuzzy filters for image filtering," in *45th IEEE Midwest Symposium on Circuits and Systems, (MWSCAS)*, vol. 3, 2002, pp. III–672.

[205] H. K. Kwan, "Fuzzy filters for noise reduction in images," in *Fuzzy Filters for Image Processing*. Springer, 2003, pp. 25–53.

[206] Z. Wang, A. C. Bovik, H. R. Sheikh, and E. P. Simoncelli, "Image quality assessment: From error visibility to structural similarity," *IEEE Transactions on Image Processing*, vol. 13, no. 4, pp. 600–612, 2004.

[207] M. Iqbal, J. Chen, W. Yang, P. Wang, and B. Sun, "Sar image despeckling by selective 3d filtering of multiple compressive reconstructed images," *Progress In Electromagnetics Research*, vol. 134, pp. 209–226, 2013.

[208] O. V. Michailovich and A. Tannenbaum, "Despeckling of medical ultrasound images," *IEEE Transactions on Ultrasonics, Ferroelectrics, and Frequency Control*, vol. 53, no. 1, pp. 64–78, 2006.

[209] H. Cheng, J. Shan, W. Ju, Y. Guo, and L. Zhang, "Automated breast cancer detection and classification using ultrasound images: A survey," *Pattern Recognition*, vol. 43, no. 1, pp. 299–317, 2010.

[210] G. Paschos, "Perceptually uniform color spaces for color texture analysis: An empirical evaluation," *IEEE Transactions on Image Processing*, vol. 10, no. 6, pp. 932–937, 2001.

[211] A. Ford and A. Roberts, "Colour Space Conversions," *Westminster University, London*, vol. 1998, pp. 1–31, 1998.

[212] C. A. Poynton, "A guided tour of colour space," in *Conference on Advanced Television and Electronic Imaging , New Foundation for Video Technology: The SMPTE*, 1995, pp. 167–180.

[213] G. Wyszecki and W. S. Stiles, *Color Science*. Wiley New York, 1982, vol. 8.

[214] J. J. Koenderink, "The structure of images," *Biological Cybernetics*, vol. 50, no. 5, pp. 363–370, 1984.

[215] B. B. Mandelbrot, *The Fractal Geometry of Nature*. Macmillan, 1983, vol. 173.

[216] J. Liang, S. Yang, and A. Winstanley, "Invariant optimal feature selection: A distance discriminant and feature ranking based solution," *Pattern Recognition*, vol. 41, no. 5, pp. 1429–1439, 2008.

[217] R. Nandi, A. K. Nandi, R. M. Rangayyan, and D. Scutt, "Classification of breast masses in mammograms using genetic programming and feature selection," *Medical and Biological Engineering and Computing*, vol. 44, no. 8, pp. 683–694, 2006.

[218] Y. Saeys, I. Inza, and P. Larrañaga, "A review of feature selection techniques in bioinformatics," *Bioinformatics*, vol. 23, no. 19, pp. 2507–2517, 2007.

[219] H. Peng, F. Long, and C. Ding, "Feature selection based on mutual information criteria of max-dependency, max-relevance, and min-redundancy," *IEEE Transactions on Pattern Analysis and Machine Intelligence*, vol. 27, no. 8, pp. 1226–1238, 2005.

[220] C. Cortes and V. Vapnik, "Support-vector networks," *Machine Learning*, vol. 20, no. 3, pp. 273–297, 1995.

[221] C.-C. Chang and C.-J. Lin, “Libsvm: A library for support vector machines,” *ACM Transactions on Intelligent Systems and Technology*, vol. 2, no. 3, p. 27, 2011.

[222] L. Breiman, “Random forests,” *Machine Learning*, vol. 45, no. 1, pp. 5–32, 2001.

[223] N. Cristianini and J. Shawe-Taylor, *An Introduction to Support Vector Machines and Other Kernel-based Learning Methods*. Cambridge University Press, 2000.

[224] K.-R. Muller, S. Mika, G. Ratsch, K. Tsuda, and B. Scholkopf, “An introduction to kernel-based learning algorithms,” *IEEE Transactions on Neural Networks*, vol. 12, no. 2, pp. 181–201, 2001.

[225] A. R. Yadav, R. Anand, M. Dewal, and S. Gupta, “Multiresolution local binary pattern variants based texture feature extraction techniques for efficient classification of microscopic images of hardwood species,” *Applied Soft Computing*, vol. 32, pp. 101–112, 2015.

[226] L. Jack and A. Nandi, “Support vector machines for detection and characterization of rolling element bearing faults,” *Institution of Mechanical Engineers, Part C: Journal of Mechanical Engineering Science*, vol. 215, no. 9, pp. 1065–1074, 2001.

[227] A. Ben-Hur, C. S. Ong, S. Sonnenburg, B. Schölkopf, and G. Rätsch, “Support vector machines and kernels for computational biology,” *PLoS Computational Biology*, vol. 4, no. 10, p. e1000173, 2008.

[228] G.-X. Yuan, C.-H. Ho, and C.-J. Lin, “Recent advances of large-scale linear classification,” *Proceedings of the IEEE*, vol. 100, no. 9, pp. 2584–2603, 2012.

[229] T. Hastie, R. Tibshirani, J. Friedman, T. Hastie, J. Friedman, and R. Tibshirani, *The elements of statistical learning*. Springer, 2009, vol. 2.

[230] J. C. Platt, N. Cristianini, and J. Shawe-Taylor, “Large margin DAGs for multiclass classification,” in *12th International Conference on Neural Information Processing Systems*. MIT press, 1999, pp. 547–553.

[231] K. Crammer and Y. Singer, “On the learnability and design of output codes for multiclass problems,” *Machine Learning*, vol. 47, no. 2-3, pp. 201–233, 2002.

[232] V. Lempitsky, M. Verhoek, J. A. Noble, and A. Blake, “Random forest classification for automatic delineation of myocardium in real-time 3D echocardiography,” in *In-*

ternational Conference on Functional Imaging and Modeling of the Heart, 2009, pp. 447–456.

[233] B. C. Ko, S. H. Kim, and J.-Y. Nam, "X-ray image classification using random forests with local wavelet-based CS-local binary patterns," *Journal of Digital Imaging*, vol. 24, no. 6, pp. 1141–1151, 2011.

[234] A. M. Prasad, L. R. Iverson, and A. Liaw, "Newer classification and regression tree techniques: Bagging and random forests for ecological prediction," *Ecosystems*, vol. 9, no. 2, pp. 181–199, 2006.

[235] F.-f. Ai, J. Bin, Z.-m. Zhang, J.-h. Huang, J.-b. Wang, Y.-z. Liang, L. Yu, and Z.-y. Yang, "Application of random forests to select premium quality vegetable oils by their fatty acid composition," *Food Chemistry*, vol. 143, pp. 472–478, 2014.

[236] M. Liu, M. Wang, J. Wang, and D. Li, "Comparison of random forest, support vector machine and back propagation neural network for electronic tongue data classification: Application to the recognition of orange beverage and chinese vinegar," *Sensors and Actuators B: Chemical*, vol. 177, pp. 970–980, 2013.

[237] A. R. Yadav, R. Anand, M. Dewal, and S. Gupta, "Hardwood species classification with DWT based hybrid texture feature extraction techniques," *Sadhana*, vol. 40, no. 8, pp. 2287–2312, 2015.

[238] M. D. DiFranco, G. OHurley, E. W. Kay, R. W. G. Watson, and P. Cunningham, "Ensemble based system for whole-slide prostate cancer probability mapping using color texture features," *Computerized Medical Imaging and Graphics*, vol. 35, no. 7, pp. 629–645, 2011.

[239] S. Geisser, *Predictive Inference*. CRC press, 1993, vol. 55.

[240] T.-T. Wong, "Performance evaluation of classification algorithms by k-fold and leave-one-out cross validation," *Pattern Recognition*, vol. 48, no. 9, pp. 2839–2846, 2015.

[241] N. Fatma Guler and E. D. Ubeyli, "Multiclass support vector machines for EEG-signals classification," *IEEE Transactions on Information Technology in Biomedicine*, vol. 11, no. 2, pp. 117–126, 2007.

[242] J. F. Hair, W. C. Black, B. J. Babin, R. E. Anderson, and R. L. Tatham, *Multivariate Data Analysis*. Pearson Prentice Hall Upper Saddle River, NJ, 2006, vol. 6.

[243] L. Larkin and P. Burt, "Multi-resolution texture energy measures," in *Proceeding of IEEE Conference on Computer Vision Pattern Recognition*, 1983, pp. 519–520.

[244] P. J. Burt, "Fast algorithms for estimating local image properties," *Computer Vision, Graphics, and Image Processing*, vol. 21, no. 3, pp. 368–382, 1983.

[245] ——, "Fast filter transform for image processing," *Computer Graphics and Image Processing*, vol. 16, no. 1, pp. 20–51, 1981.

[246] L. Nanni, A. Lumini, and S. Brahnam, "Local binary patterns variants as texture descriptors for medical image analysis," *Artificial Intelligence in Medicine*, vol. 49, no. 2, pp. 117–125, 2010.

[247] ——, "Survey on LBP based texture descriptors for image classification," *Expert Systems with Applications*, vol. 39, no. 3, pp. 3634–3641, 2012.

[248] L. Nanni, M. Paci, S. Brahnam, S. Ghidoni, and E. Menegatti, "Local phase quantization texture descriptor for protein classification," in *International Conference on Bioinformatics & Computational Biology (BIOCOMP)*, 2013, p. 1.

[249] T. Ojala, M. Pietikäinen, and D. Harwood, "A comparative study of texture measures with classification based on featured distributions," *Pattern Recognition*, vol. 29, no. 1, pp. 51–59, 1996.

[250] M. Pietikäinen, A. Hadid, G. Zhao, and T. Ahonen, *Local Binary Patterns for Still Images*. Springer, 2011.

[251] T. Mäenpää, *The Local Binary Pattern Aapproach to Texture Analysis: Extensions and Applications*. Oulun yliopisto, 2003.

[252] M. Heikkilä, M. Pietikäinen, and C. Schmid, "Description of interest regions with local binary patterns," *Pattern Recognition*, vol. 42, no. 3, pp. 425–436, 2009.

[253] Y. Zheng, C. Shen, R. Hartley, and X. Huang, "Effective pedestrian detection using center-symmetric local binary/trinary patterns," *arXiv preprint arXiv:1009.0892*, 2010.

[254] T. Ahonen, J. Matas, C. He, and M. Pietikäinen, "Rotation invariant image description with local binary pattern histogram fourier features," in *Scandinavian Conference on Image Analysis*, 2009, pp. 61–70.

[255] G. Zhao, T. Ahonen, J. Matas, and M. Pietikainen, "Rotation-invariant image and video description with local binary pattern features," *IEEE Transactions on Image Processing*, vol. 21, no. 4, pp. 1465–1477, 2012.

[256] Z. Guo, L. Zhang, and D. Zhang, "A completed modeling of local binary pattern operator for texture classification," *IEEE Transactions on Image Processing*, vol. 19, no. 6, pp. 1657–1663, 2010.

[257] R. C. Gonzalez and R. E. Woods, *Digital Image Processing*. Prentice-Hall of India Pvt. Ltd, 2002.

[258] V. Jain and J. Sahambi, "Neural network and wavelets in arrhythmia classification," in *Conference on Asian Applied Computing*. Springer, 2004, pp. 92–99.

[259] H. K. Ekenel and B. Sankur, "Multiresolution face recognition," *Image and Vision Computing*, vol. 23, no. 5, pp. 469–477, 2005.

[260] R. R. Paul, A. Mukherjee, P. K. Dutta, S. Banerjee, M. Pal, J. Chatterjee, K. Chaudhuri, and K. Mukkerjee, "A novel wavelet neural network based pathological stage detection technique for an oral precancerous condition," *Journal of Clinical Pathology*, vol. 58, no. 9, pp. 932–938, 2005.

[261] D. Kumar, P. d. Carvalho, M. Antunes, J. Henriques, M. Maldonado, R. Schmidt, and J. Habetha, "Wavelet transform and simplicity based heart murmur segmentation," in *Computers in Cardiology, 2006*. IEEE, 2006, pp. 173–176.

[262] C. Pujara, A. Bhardwaj, V. M. Gadre, and S. Khire, "Secure watermarking in fractional wavelet domains," *IETE Journal of Research*, vol. 53, no. 6, pp. 573–580, 2007.

[263] S. Kumar, R. Gupta, N. Khanna, S. Chaudhury, and S. D. Joshi, "Text extraction and document image segmentation using matched wavelets and MRF model," *IEEE Transactions on Image Processing*, vol. 16, no. 8, pp. 2117–2128, 2007.

[264] A. Apatean, A. ROGOZAN, S. EMERICH, and A. BENSRHAIR, “Wavelets as features for objects recognition,” *Acta Tehnica Napocensis-Electronics and Telecommunications*, vol. 49, pp. 23–26, 2008.

[265] C. S. Anand and J. S. Sahambi, “Wavelet domain non-linear filtering for MRI denoising,” *Magnetic Resonance Imaging*, vol. 28, no. 6, pp. 842–861, 2010.

[266] S. Nirmala, S. Dandapat, and P. Bora, “Wavelet weighted blood vessel distortion measure for retinal images,” *Biomedical Signal Processing and Control*, vol. 5, no. 4, pp. 282–291, 2010.

[267] R. S. Sengar, A. K. Upadhyay, M. Singh, and V. M. Gadre, “Segmentation of two dimensional electrophoresis gel image using the wavelet transform and the watershed transform,” in *2012 IEEE National Conference on Communications (NCC)*, 2012, pp. 1–5.

[268] B. Deka and P. K. Bora, “Wavelet-based despeckling of medical ultrasound images,” *IETE Journal of Research*, vol. 59, no. 2, pp. 97–108, 2013.

[269] R. D. Gupta, J. K. Dash, and M. Sudipta, “Rotation invariant textural feature extraction for image retrieval using eigen value analysis of intensity gradients and multiresolution analysis,” *Pattern Recognition*, vol. 46, no. 12, pp. 3256–3267, 2013.

[270] S. Nirmala, S. Dandapat, and P. Bora, “Wavelet weighted distortion measure for retinal images,” *Signal, Image and Video Processing*, vol. 7, no. 5, pp. 1005–1014, 2013.

[271] G. Fan and X.-G. Xia, “Wavelet-based texture analysis and synthesis using hidden markov models,” *IEEE Transactions on Circuits and Systems I: Fundamental Theory and Applications*, vol. 50, no. 1, pp. 106–120, 2003.

[272] I. Daubechies *et al.*, *Ten Lectures on Wavelets*. SIAM, 1992, vol. 61.

[273] J. Z. Wang, G. Wiederhold, O. Firschein, and S. Xin Wei, “Content-based image indexing and searching using daubechies’ wavelets,” *International Journal on Digital Libraries*, vol. 1, no. 4, pp. 311–328, 1998.

[274] S. Mahmoodabadi, A. Ahmadian, and M. Abolhasani, “ECG feature extraction using Daubechies wavelets,” in *Fifth International conference on Visualization, Imaging and Image Processing*, 2005, pp. 343–348.

[275] A. Khare, M. Khare, Y. Jeong, H. Kim, and M. Jeon, “Despeckling of medical ultrasound images using Daubechies complex wavelet transform,” *Signal Processing*, vol. 90, no. 2, pp. 428–439, 2010.

[276] M. Sharma, A. Dhere, R. B. Pachori, and U. R. Acharya, “An automatic detection of focal EEG signals using new class of time–frequency localized orthogonal wavelet filter banks,” *Knowledge-Based Systems*, vol. 118, pp. 217–227, 2017.

[277] J. G. Daugman, “An information-theoretic view of analog representation in striate cortex,” in *Conference on Computational neuroscience*. MIT Press, 1993, pp. 403–423.

[278] A. C. Bovik, M. Clark, and W. S. Geisler, “Multichannel texture analysis using localized spatial filters,” *IEEE Transactions on Pattern Analysis and Machine Intelligence*, vol. 12, no. 1, pp. 55–73, 1990.

[279] A. K. Jain and F. Farrokhnia, “Unsupervised texture segmentation using Gabor filters,” *Pattern Recognition*, vol. 24, no. 12, pp. 1167–1186, 1991.

[280] D. Sripathi and S. Y. Foo, *Efficient Implementations of Discrete Wavelet Transforms using FPGAs*, 2003.